JOHANNES GUTENBERG
UNIVERSITÄT MAINZ

Measurement of Proton Electromagnetic Form Factors Using the Initial-State-Radiation Process $e^+e^- \to p\bar{p}\gamma$ at BESIII

Dissertation

zur Erlangung des Grades
"Doktor der Naturwissenschaften"

am Fachbereich Physik, Mathematik und Informatik
der Johannes Gutenberg-Universität
in Mainz

von
Dexu Lin
geboren in Sichuan, China

Mainz, July 2017

一尺之棰，日取其半，萬世不竭。

—- 莊周《莊子・天下》

A chi-long stick, cut in half every day,
will never be exhausted in myriad ages.
— “Chuang-Tzu · All-Under-Heaven”
by Chuang Chou

Abstract

The proton is one of the basic building blocks of atomic nuclei and has fundamental properties determined by its internal structure. Understanding the proton's internal structure in terms of quark and gluon degrees of freedom is one of the most important and challenging problems in modern nuclear physics. The electromagnetic structure of the proton can be studied by measuring the electromagnetic form factors. In the time-like kinematic region, several experiments have been performed in the last two decades. However, limited statistics in most cases only allowed for extraction of the effective form factor of the proton. Only few experiments have been able to extract the ratio of the electric and magnetic form factors of the proton, with uncertainties larger than 11%. The results of the ratio from different experiments show strong discrepancies in the momentum-transferred region close to the proton-antiproton pair ($p\bar{p}$) production threshold.

In this thesis, the proton electromagnetic form factors are studied via the initial-state-radiation process $e^+e^- \to p\bar{p}\gamma$. The total luminosity used amounts to 7.41 fb^{-1}. It was collected at seven center-of-mass energies between 3.773 and 4.600 GeV with the BESIII spectrometer at the BEPCII collider. Two scenarios can be distinguished depending on whether the radiated photon is detected (tagged case, around 12% of the events) or not (untagged case, around 40% of the events). In the analysis with the radiated photon tagged, the ratio of proton form factors is extracted for six bins of the momentum transfer from 1.877 to 3.0 GeV/c. The statistical and systematic uncertainties range from 18.5% to 33.6% and 4.5% to 15.6%, respectively. The cross section of $e^+e^- \to p\bar{p}$ and the effective form factor of the proton are measured in bins of 25 MeV/c width from 1.877 to 2.3 GeV/c, and in bins of 50 MeV/c width from 2.3 to 3.0 GeV/c, with statistical uncertainties at the 10% level. In the analysis with the radiated photon untagged, the cross section of $e^+e^- \to p\bar{p}$ and the effective form factor of the proton are measured from 2.0 to 3.8 GeV/c with statistical and systematic uncertainties at the few-percent level. However, due to the particular angular distribution of these events, the ratio of proton form factors is only extracted for four bins from 2.0 to 3.0 GeV/c, with statistical and systematic uncertainties from 24.8% to 35.4% and 7.1% to 14.8%, respectively.

The measurements presented in this work are essential for further understanding of the $e^+e^- \to p\bar{p}$ process and the proton electromagnetic form factors in a wide momentum-transferred region. Close to the $p\bar{p}$ threshold, the ratio of proton form factors confirms the results from BABAR and CMD-3, conflicting with PS170. At higher momentum transfers, the ratio of proton form factors is consistent with existing measurements. The cross section and the effective form factor are in a good agreement with previous measurements at the few-percent precision level.

Zusammenfassung

Das Proton stellt eines der grundlegenden Bausteine der Atomkerne dar und besitzt fundamentale Eigenschaften, welche durch seine innere Struktur bedingt werden. Eine der wichtigsten und herausfordernden Fragen aktueller Physik ist das Verständnis der inneren Struktur des Protons im Bezug auf die quarkonischen und gluonischen Freiheitsgrade. Die elektromagnetische Struktur des Protons kann mittels Messung elektromagnetischer Formfaktoren studiert werden. Innerhalb der letzten beiden Jahrzehnte beschäftigten sich mehrere Experimente mit der Erforschung des zeitartigen, kinematischen Bereichs. Aufgrund der geringen Datenmengen in den meisten Fällen konnte dabei jedoch nur der effektive Formfaktor bestimmt werden. Nur wenige Experimente gelang es, das Verhältnis der Formfaktoren aus den Messdaten zu extrahieren, wobei die zugehörigen Unsicherheiten bei mehr als 11% lagen. Die gewonnenen Resultate weisen im Bereich der $p\bar{p}$–Produktionsschwelle zudem starke Diskrepanzen auf.

Im Rahmen dieser Arbeit wurden die elektromagnetischen Formfaktoren mittels Prozessen der Initial-State-Radiation, $e^+e^- \to p\bar{p}\gamma$, untersucht. Die zeitintegrierte Luminosität beläuft sich dabei auf 7.41 fb^{-1}, welche bei insgesamt sieben verschiedenen Schwerpunktsenergien zwischen 3.773 und 4.600 GeV mit dem BESIII Spektrometer am BEPII Collider gemessen wurde. Es wird dabei zwischen zwei unterschiedlichen Szenarien unterschieden. In Abhängigkeit davon, ob das emittierte Photon detektiert wurde, spricht man vom tagged case, welcher bei etwa 12% der Ereignisse vorliegt, oder aber vom untagged case (im Falle von etwa 40% der Ereignisse), bei welchem das Photon nicht detektiert wird. Im tagged case wurde das Verhältnis der Formfaktoren des Protons bei sechs unterschiedlichen Messintervallen des Viererimpulsübertrags im Bereich von 1.877 bis 3.0 GeV/c bestimmt. Die statistischen (systematischen) Unsicherheiten liegen dabei im Bereich von 18.5% bis 33.6% (4.5% bis 15.6%). Der Wirkungsquerschnitt des Prozesses $e^+e^- \to p\bar{p}$ sowie der effektive Formfaktor des Protons wurden in Messintervallen mit einer Breite von 25 MeV/c im Bereich von 1.877 bis 2.3 GeV/c , sowie mit einer Breite von 50 MeV/c zwischen 2.3 und 3.0 GeV/c gemessen, welche mit statistischen Unsicherheiten in der Größenordnung von

10% verbunden sind. In der Analyse des untagged case wurde der Wirkungsquerschnitt von $e^+e^- \to p\bar{p}$ und der effektive Formfaktor des Protons im Bereich von Viererimpulsüberträgen von 2.0 bis 3.8 GeV/c gemessen, wobei in diesem Fall die statistischen und systematischen Unsicherheiten in der Größenordnung von wenigen Prozent liegen. Jedoch konnte aufgrund der speziellen Winkelverteilung dieser Ereignisse das Verhältnis der Formfaktoren in lediglich vier verschiedenen Messintervallen im Bereich von 2.0 bis 3.0 GeV/c bestimmt werden. Dabei wurden statistische Unsicherheiten von 24.8% bis 35.4%, sowie systematische Unsicherheiten zwischen 7.1% bis 14.8% erreicht.

Die Messungen, welche in dieser Arbeit vorgestellt werden sollen, sind essentiell für das tiefergehende Verständnis des Prozesses $e^+e^- \to p\bar{p}$, sowie der elektromagnetischen Formfaktoren des Protons für einen großen Bereich des bei dieser Reaktion übertragenen Viererimpulses. Im Bereich der $p\bar{p}$-Produktionsschwelle bestätigen die Resultate dieser Analyse die Ergebnisse, welche bei BABAR sowie CMD-3 gewonnen wurden, stehen jedoch in Konflikt mit den Resultaten von PS170. Bei höherem Impulsübertrag stehen die ermittelten Werte für das Verhältnis der Formfaktoren des Protons in Einklang mit bereits existierenden Messungen. Der gemessene Wirkungsquerschnitt sowie der effektive Formfaktor weisen eine gute Vereinbarkeit mit den Resultaten früherer Messungen mit einer Präzision im Bereich von wenigen Prozent auf.

Contents

List of Figures

List of Tables

CHAPTER 1

Introduction to the Standard Model of Particle Physics

What is the most elementary particle composing the universe? This question has been explored for thousands of years, and can be traced back to the most ancient human civilizations. A Chinese philosopher Chuang Tzu, who lived around 4th century BC, had recorded a celebrated thesis: a chi-long* stick, which is taken away half daily, will never be exhausted in myriad ages [1]. This thought basically indicated that matter is infinitely divisible. Simultaneously, an ancient Greek philosopher Democritus (460 – 370 BC) proposed a theory in which everything is composed of "atoms", which are physical and indestructible, not geometrical and indivisible, have always been and will always be, in motion. Until the 1930s, the early framework of the structure of matter was established following the discoveries of the electron (1897), the proton (1917) and the neutron (1932). At the same time, the Quantum Mechanics by Max Plank (1858 - 1947) and the Theory of Relativity by Albert Einstein (1879 - 1955) had emerged, becoming the theoretical basis of Particle Physics in the 20th century.

*Chi: traditional Chinese unit of length, the value of which varied from 23.1 to 24.3 cm until the 3rd century AD. The modern value is defined as $33\frac{1}{3}$ cm in China mainland, $14\frac{5}{8}$ inch in Hongkong (pronounced $chek$ in Cantonese) and $\frac{10}{33}$ m in Taiwan.

1.1 Elementary particles

In the Standard Model, elementary particles can be classified into two types: fundamental fermions including leptons and quarks, which are known as "matter particles", and fundamental bosons including gauge bosons and Higgs bosons, which are usually called "force particles" and mediate interactions among fermions [2].

Figure.1.1 shows the basic features of the elementary particles. The fundamental spin-$\frac{1}{2}$ particles are six leptons and six quarks, which are grouped into three generations based on their masses. Each lepton or quark has a corresponding antilepton or antiquark. Leptons carrying integral electric charge exist as free particles; quarks carrying fractional electric charge are traditionally confined as quark-antiquark pairs (mesons) or three-quark combinations (baryons) because of the confinement of the "color charge", which is an internal quantum number of quarks (and gluons, the carriers of the strong interaction). The color charge can be analogized to three primary colors—red, green and blue—as well as three anti-colors—anti-red, anti-green and anti-blue—for the antiquarks.

The charged $leptons$ with integral electric charge are the electron e, the muon μ and the tau τ, with one unit of negative charge. Both the muon and the tau are unstable particles with mean lifetimes of 2.2×10^{-6} s and 2.9×10^{-13} s, respectively, and decay spontaneously into lighter leptons and other particles.

The neutral leptons are called $neutrinos$ ν, and were first postulated by Pauli in 1930 in order to account for the energy and momentum conservation in the β decay. Neutrinos come in three flavors: electron neutrino ν_e, muon neutrino ν_μ, and tau neutrino ν_τ. Each flavor has an associated antiparticle, called antineutrino which is also electrically neutral and has spin $\frac{1}{2}$. Neutrinos and antineutrinos are distinguished by the left-hand and right-hand helicity, respectively.

The $quarks$ carry fractional electric charges of $+\frac{2}{3}e$ or $-\frac{1}{3}e$, and have six flavors: up (u), down (d), strange (s), charm (c), top (t) and bottom (b), as shown in Fig. 1.1. Only the quarks with lowest mass (up and down) are stable; the heavier quarks decay rapidly to the lighter quarks and leptons.

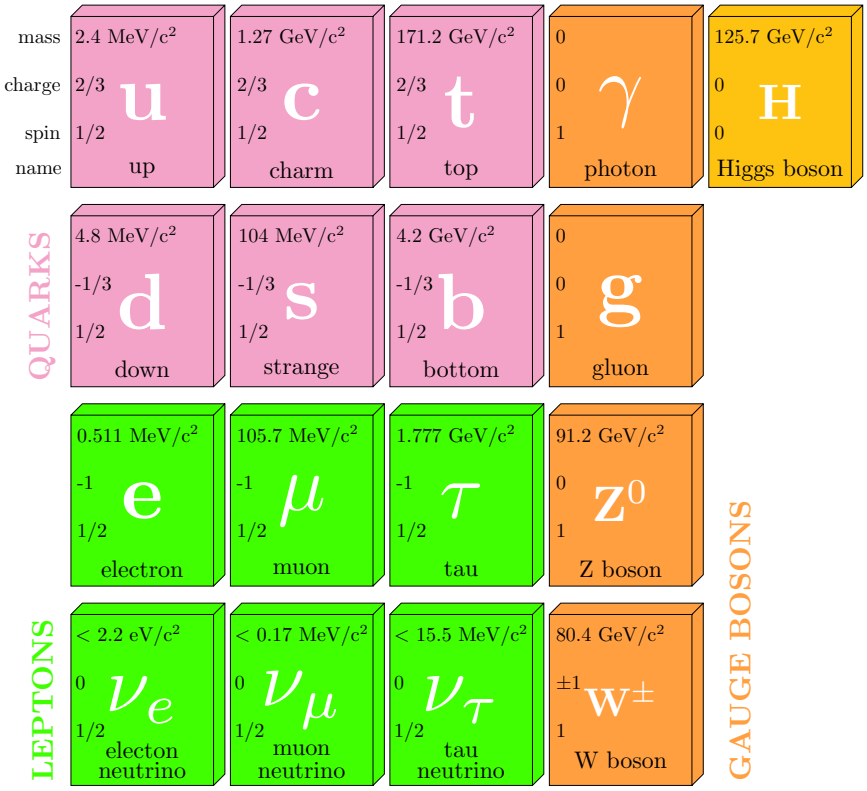

Fig. 1.1: The elementary particles of the Standard Model: three generations of fermions (col. 1 - 3), gauge bosons (col. 4) and Higgs boson (col. 5)

1.2 Fundamental interactions

There are four fundamental interactions in nature, characterized by different coupling strengths and interaction ranges at a typical measuring scale of 1 GeV. The strong interaction has a range of 10^{-15} m and is responsible for the formation of nucleons and nuclear binding. The electromagnetic interaction is responsible for virtually all the phenomena in the extra-nuclear physics, in particular for the bound states of electrons with nuclei. This interaction, mediated by photon exchange, has an infinite range, and its strength is determined by the fine structure constant of $\alpha \simeq \frac{1}{137}$. The weak interaction is responsible for radioactive decays, has an interaction range of 10^{-18} m and is about 10^5 times weaker than the strong interaction. The gravitational interaction also has an infinite interaction range with a coupling constant of about 10^{-38}, which is extremely low and not included in the standard model of particle physics. The properties of all four interactions are summarized in Tab.1.1.

The **electromagnetic interaction** is well-described by the theory of *quantum electrodynamics* (QED) through the renormalization of quantum field theory. Although the theory of the **weak interaction** is sometimes called quantum flavourdynamics (QFD), the weak interaction is better understood by the spontaneously broken SU(2)×U(1) *electroweak theory* due to the unification of these two interactions at higher energy scales.

The **strong interaction**, described by the unbroken SU(3) gauge field theory of *quantum chromodynamics* (QCD), confines quarks to form hadrons at short-distance range (~ 0.8 fm) and binds nucleons (protons and neutrons) to form nucleus at longer-distance range ($\sim$1.0 - 3.0 fm). In the context of hadron formation, the interaction is mediated through the exchange of massless gluons between colored quarks, which is very similar to the massless photon exchanged between charged particles in the electromagnetic interaction. Unlike the electrically neutral photon, gluons are colored particles and can therefore interact (self-couple) with other gluons.

Tab. 1.1: Properties of the fundamental interactions.

Interaction	Strong	Electromagnetic	Weak	Gravitation
Acts on	color charge	electric charge	flavor	Mass - Energy
Particles experiencing	quarks, gluons	electrically charged	quarks, leptons	all
Mediators	gluons	photons	Z and W bosons	gravitons
Strength	~ 1	$\sim \frac{1}{137}$	$\sim 10^{-5}$	$\sim 10^{-38}$
Range (m)	10^{-15}	∞	10^{-18}	∞
Current theory	Quantum Chromodynamics (QCD)	Quantum Electrodynamics (QED)	Electroweak Theory (EWT)	General Relativity (GR)

1.3 Quantum chromodynamics

The Lagrangian of QCD [3] is written as

$$\mathcal{L}_{\mathrm{QCD}} = -\frac{1}{4} F^a_{\mu\nu} F^{\mu\nu}_a + \bar{\psi}^i_q (i\gamma^\mu)(D_\mu)_{ij} \psi^j_q - m_q \bar{\psi}^i_q \psi_{qi}, \tag{1.1}$$

where ψ_q^i denotes a quark field with the color index i ($i = [R, G, B]$), γ^μ is a Dirac matrix with a Lorentz vector index μ, m_q is the quark mass, $F_{\mu\nu}^a$ is the gluon field strength tensor for a gluon with color index a (i.e., $a \in [1, ..., 8]$), and D_μ is the covariant derivative,

$$(D_\mu)_{ij} = \delta_{ij}\partial_\mu - \frac{1}{2} i g_s \lambda_{ij}^a A_\mu^a. \tag{1.2}$$

In the previous Eq. 1.2, the strong coupling $g_s^2 = 4\pi\alpha_s$ (α_s is called the running coupling), A^a is the gluon field with the color index a, and λ^a are the Hermitian and traceless Gell-Mann matrices of SU(3) [3, 4]. The running coupling, α_s, depends on the the energy of the strong process involved, usually given by a reference scale with the momentum transfer squared, $Q^2 = m_Z^2$:

$$\alpha_s(Q^2) = \frac{\alpha_s(m_Z^2)}{1 + b_0 \alpha_s(m_Z^2) \ln \frac{Q^2}{m_Z^2} + \mathcal{O}(\alpha_s^2)}, \tag{1.3}$$

where m_Z is the mass of Z boson, and $b_0 = \frac{11C_A - 4n_f T_R}{12\pi}$ is the coefficient related to the one-loop beta-function, in which the first term describes gluon loops and the second one describes quark ones. Figure 1.2 shows α_s as a function of the energy scale Q and $\alpha_s(m_Z) = 0.1181 \pm 0.0011$ [4].

At high energy scale (short-distance range), the running coupling α_s is small, and a perturbative theory can be applied to describe the terms of quark and gluon interactions. The first and most successful test of perturbative QCD (PQCD) is R-value measurement in the electron-positron annihilation, where R is the ratio of the inclusive hadron production rate to the muon-pair production rate ($R = \frac{\sigma_{e^+e^- \to \text{hadrons}}}{\sigma_{e^+e^- \to \mu^+\mu^-}}$) [4].

The degrees of freedom are changed from quarks and gluons to hadrons in the low-energy ($\approx$ 1 GeV) regime of QCD, which becomes non-perturbative [5]. It is not possible to describle the interactions between the hadrons directly from the QCD Lagrangian by applying perturbative methods.

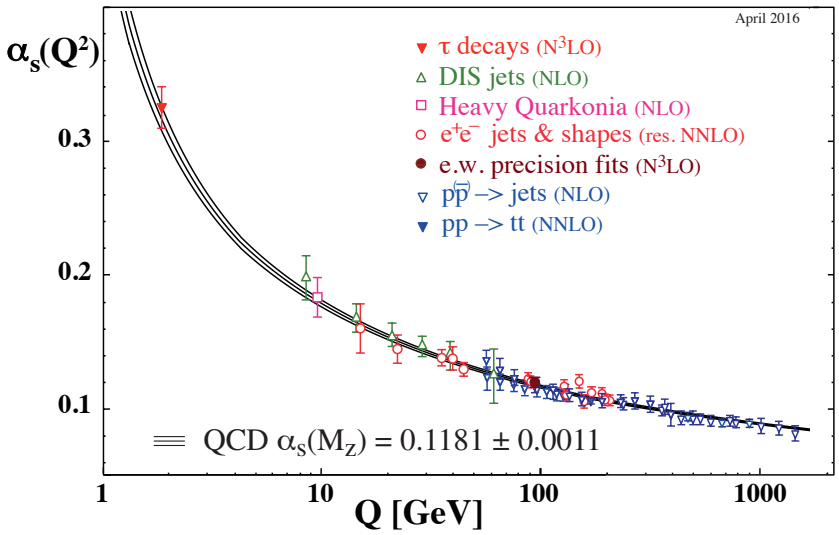

Fig. 1.2: The running coupling of the strong interaction, α_s, measured as a function of the energy scale Q [4].

1.4 The proton in the Standard Model

Due to the color confinement as mentioned in the previous sections, quarks (antiquarks) cannot be isolated singularly, and cannot be observed directly. Traditionally, quarks are clumped together to form two types of hadrons, mesons and baryons. Based on the naive quark model (NQM) [6], mesons consist of quark and antiquark, and baryons consist of three quarks. The lightest mesons and baryons are pions and nucleons (proton and neutron), respectively, and only contain quarks (antiquarks) of the lightest quark generation, up and $down$.

The proton consists of two up quarks and one $down$ quark. The total mass of three quarks ($2m_u + m_d$) is only around 10 MeV/c^2. However, the rest mass of proton is larger than 938 MeV/c^2, which is around 94 times higher than the total mass of the valence quarks. The strong interaction among quarks confined inside the proton is mediated by gluons according to the QCD theory, and most of the proton mass arises from the interaction itself. As mentioned above, due to the non-perturbative nature of the interaction at low energies ($\approx$ 1 GeV), dynamics can be parametrized inside non-perturbative (long-distance) functions, such as parton distribution functions, fragmentation functions, generalized parton distributions, form

factors and so on. This thesis focuses on the measurement of two of these functions, the electromagnetic form factors (FFs) of the proton, extracted through the electron-positron annihilation process.

Electromagnetic processes are an excellenttool to investigate the structure of the nucleons. Under suitable conditions, it is possible to factorize short- and long-distance contributions (large- and smal-energy-scale effects, respectively) to the reaction mechanism. Each of these contributions can then be calculated using different techniques. The short-distance factor is typically calculated by making use of powerful analytic techniques, such as weak-coupling perturbation theory and the renormalization group, while the long-distance part may be amenable to lattice gauge theory or phenomenological methods [7]. The principle of universality in factorization states that a long-distance factor can be determined from one theoretical or phenomenological calculation and can then be applied in a model-independent way to a number of different processes. In a reaction of the kind $e^+e^- \to h\bar{h}$ (hadron-antihadron pair) through the exchange of one virtual photon, the hadronic interaction can be completely parametrized by the hadronic form factors, which can be regarded as containing all the long-distance (non-perturbative) effects produced by the strong interaction within and between the hadrons.

CHAPTER 2

Proton Electromagnetic Form Factors

The structure of the nucleon plays a central role in our understanding of the strong interaction in hadronic physics. Electromagnetic form factors (FFs) are the most fundamental objects which can be used to describe the electromagnetic internal structure and the dynamics of the nucleons. The measurements of the FFs have had significant achievements since the early 1950s, when Hofstadter and his group first measured the proton form factors in scattering experiments at the High Energy Physics Laboratory at Stanford University [8–10].

2.1 Early definition of the proton form factor

The early definitions of the FFs are credited to Rosenbluth [11], who discussed the role of the reduced charge (e') and magnetic moments ($\kappa' e'$ with the effective anomalous magnetic moment κ') of the proton in high-energy $electron\text{-}proton$ (ep) scattering experiments. The effective charge and magnetic moments, $\frac{e'}{e}$ and $\frac{\kappa' e'}{\kappa_0 e}$ (κ_0 is the anomalous magnetic moment), repectively, were first derived by Schiff [12, 13].

In the early framework, the phenomenological FF, $|F(q)|^2$, was defined from the ep differential cross section measurements [13, 14]:

$$|F(q)|^2 = \frac{\sigma(q)}{\sigma_{\text{Mott}}(q)}, \tag{2.1}$$

where $q = |\vec{q}|$ and $\vec{q}$ stands the momentum transferred by the virtual photon exchanged, and $\sigma_{\text{Mott}} = (\frac{\alpha}{2E_{\text{beam}}})^2 \frac{\cos^2(\theta_e/2)}{\sin^4(\theta_e/2)}$ is the Mott cross section for the scattering of a spin-$\frac{1}{2}$ electron by a point-like proton, with E_{beam} the beam energy of the incident electron and θ_e the electron scattering angle in laboratory.

In the non-relativistic limit, the FF is the Fourier transform of the charge distribution in the Breit frame:

$$F(\vec{q}) = \int \rho(\vec{r}) e^{i\vec{q}\cdot\vec{r}} d^3r, \tag{2.2}$$

where the charge density of the proton, $\rho(\vec{r})$, is normalized as $\int \rho(\vec{r}) d^3r = 1$. When $|\vec{q}|$ is small enough, the FF can be expanded as:

$$\begin{aligned} F(\vec{q}) &= \int \left(1 + i\vec{q}\cdot\vec{r} - \frac{(\vec{q}\cdot\vec{r})^2}{2} + \cdots\right) \rho(\vec{r}) d^3r \\ &= 1 - \frac{1}{6}|\vec{q}|^2 < r^2 > + \cdots, \end{aligned} \tag{2.3}$$

where $< r^2 >$ is the mean square radius of the charge cloud.

Later, Clementel and Villi defined the charged and static magnetic FFs as $F_1(q) = \frac{e'}{e}$ and $F_2(q) = \frac{\kappa' e'}{\kappa_0 e}$, respectively [15]. These form factors were first introduced by Hofstadter [14,16] as the Dirac and Pauli FFs. The Dirac FF represents the deviation of the effective charge from a point-like charged Dirac particle, while the Pauli FF represents the deviation of the effective magnetic moment from a point-like anomalous magnetic moment.

2.2 Proton form factors in scattering and annihilation processes

As mentioned above, proton FFs were traditionally determined by the measurement of elastic ep scattering. Assuming one virtual photon exchange between electron and proton,

the amplitude ($\mathcal{M}$) for the elastic scattering process illustrated in Fig. 2.1 can be written as [13, 17]

$$i\mathcal{M} = \frac{-ig_{\mu\nu}}{q^2}[ie\bar{u}(k_2)\gamma^\nu u(k_1)][-ie\bar{N}(p_2)\Gamma^\mu(p_2,p_1)N(p_1)] = \frac{-i}{q^2}\ell_\mu \mathcal{J}^\mu, \tag{2.4}$$

where ℓ_μ and $\mathcal{J}^\mu$ are the four-component leptonic and hadronic currents, respectively. In the equation, q^2 is the momentum transfer squared of the exchanged virtual photon, k_1 (k_2) and p_1 (p_2) are the four-momenta of the electron and proton in the initial (final) state, u and N are the electron and proton spinors, $g_{\mu\nu}$ is the metric tensor and $\gamma^\nu = \{\gamma^0, \gamma^1, \gamma^2, \gamma^3\}$ are the gamma matrices. The vertex Γ^μ describes the interaction of a virtual photon with a proton and contains the information accounting for proton structure.

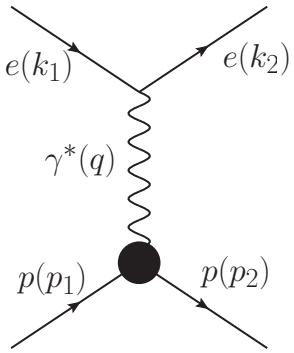

Fig. 2.1: Feynman diagram for the elastic *electron-proton* scattering in the Born approximation.

For a spin-$\frac{1}{2}$ hadron with internal structure, the most general form for the hadronic current $\mathcal{J}^\mu$ satisfies relativistic invariant and current-conservation [13, 17–20]:

$$\mathcal{J}^\mu = -ie\bar{N}(p_2)[\gamma^\mu F_1(Q^2) + \frac{i\sigma^{\mu\nu}}{2m_p}q_\nu F_2(Q^2)]N(p_1), \tag{2.5}$$

where $\sigma^{\mu\nu} = \frac{1}{2}[\gamma_\mu, \gamma_\nu]$, m_p is the proton mass, and F_1 and F_2 are the Dirac and Pauli FFs mentioned above. For the elastic scattering process of Fig. 2.1, both FFs, F_1 and F_2, are real functions of $Q^2 = -q^2$. The momentum transfer squared, q^2, is a negative quantity [13]

$$q^2 = (k_1 - k_2)^2 \simeq -2k_1 \cdot k_2 < 0 \tag{2.6}$$

Since the leptonic vertex is well-known by the theory of quantum electrodynamics (QED), the quantities of the FFs can be extracted from the differential cross section measurement of the scattering process. The differential cross section is obtained from

$$\begin{aligned} \left.\frac{d\sigma}{d\Omega_e}\right|_{\text{lab}} &= \frac{|\overline{\mathcal{M}}|^2}{64\pi^2 m_p}\left(\frac{E_2}{E_1}\right)^2, \\ \text{with } |\overline{\mathcal{M}}|^2 &= \frac{1}{(q^2)^2}|\overline{\ell \cdot \mathcal{J}}|^2, \end{aligned} \tag{2.7}$$

where E_1 and E_2 are energies of the incident and scattered electron. Based on Eq. 2.4 and 2.5, the differential cross section is written as [11, 20]

$$\begin{aligned} \left.\frac{d\sigma}{d\Omega_e}\right|_{\text{lab}} =& \frac{\alpha^2}{4E_1^2 \sin^4\frac{\theta_e}{2}}\frac{E_1}{E_2} \times \\ & \left[\left(F_1^2(Q^2) + \tau F_2^2(Q^2)\right)\cos^2\frac{\theta_e}{2} + 2\tau\left(F_1(Q^2) + F_2(Q^2)\right)^2 \sin^2\frac{\theta_e}{2}\right], \end{aligned} \tag{2.8}$$

where $\tau = \frac{Q^2}{4m_p^2}$, and $\alpha \simeq \frac{1}{137}$ is the fine structure constant.

At small momentum transfer (large wavelength) of the virtual photon, the FFs provide information about the size of the proton. At large momentum transfer (short wavelength) of the virtual photon, the behavior of the FFs should follow the scaling laws predicted by PQCD. The momentum transferred to the nucleon by the virtual photon must be shared among the constituent quarks, in order for the nucleon to remain intact, through gluon exchages [21, 22]. Precise knowledge of the FFs in a wide kinematic region allows for the understanding of the proton's structure and dynamics and thus for a systematic study of the strong interaction at different energy scales.

In the time-like (TL) region, the proton FFs are extracted through annihilation channels: $e^+e^- \to p\bar{p}$ (Fig. 2.2) and $p\bar{p} \to e^+e^-$, which involve positive values of the momentum transfer squared (2.9).

$$q^2 = s = (p_1 + p_2)^2 = (k_1 + k_2)^2,\ q^2 > 4m_p^2, \tag{2.9}$$

where p_1 (p_2) and k_1 (k_2) are the four-momenta of the antiproton (proton) and electron (positron), and $4m_p^2$ is the kinematic threshold (th.) of the proton-antiproton pair production. The hermicity of the electromagnetic current operator of the nucleons implies the Schwartz reflection principle for the FFs. This means that the FFs are real in the SL region, while they are complex in the TL region [21].

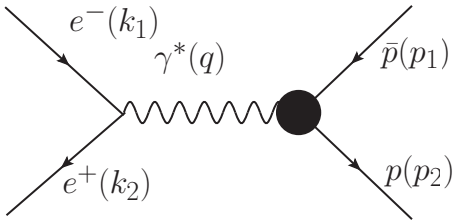

Fig. 2.2: Lowest order Feynman diagram for the proton-antiproton pair production from the electron-positron annihilation.

2.2.1 Sachs form factors

Instead of the Dirac and Pauli FFs, the most general forms of the FFs are the linear combinations of F_1 and F_2, which are the electric and magnetic Sachs FFs, G_E and G_M [26]:

$$\begin{cases} G_E = F_1 - \tau F_2, \\ G_M = F_1 + F_2. \end{cases} \tag{2.10}$$

The differential cross section of the scattering process, Eq. 2.8, becomes the function of G_E and G_M [20]:

$$\left.\frac{d\sigma}{d\Omega_e}\right|_{\text{lab}} = \frac{\alpha^2}{4E_1^2 \sin^4(\theta_e/2)} \frac{E_1}{E_2} \times \left(\frac{G_E^2(Q^2) + \tau G_M^2(Q^2)}{1+\tau} \cos^2\frac{\theta_e}{2} + 2\tau G_M^2(Q^2) \sin^2\frac{\theta_e}{2} \right). \tag{2.11}$$

In a particular Lorentz frame, the Breit frame, the hadrons' momenta $\mathbf{p}_1 = -\mathbf{p}_2 = -\frac{\mathbf{q}}{2}$.

In this frame, the FFs' three-dimensional Fourier transforms are considered to be the proton charge and magnetic moment distributions, which are directly represented by Sachs FFs, G_E and G_M, respectively [20]. As mentioned in Section 2.1, when the momentum transfer squared is in the non-relativistic limit ($Q^2 = -q^2 \to 0$), the radii of the charge and magnetic moment distributions can be extracted from the electric and magnetic FFs of the proton:

$$\begin{cases} < r_E^2 >= 6 \frac{dG_E(Q^2)}{dQ^2}|_{Q^2=0}, \\ < r_M^2 >= 6 \frac{dG_M(Q^2)}{dQ^2}|_{Q^2=0}. \end{cases} \tag{2.12}$$

2.2.2 Boundary and asymptotic behavior

The bold vertex in Fig. 2.2 symbolizes the sum of all the electromagnetic contributions. As a consequence of the optical theorem (unitarity), the amplitudes of these diagrams have a discontinuity cut for all q^2 values which allow the virtual photon, getting enough virtual mass $\sqrt{q^2}$, to couple with on-shell intermediate hadronic states. The lightest of such states is $\pi^+\pi^-$, thus the cut covers $q^2 > 4m_\pi^2$ (m_π is the pion mass). The light vector meson resonances are the strongest coupled intermediate states, which represent the main contributions to the FFs and have masses below the threshold of $p\bar{p}$ ($q^2 < 4m_p^2$) [21, 22]. The region below the threshold is called the unphysical region, and the FFs could be accessed through the study of the processes of $\bar{p}p \to \pi^0 l^+ l^-$ and $\bar{p}n \to \pi^- l^+ l^-$ ($l = e, \mu$), at the future $\overline{\text{P}}$ANDA experiment [24, 25].

The Dirac and Pauli FFs are normalized at $q^2 = 0$ according to the proton charge for F_1 and to the anomalous magnetic moment for F_2 by taking into account the non-elementary nature of the proton:

$$\begin{cases} F_1(0) = 1, \\ F_2(0) = \mu_p - 1, \end{cases} \tag{2.13}$$

where $\mu_p = 2.792847351(28)$ is the proton magnetic moment in units of nuclear magnetons. The corresponding normalization of the Sachs FFs at $q^2 = 0$ according to Eq. 2.10 is

$$\begin{cases} G_E(0) = 1, \\ G_M(0) = \mu_p. \end{cases} \tag{2.14}$$

In the TL region, at the threshold of the proton-antiproton pair production, the electric and magnetic FFs are equal: $G_E(4m_p^2) = G_M(4m_p^2)$, which follows from Eq. 2.10 with $\tau = 1$.

According to the pQCD theory, dimensional counting rules apply to the proton FFs in the SL region, which acquire a power-law asymptotic behavior [21, 28]:

$$\lim_{q^2 \to -\infty} G_{E,M}(q^2) \sim (-q^2)^{-2}. \tag{2.15}$$

The asymptotic behavior in the TL region is obtained by considering the analyticity and boundedness of the proton FFs [22], from which it follows:

$$\lim_{q^2 \to \infty} G_{E,M}(q^2) \sim (q^2)^{-2}. \tag{2.16}$$

Based on the unitarity and analyticity, dispersion relations give an unified framework for the description of the FFs in the whole kinematic region $-\infty < q^2 < \infty$, including the unphysical region.

2.3 Proton form factors in the time-like region

The proton form factors have been explored in the SL region by the elastic ep scattering experiments with high accuracy. Due to the low luminosity collected in the past decades, only few data exist for the proton FFs in the TL region and only a very coarse determination of the ratio (modulus) of the FFs has been possible so far. This section will briefly review the experimental techniques to study the proton FFs as well as the status of the measurments of the proton FFs in the TL region.

2.3.1 Direct e^+e^- annihilation process

The proton FFs can be measured in the TL region through the annihilation reactions $e^+e^- \leftrightarrow p\bar{p}$ using the energy-scan technique, in which the center-of-mass (cms) energy ($\sqrt{s}$)

of the initial state is varied systematically, and at each energy point a measurement of the associated cross section is performed.

In the Born approximation, the differential cross section for the annihilation reaction $e^+e^- \to p\bar{p}$, assuming one photon exchange in the cms frame, is expressed as a function of the proton electromagnetic FFs [27]

$$\frac{d\sigma}{d\cos\theta} = \frac{\pi\alpha^2\beta\mathcal{C}}{2q^2}[(1+\cos^2\theta)|G_M|^2 + \frac{1}{\tau}\sin^2\theta|G_E|^2], \tag{2.17}$$

where α is the electromagnetic coupling constant and θ is the angle of the proton. The phase-space factor, $\beta = \sqrt{1-1/\tau}$, is the velocity of the proton, $\tau = q^2/4m_p^2$ is an inverse helicity suppression factor and m_p is the proton mass. The constant $\mathcal{C}$ stands for the s-wave Sommerfeld-Gamow factor [29–31] by taking into account the electromagnetic interaction in the final state. It can be expressed as a product between an enhancement factor ε and a resummation term $\mathcal{R}$, i. e., the so called Sommerfeld-Schwinger-Sakharaov rescattering formula [30–32]:

$$\mathcal{C} = \varepsilon \times \mathcal{R}, \tag{2.18}$$

where the enhancement factor is

$$\varepsilon = \frac{2m_p}{q}\frac{\pi\alpha}{\beta}, \tag{2.19}$$

and the resummation term is

$$\mathcal{R} = \frac{1}{1-exp(-\varepsilon)}. \tag{2.20}$$

Close to the threshold, $q \sim 2m_p$, the enhancement factor is approximately $\frac{\pi\alpha}{\beta}$. In the limit $\beta \to 0$, the Coulomb factor behaves like the enhancement factor $\mathcal{C} \sim \varepsilon$, so that the factor β in Eq. 2.17 is cancelled and the cross section is expected to be finite at the threshold. With the increase of q above the threshold, the Coulomb factor decreases to $\sim$1 rapidly, thus the cross section is barely affected by the Coulomb factor.

Integrating over the full angular distribution range in Eq. 2.17, the total cross section is,

$$\sigma(q^2) = \frac{4\pi\alpha^2\beta C}{3q^2}[|G_M|^2 + \frac{1}{2\tau}|G_E|^2]. \tag{2.21}$$

The measurement of the differential cross section (Eq. 2.17) at a fixed energy allows for determination of the ratio of proton FFs, $R_{em} = |G_E|/|G_M|$. With precise knowledge of the normalization and the luminosity, a separate determination of $|G_E|$ and $|G_M|$ is possible. The quantity usually measured when the angular distributions cannot be precisely studied (due to the low statistics) is an effective FF, introduced as a linear combination of $|G_E|^2$ and $|G_M|^2$:

$$|G_{\text{eff}}| = \sqrt{\frac{2\tau|G_M|^2 + |G_E|^2}{2\tau+1}}. \tag{2.22}$$

One can define a point-like cross section (Fig. 2.3), $\sigma_{\text{point}}(q^2)$, according to the total cross section (Eq. 2.21) and the effective FF (Eq. 2.22):

$$\sigma_{\text{point}}(q^2) = \frac{4\pi\alpha^2\beta C}{3q^2}[1 + \frac{1}{2\tau}] \tag{2.23}$$

and the total cross section becomes

$$\sigma(q^2) = \frac{4\pi\alpha^2\beta C}{3q^2}[1 + \frac{1}{2\tau}]|G_{\text{eff}}|^2 = \sigma_{\text{point}}(q^2)|G_{\text{eff}}|^2. \tag{2.24}$$

At the threshold (τ=1), the point-like cross section for the proton-antiproton pair prodocution is reduced to a finite value:

$$\sigma_{\text{point}}(q^2 = 4m_p^2) = \frac{4\pi\alpha^2}{3q^2} \times \frac{3\pi\alpha}{2} = 0.848 \text{ nb}. \tag{2.25}$$

Most of the previous experiments were limited by the statistics and only measured the effective FF of the proton, which was extracted from the total cross section (Eq. 2.21) based on (or equivalent to) an assumption of $|G_E| = |G_M|$. The effective FF indicates how much the experimental proton-anitproton pair cross section differs from a point-like one.

2.3.2 Radiative corrections

Generally, the Born cross section of $e^+e^- \to p\bar{p}$ (Fig. 2.2) cannot be measured experimentally due to distorting by higher order processes, as shown in Fig. 2.4.

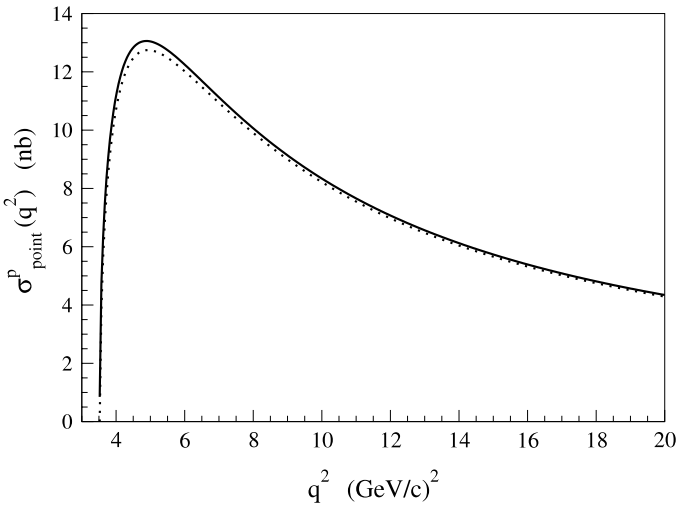

Fig. 2.3: Point-like proton cross section given by Eq. 2.23; he dashed line is the point-like neutron cross section [31].

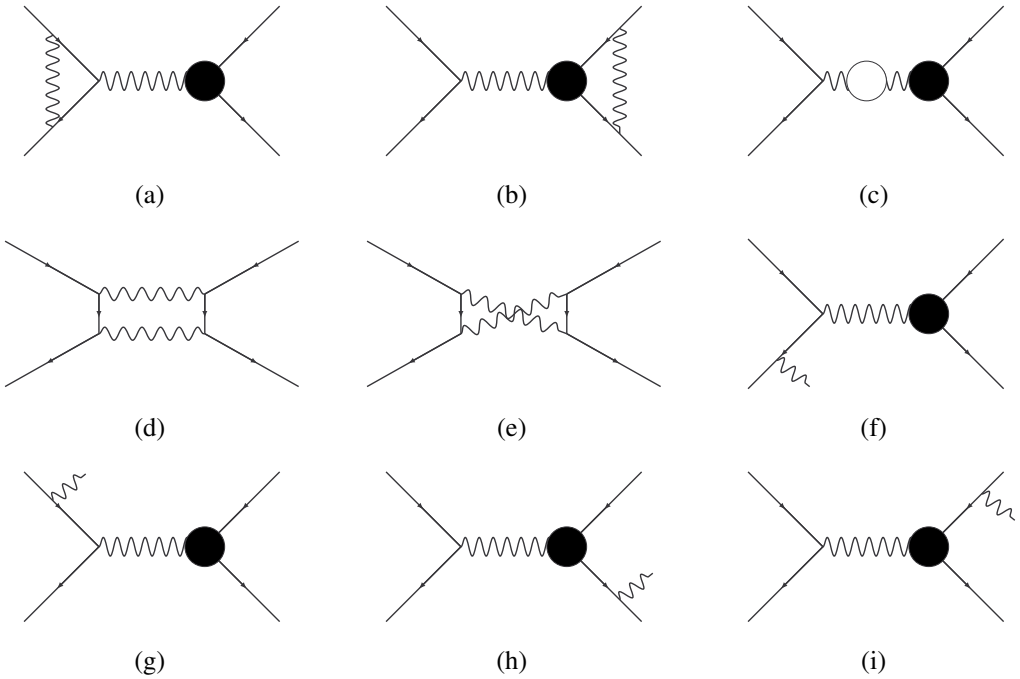

Fig. 2.4: Feynman diagrams for the first-order radiative corrections to $e^+e^- \to p\bar{p}$.

The observed cross section ($d\sigma_{\text{obs}}$) from a experiment is different from the Born cross section ($d\sigma_B$) [49, 50]:

$$d\sigma_{\text{obs}} = d\sigma_B \times (1+\delta), \tag{2.26}$$

where (1+δ) is the radiative correction factor obtained through the theoretical calculation. The radiative corrections contain:

- the virtual corrections from the interference between the Born process (Fig. 2.2) and the processes with one virtual photon emission (Fig. 2.4) including lepton vertex (a), hadron vertex (b), vacuum polarization (c) and two-photon exchange (d and e);

- the bremsstrahlung corrections from the processes with a real photon emission in the initial and final states, Fig. 2.4 (f) - (i).

When the calculation is performed, the bremsstrahlung corrections are usually separated into two contributions: (1) the soft photon contribution with the emitted photon energy up to an infrared cut-off parameter (ω) where the soft photon approximation holds, (2) the hard photon contribution with the emitted photon energy from ω up to an experimental cut depending on the energy resolution of the detector. This separation is usually arbitrary and the total radiative correction does not depend on the infrared cut-off. The infrared sigularities, led by the bremsstrahlung corrections, are cancelled order by order by the virtual corrections [50]. Additionally, the self-energy corrections (virtual photon emission and re-absorption from the same particle) renormalize the mass (energy) of the particles. These corrections are cancelled in the total correction considering the ultraviolet divergences. More details of such calculations can be found in the references [49, 50].

2.3.3 Initial-state-radiation process

Because the e^+e^- annihilation is mostly accompanied by emission of one or several photons from the initial state, the high luminosity collected at the main resonances in the e^+e^- collider experiments provides a complementary approach to the energy-scan technique. Since events with initial-state-radiation (ISR) photons lead to a reduction in momentum transferred by the virtual photon and hence a reduction of the invariant mass of the final state,

the ISR process allows for measurement of the hadronic FFs over a wide kinematic range below the cms energy of the initial state ($\sqrt{s}$).

In the case of $e^+e^- \to p\bar{p}\gamma$, the emission of a photon in the initial state gives rise to the possibility of measuring the cross section of the $e^+e^- \to p\bar{p}$ process over a wide range of cms energies, from the threshold $\sqrt{q^2} = 2M_p$ (1.877 GeV/c^2) up to $\sqrt{s}$. The measurement of the cross section exactly at threshold in the $e^+e^- \to p\bar{p}$ process is in practice impossible, since the outgoing particles, produced at rest in the laboratory system, do not reach the detector. The ISR technique is the only method for accessing the threshold in an e^+e^- annihilation because the $p\bar{p}$ system is not produced at rest, but boosted in the opposite direction to the ISR photon.

The Born cross section for the $e^+e^- \to p\bar{p}\gamma$ reaction (Fig. 2.5), integrated over the nucleon momenta, is given by

$$\begin{cases} \frac{d\sigma_{e^+e^- \to p\bar{p}\gamma}(q^2)}{dq^2} = \frac{1}{s} W(s,\, x)\sigma_{p\bar{p}}(q^2), \\ W(s,\, x) = \frac{\alpha}{\pi x}(\ln\frac{s}{m_e^2} - 1)(2 - 2x + x^2), \end{cases} \tag{2.27}$$

where $x = \frac{2E_\gamma^*}{\sqrt{s}} = 1 - \frac{q^2}{s}$ and E_γ^* is the ISR photon energy in the e^+e^- cms frame. The radiator function $W(s,\, x)$ [44–48] is the probability of ISR photon emission and m_e is the electron mass.

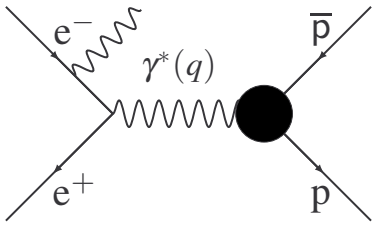

Fig. 2.5: Lowest order Feynman diagram for the process $e^+e^- \to p\bar{p}\gamma$

The ratio of proton FFs, $R_{em} = |G_E|/|G_M|$, can be determined from the distribution of θ_p, the angle between the proton momentum in the $p\bar{p}$ rest frame and the momentum of the $p\bar{p}$ system in the e^+e^- cms frame (the helicity of the proton). This distribution can be expressed as a sum of terms proportional to $|G_E|^2$ and $|G_M|^2$.

2.3.4 Status of proton form factors in the time-like region

The first experiment to measure the cross section of $e^+e^- \to p\bar{p}$ and the effective FF of the proton was performed at the Adone storage ring in Frascati in 1973 [33]. Over the past fourty years, the $e^+e^- \to p\bar{p}$ channel has been studied by different experiments. Up to 2015, the total luminosity accumulated through energy scans between 1.900 to 3.671 GeV amounts to around 188 pb^{-1}. A summary of the different experiments using the energy-scan technique to measure $e^+e^- \to p\bar{p}$ is presented in Tab. 2.1.

Tab. 2.1: Summary of different experiments using the energy-scan technique to measure $e^+e^- \to p\bar{p}$, and $\mathcal{L}_{\text{int}}$ is the integrated luminosity.

Experiment	Year Publ.	Scan Points	$\sqrt{s}$ Range [GeV]	$\mathcal{L}_{\text{int}}$ [pb^{-1}]	Events	Ref.
Adone 73	1973	1	2.1	0.2	25	[33]
FENICE	1993	1	2.1	< 0.1	28	[34]
FENICE	1994	4	1.9 - 2.4	0.3	70	[35]
FENICE	1998	1	2.1	< 0.1	7	[36]
DM1	1979	4	1.925 - 2.180	0.4	~ 70	[37]
DM2	1983	6	1.975 - 2.250	0.5	~ 100	[38]
DM2	1990	1	2.4	0.2	4	[39]
CLEO-c	2005	1	3.671	21	16	[40]
BESII	2005	10	2.00 - 3.07	5	80	[41]
BESIII	2015	12	2.2324 - 3.6710	159.6	1368	[42]
CMD-3	2015	12	1.89 - 2.00	6.976	2862	[43]

- The non-magnetic detector of FENICE was designed with the original goal of measuring the neutron FFs at the Adone storage ring. The main components were Limited Streamer Tubes as tracking system and Scintillation Counters as timing and trigger system. The effective FF of the proton was measured from the cms energy 1.9 GeV up to 2.4 GeV [33–36].

- The effective FF of the proton was measured in the cms energy range of 1.925 GeV to 2.400 GeV with the DM1 and DM2 detectors at the Orsay colliding beam facility from

1979 to 1990. A total luminosity of 1.1 pb^{-1} was collected at 11 energy points and the proton effective FF was extracted with around 170 $p\bar{p}$ total events [37–39].

- The CLEO-c detector, installed at the Cornell Electron Storage Ring, had 93% coverage of the solid angle for both the charged- and neutral-particle identification. Only a single energy point was analyzed with the luminosity of 21 pb^{-1} at 3.671 GeV to measure the cross section of $e^+e^-\to p\bar{p}$ and the effective FF of the proton [40].

- The BESII detector, operated at the BEPC collider, collected 5 pb^{-1} of luminosity at the cms energies between 2.00 to 3.07 GeV to measure the cross section of $e^+e^-\to p\bar{p}$ and the effective FF of the proton [41]. After the upgrades of the detector and collider, the BESIII detector started to take data in 2009 at the BEPCII collider. The result of the $e^+e^-\to p\bar{p}$ measurement at the energy range of 2.2324-3.6710 GeV was published in 2015 with the total luminosity of 160 pb^{-1} mainly collected for the R ($\frac{\sigma_{\text{hadrons}}}{\sigma_{\mu^+\mu^-}}$) value measurement (R-Scan). The ratio ($\frac{|G_E|}{|G_M|}$) of the proton FFs as well as the magnetic FF ($|G_M|$) was extracted at three energy points with high luminosities [42]

- The CMD-3 detector at the electron-positron collider VEPP-2000 collected large luminosity below 2.0 GeV. The tracking system of the detector consists of a cylindrical drift chamber and a double-layer, cylindrical, multiwire proportional Z-chamber inside a superconducting solenoid with a 1.3-T field. The cross section was measured at the energy points very close to the threshold. Combining the data collected between 1.92 GeV and 2.00 GeV, the ratio of proton FFs was extracted with a statistical precision of 15% [43].

In the last decades, the proton FFs and their ratio were aslo measured with the crossing symmetry channel $p\bar{p}\to e^+e^-$ by the experiments of E760 [51] and E835 [52, 53] at Fermi Lab and PS170 [54] at CERN.

Except for the direct annihilation experiments, the proton FFs were studied by the BABAR collaboration through the ISR technique in a wide kinematic range [46–48]. A total luminosity of 469 pb^{-1} was collected at the cms energy of 10.58 GeV with the BABAR detector at SLAC. Two analyses, tagged and untagged, were performed in different $p\bar{p}$ invariant-mass ranges.

The tagged analysis, which required the ISR photon to be detected, found in total 7876 $e^+e^- \to p\bar{p}$ events from the threshold up to 4.5 GeV/c^2. The ratio of proton FFs was extracted in the tagged analysis from the threshold up to 3.0 GeV/c^2. The untagged analysis collected in total 140 events with the ISR photon escaping into the beam pipe from 3.0 GeV/c^2 to 6.5 GeV/c^2. It is not possible to access the threshold (lower invariant-mass region) by the untagged analysis. When the ISR photon is emitted into the beam pipe, the hadronic system is emitted into the opposite beam pipe. For the untagged photon emitted with a very high momentum, which corresponds to the hadronic system with a very low invariant mass, the opening angle between the proton and antiproton is very small and thus both or one of the hadrons cannot reach the detector volume.

The world data on the cross section of $e^+e^- \to p\bar{p}$ are shown in Fig. 2.6 (a), while the data on the effective FF of the proton in the TL region are shown in Fig. 2.6 (b) from both processes of the e^+e^- and $p\bar{p}$ annihilation.

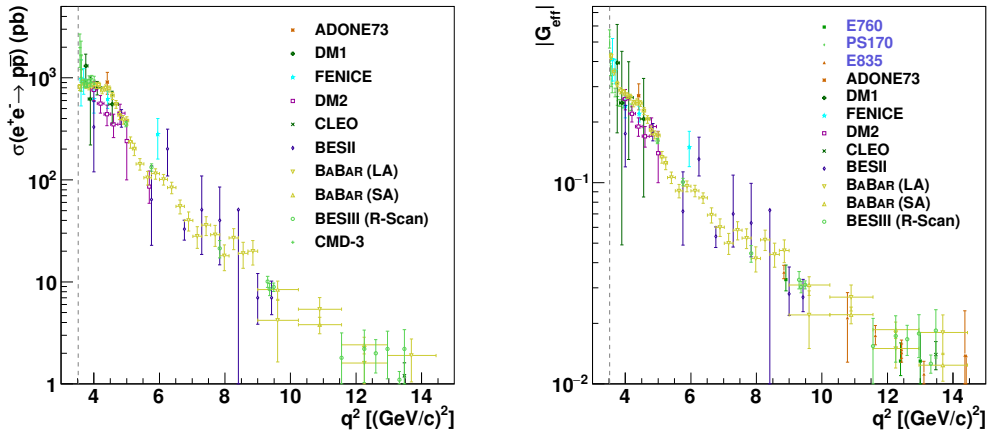

(a) The cross section of $e^+e^- \to p\bar{p}$

(b) The effective FF of the proton

Fig. 2.6: World data on the cross section of $e^+e^- \to p\bar{p}$ and the effective FF of the proton, as a function of q^2: (a) The cross section measured by $e^+e^- \to p\bar{p}$, (b) The effective FF of the proton including $p\bar{p} \to e^+e^-$ experiments.*

The ratio of proton FFs were extracted in four experiments, PS170 [54], BABAR [46, 47], BESIII [42] and CMD-3 [43]. However, an obvious discrepancy exists between the results

*LA: Large (polar) Angle of the ISR photon; SA: Small (polar) Angle of the ISR photon.

of PS170 and BABAR in the lower q^2 range. In a higher q^2 range, the results from BABAR and BESIII (R-Scan) are consistent with large uncertainties, see Fig. 2.7 (a). In addition, R. Baldini and his colleagues determined the upper and lower limits of the ratio for two data points based on the results from FENICE, DM1 and E835 [55].

The individual magnetic FF ($|G_M|$) of the proton, extracted by PS170 [54] and BESIII [42], is shown in Fig. 2.7 (b).

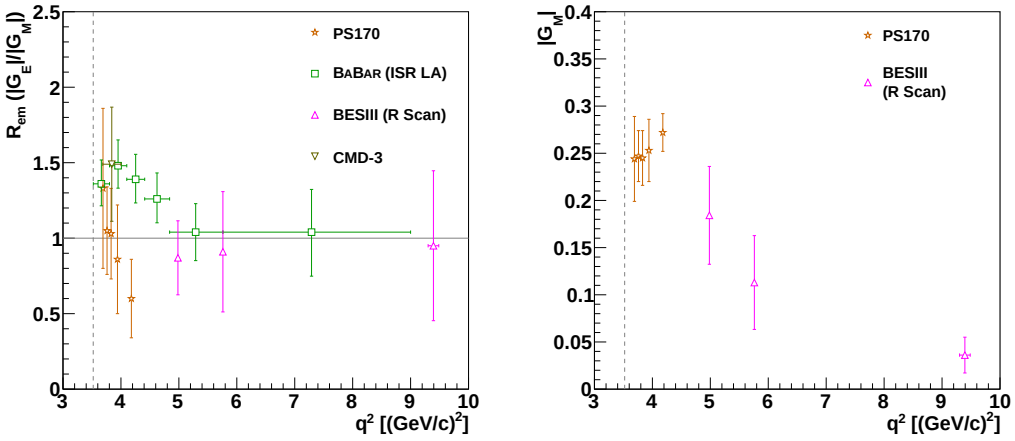

(a) Ratio of proton FFs

(b) Magnetic FF

Fig. 2.7: World data on the ratio of proton FFs and the proton magnetic FF as a function of q^2: (a) the ratio of proton FFs, (b) the proton magnetic FF ($|G_M|$).

2.4 Theoretical models on proton form factors

In the past decades, many theoretical efforts have been made to explain the existing data in the SL region. Different models have been developed to describe the dynamical structure of hadrons but not all of them can apply to all four nucleon FFs or be extended in the TL region. In this section, the theoretical predictions based on the Vector Meson Dominance (VMD) model and PQCD are shortly reviewed. More theoretical models, such as chiral perturbation theory and constituent quark models, were reviewed in [13] and [21].

2.4.1 Vector meson dominance model

The VMD models were built through the idea that a photon interacts with the nucleon through the exchange of an intermediate vector meson (ρ, ω, ϕ, ...) with the same quantum numbers as the photon ($J^{PC} = 1^{--}$, total spin 1 and odd parity). These models allow to reproduce the data, even in the high q^2 region by giving a simple parametrization of the nucleon FFs through a limited number of parameters with physical meaning as masses and coupling constants [21].

In 1973, a VMD-based model for a "semi-phenomenological" description of the SL nucleon FFs was proposed by Iachello, Jackson and Landé [56], predicting a linear decrease of the ratio of proton FFs. The model has been further developed by including a more accurate TL complex structure [57–59]. The nucleon FFs are parametrized as the product of an intrinsic FF, $g(q^2)$, and the terms describing the interaction of the nucleon with the photon by taking into account the different coupling to the isovector (ρ, ...) and isoscalar (ω, ϕ, ...) vector mesons. The expressions for the Dirac and Pauli FFs (Eq. 2.5) in this model are:

$$\begin{cases} F_1(q^2) = F_1^V(q^2) + F_1^S(q^2), \\ F_2(q^2) = F_2^V(q^2) + F_2^S(q^2), \end{cases} \tag{2.28}$$

where $F_{1,2}^V(q^2)$ and $F_{1,2}^S(q^2)$ are the isovector and isoscalar FFs, respectively. They have the following expressions [21]:

$$\begin{cases} F_1^V(q^2) = \frac{1}{2} g(q^2) \left(1 - \beta_\rho + \frac{\beta_\rho}{D_\rho(q^2)} \right), \\ F_2^V(q^2) = \frac{1}{2} g(q^2) \left(\frac{3.706}{D_\rho(q^2)} \right), \\ F_1^S(q^2) = \frac{1}{2} g(q^2) \left(1 - \beta_\omega \frac{q^2}{m_\omega^2 + q^2} - \beta_\phi \frac{q^2}{m_\phi^2 + q^2} \right), \\ F_2^S(q^2) = \frac{1}{2} g(q^2) \left((-0.120 - \alpha_\phi) \frac{m_\omega^2}{m_\omega^2 + q^2} + \alpha_\phi \frac{m_\phi^2}{m_\phi^2 + q^2} \right). \end{cases} \tag{2.29}$$

The function $g(q^2)$ is the intrinsic FF considered as the dipole:

$$g(q^2) = \frac{1}{(1 - \gamma e^{i\theta} q^2)^2} \tag{2.30}$$

where $\gamma = 0.25$ (GeV/c)$^{-2}$ as in the SL region [57], and a phase angle is introduced to account for the complex structure of the FFs in the TL region.

The function $D_\rho(q^2)$ is a propagator accounting for the finite width of ρ meson and is normalized as $D_\rho(0) = 1$ [21, 57]:

$$\frac{1}{D_\rho(q^2)} = \frac{m_\rho^2 + 8\Gamma_\rho m_\pi/\pi}{m_\rho^2 - q^2 + (4m_\pi^2 - q^2)\Gamma_\rho \alpha(q^2)/m_\pi}, \tag{2.31}$$

in the TL region $q^2 \geq 4m_\pi^2$, with

$$\alpha(q^2) = \frac{2}{\pi}\sqrt{\frac{q^2 - 4m_\pi^2}{q^2}} ln\left(\frac{\sqrt{q^2 - 4m_\pi^2} + \sqrt{q^2}}{2m_\pi}\right). \tag{2.32}$$

The contributions from the ω and ϕ mesons are included as simple real poles in Eq. 2.29 considering the very narrow widths of these resonances. The four coupling constants were set as $\beta_\rho = 0.672$, $\beta_\omega = 1.102$, $\beta_\phi = 0.112$ and $\alpha_\phi = -0.052$ in Ref. [56].

2.4.2 Perturbative QCD parametrization

As mentioned in Section 2.2, the asymptotic behavior of the proton FFs is predicted by PQCD at large momentum transfer. Figure 2.8 shows the lowest order PQCD diagram describing the interaction between the virtual photon and the proton at quark level in the ep elastic scattering process. The momentum transferred by the virtual photon is shared by the quarks through the gluon exchange [21, 60, 61].

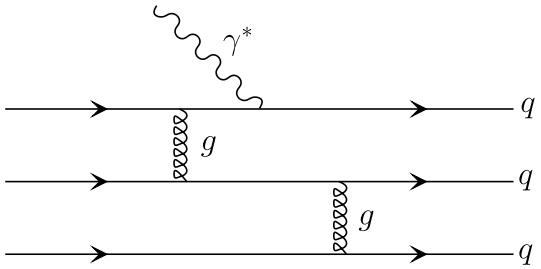

Fig. 2.8: The lowest order diagram describing the ep elastic scattering process in PQCD [21].

The differential cross section for the exclusive scattering process of the two particles collision at high momentum transfer squared (t) reads

$$\left(\frac{d\sigma}{dt}\right)_{\mathrm{AB}\to\mathrm{CD}} \propto s^{-n+2} f\left(\frac{t}{s}\right), \tag{2.33}$$

where n is the total number of the fields in the initial (A and B) and final (C and D) states, and the function $f\left(\frac{t}{s}\right)$ depends on the scattering angle.

Generally, it is very difficult to predict the absolute cross section of the exclusive processes in the QCD frame. The FFs of the proton are proportional to the strong coupling constant $\alpha_s(Q^2)$, depending on the number of the valence quarks involved (exchanged gluons) in the process of Fig. 2.8. In the SL region, the strong coupling constant $\alpha_s(Q^2)$ is determined as [62]:

$$\alpha_s(Q^2) = \frac{4\pi}{\beta \ln(Q^2/\Lambda^2_{\mathrm{QCD}})}, \tag{2.34}$$

where Λ_{QCD} ($Q^2 \gg \Lambda_{\mathrm{QCD}}$) is the QCD scale constant, and β equals $11 - \frac{2}{3}n_f$, with n_f the number of flavors. The proton FFs, $G_E(Q^2)$ and $G_M(Q^2)$, must have the same $\frac{1}{Q^2}$-dependence and are proportional to the strong coupling constant:

$$G_E(Q^2) = G_M(Q^2) \simeq \frac{\alpha_s^2(Q^2)}{(Q^2)^2} = \frac{\alpha_0^2}{Q^4 \ln^2(Q^2/\Lambda^2_{\mathrm{QCD}})}, \tag{2.35}$$

where the constant α_0 can be obtained by a fit on the experimental data.[†]

To extend the pQCD parametrization to the TL region analytically, the momentum transfer squared, $q^2 \gg \Lambda^2_{\mathrm{QCD}}$, is positive and the term of the logarithmic function is replaced as following:

$$\ln(Q^2/\Lambda^2_{\mathrm{QCD}}) \to \ln(q^2/\Lambda^2_{\mathrm{QCD}}) - i\pi. \tag{2.36}$$

The modulus of the proton FFs is written as:

$$|G_{E,M}(Q^2)| = \frac{C}{q^4\left(\ln^2(q^2/\Lambda^2_{\mathrm{QCD}}) + \pi^2\right)}, \tag{2.37}$$

where the coefficient C and the scale constant Λ_{QCD} can be obtained by fitting the experi-

[†]The similar expression of $G_{\mathrm{eff}}(Q^2)$ in the Ref. [21] (Eq. 116) has a mistyping of a power 2 for the coupling constant as well as for the logarithmic function [63].

mental data in the TL region, and are suggested to be 72 GeV^{-4} and 0.52 GeV[‡], respectively, in the Ref. [64].

This simple model of the PQCD parametrization assumes that the relative phase angle between G_E and G_M is zero, which needs to be verified through the relative phase measurement in experiments using polarization observables.

[‡]The unit of Λ^2 should be same as q^2. The unit of Λ given in the Ref. [64] has a typo of the power 2 [65].

CHAPTER 3

BEPCII Collider and BESIII Spectrometer

The original Beijing Electron Positron Collider (BEPC) and its detectors, the Beijing Spectrometer (BES) and the upgraded BESII, operated from 1989 to 2004 in the τ-charm energy region [66–68]. As a single-ring electron-positron storage ring with single bunch mode, the instantaneous luminosity of the BEPC reached approximately 10^{31} cm^{-2}s^{-1} before it was shut down.

BEPCII, which is the second-phase construction of the BEPC, is a double-ring multi-bunch collider with a design luminosity of 1×10^{33} cm^{-2}s^{-1} at the optimized beam energy of 1.89 GeV. The collider is running at the cms energy range from 2.0 GeV to 4.6 GeV for the study of τ-charm physics. The upgraded spectrometer, BESIII (Beijing Spectrometer III), is operated at the BEPCII with a nearly 4π (93%) acceptance [69, 71]. The physics goals of the BESIII experiment include:

- Precision measurements of QCD parameters.
- Tests of electroweak interactions with very high precision in both the quark and the lepton sectors.
- Studies of light hadron spectroscopy and decay properties with high statistics, and search for glueballs, hybrids, and exotic states.

- Studies of the production and decay properties of charmonium states with high statistcs.
- Studies of charm physics including the decay properties of charmed mesons and baryons.
- τ-physics studies.
- Search for new physics by studying rare and forbidden decays, oscillations and CP (charge conjugation parity) violations in c-hadron and τ-lepton sectors.

3.1 Beijing electron positron collider II

In July 2008, BEPCII was first operated in collision mode, and physics data-taking started in March of 2009. The instantaneous luminosity reached the design luminosity at the cms energy of 2×1.89 GeV in the running period 2015-2016, which is an improvement of a factor of 100 compared to its predecessor, BEPC. This luminosity is also the new record achieved for such an accelerator in this energy range.

Fig. 3.1: Aerial view of the BEPCII facility. The figure is taken from *http://english.ihep.cas.cn/*.

The BEPCII collider consists of a 202.0 m long linac and two 273.5 m long storage rings [72], an aerial view of the facility is shown in Fig. 3.1. The electron and positron beams can be accelerated up to 1.89 GeV for injection into the storage rings by the linac consisting of klystrons, an electron gun and a positron source. The electron and positron injection rates can reach 200 mA/min, while the positron injection rate can reach 50 mA/min. BEPCII

is operated in multi-bunch mode with 93 bunches stored in each ring with a space of 8 ns (6 ns for energry-scan data-taking in 2015) or 2.4 m. Positrons and electrons collide at the interaction point with a horizontal crossing angle of ± 11 mrad. The single-beam current was designed to be 910 mA in the collider mode. A micro-β technique using superconducting quadrupole magnets placed very close to the interaction point was applied to improve the luminosity. Table 3.1 summarizes the design parameters of BEPCII.

Tab. 3.1: Designed parameters of the BEPCII collider.

Parameters	BEPCII
Beams cms energy (GeV)	2.0 - 4.6
Circumference (m)	237.5
Number of rings	2
RF frequency f_{rf} (MHz)	499.8
Peak luminosity ($cm^{-2}s^{-1}$)	$\sim 10^{33}$
Number of bunches	2×93
Bunch spacing (ns/m)	8/2.4
Bunch length σ_z (cm)	1.5
Bunch width σ_x (μm)	$\sim$380
Bunch height σ_y (μm)	$\sim$5.7
Beam current (mA)	2×910
Relative energy spread	5×10^{-4}
Crossing angle (mrad)	± 11

3.2 Beijing spectrometer III

Figure 3.2 shows the main components of the spectrometer. The multilayer drift chamber (MDC) surrounds the beryllium beam pipe, and the end plates of the MDC inner chamber have a stepped conical shape in which two superconducting quadrupoles (SCQ) are inserted. Including a barrel and two end caps, the time-of-flight (TOF) system is located outside the MDC barrel and end caps. The TOF barrel consists of two layers of plastic scintillator counters, while each end cap of the TOF has a single layer. The CsI(Tl) electromagnetic calorimeter (EMC) is placed outside of the TOF system and inside the superconducting

solenoid magnet (SSM). The coil of the SSM has a mean radius of 1.482 m and length of 3.52 m, with the steel plates of the flux return yoke outside. The muon counter (MUC) consists of layers of resistive plate chambers (RPCs) inserted in gaps between the steel plates. Furthermore, the sub-detectors MDC, TOF and EMC provide information to the level 1 (L1) trigger system. The solid-angle coverage of the spectrometer is $\Delta\Omega/4\pi = 0.93$. The polar angle (θ in Fig. 3.2) of the spectrometer, which is defined with respect to the horizontal direction of the positron beam, covers from 21° to 159°. Table 3.2 shows the summary of the subsystem parameters of the BESIII spectrometer.

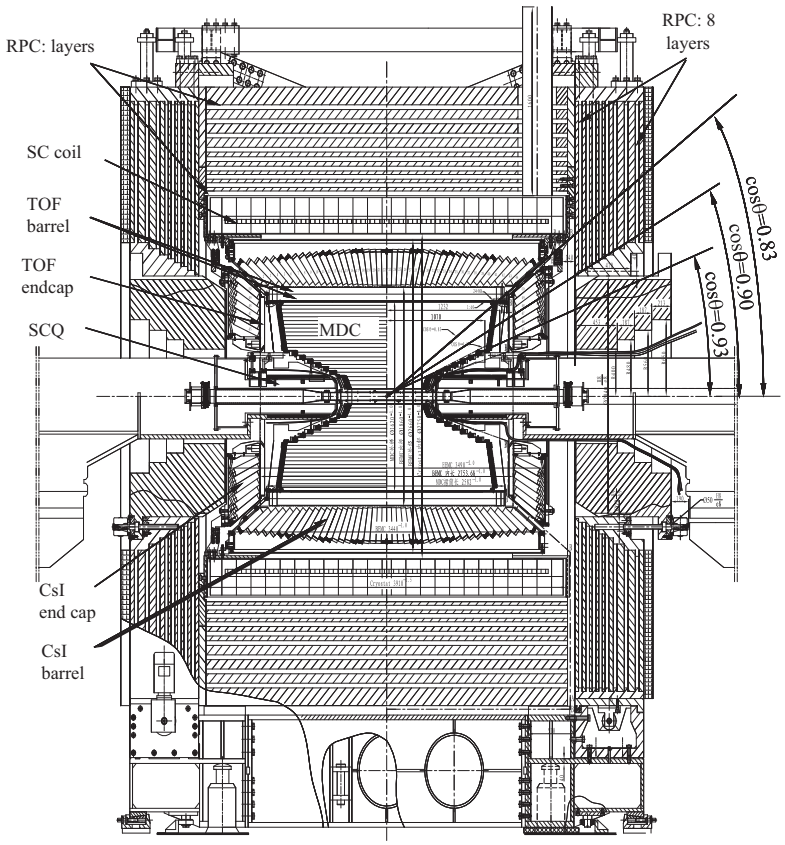

Fig. 3.2: Schematic drawing of the BESIII detector. The electron and positron beams collide in the center along the horizontal beam pipe.

Tab. 3.2: Parameters of the BESIII detector.

Subsystem		Parameter
MDC	single wire $\sigma_{r\phi}$ (μm)	130
	σ_p/p (1.0 GeV/c) (%)	0.5
	σ (dE/dx) (%)	6
EMC	σ_E/E (1.0 GeV) (%)	2.5
	position resolution (1.0 GeV) (cm)	0.6
TOF	barrel σ_T (ps)	100
	end cap σ_T (ps)	110
MUC	No. of layers (barrel/end cap)	9/8
	cut-off momentum (MeV/c)	0.4
solenoid magnet field (T)		1.0
solid-angle coverage $\Delta\Omega/4\pi$		0.93

3.2.1 Multilayer drift chamber

The multilayer drift chamber was optimized for effectively tracking the relatively low-momentum particles produced in the τ-charm energy region with an excellent momentum resolution and a good measurement of the ionization energy loss (dE/dx). Signals are also produced by the MDC for the L1 trigger system to select physics events and suppress background.

The MDC inner radius is 59 mm and the outer radius is 810 mm. A helium-based gas mixture He/C_3H_8 (60/40) is used to minimize the effect of multiple scattering while maintaining a reasonable dE/dx resolution. A stepped conical shape was designed for the end plates of the inner chamber to place the final focusing quadrupole as close as possible to the interaction point (IP). The single-cell position resolution is better than 130 μm in the $r-\phi$ plane. In the beam direction at the vertex, the position resolution is around 2 mm measured by stereo wires with stereo angles from -3.4° to +3.9°. The transverse momentum resolution is better than 0.5% at 1.0 GeV/c in a 1-T magnetic field of the solenoid, and the resolution of the dE/dx measurement is better than 6.0% for particles with an incident angle of 90°. A short summary of the main functions of the BESIII MDC is listed below:

- Reconstruct charged tracks in 3D space.

- Determine the momentum of charged particles.
- Measure dE/dx to identify charged particles.
- Recontruct long-lived hadrons (mainly K_S^0 and Λ) decaying in the MDC volume.
- Provide the L1 trigger signal based on reconstructed charged tracks and reject background tracks.
- Provide extrapolated tracks for the outer detector components.

3.2.2 Time-of-flight system

The TOF system consists of a double-layer barrel and two single-layer end caps, which are based on plastic scintillation counters read out by fine mesh photomultiplier tubes. The double-layer barrel placed between the MDC and EMC has 176 plastic scintillation counters (BC-408, 88 for each layer). The length of the scintillator bars for the barrel is 2300 mm, and the bar's cross section is trapezoidal with a thickness of 50 mm. Two fine mesh photomultiplier tubes (PMTs) are attached to the two ends of the bars and coupled by 1-mm silicone pads. Two single-layer end caps, with 48 fan-shaped scintillation counters each (BC-404), are placed outside the MDC end caps. Each scintillator is 480 mm long and 50 mm thick, its width is 62 and 109 mm at each one of the ends. The inside end (smaller width) of the scintillator is cut at 45° to reflect light to the PMT. The PMT is attached to the outside end (larger width) of the scintillator facing the 45° cut surface.

The solid angle coverage is $|\cos\theta| <$0.82 for the barrel and 0.85$< |\cos\theta| <$0.95 for the end caps. The time resolutions are better than 70 ps and 100 ps for the barrel and the end caps, respectively. This allows a 3σ (standard deviation) π/K (pion/Kaon) separation for the track momentum up to approximately 700 MeV/c at 90° in the barrel region. The TOF counter provides signals to the trigger system, which plays a critical role for the detection of charge particles.

3.2.3 Electromagnetic calorimeter

The electromagnetic calorimeter consists of 6240 CsI(Tl) crystals located outside of the TOF counters and inside the coil of the solenoid magnet. The length of each crystal is 28 cm or 15 radiation lengths X_0, and the front face is 5.2 cm $\times$ 5.2 cm. The EMC has an inner radius of 94 cm with a total weight of 25.6 tons. The design energy resolution of the EMC is $\delta E/E$=2.5% at 1.0 GeV, and the position resolution is δ=6 mm/$\sqrt{E}$ (E in GeV), which makes it possible to measure the energy of photons precisely from $\sim$20 MeV to the full beam energy of 2.3 GeV. Furthermore, L1 trigger signals (see Section 3.2.5) are generated by the EMC sub-trigger system based on the total energy, the energy balance in different regions and the number of isolated energy clusters. The polar angle coverage for the EMC barrel is $|\cos\theta| <$0.82, and it is 0.83$< |\cos\theta| <$0.93 for the EMC end caps.

3.2.4 Muon counter

The muon counter consists of resistive plate counters (RPC) interspersed in steel plates of the magnetic-flux return yoke of the solenoid magnet. For the barrel, there are nine layers of RPCs with the first layer placed in front of the first steel plate. The nine layers of steel plates have a total thickness of 41 cm. There are eight layers of RPCs for each end cap, with the first layer placed behind a 4-cm-thick steel plate. As minimum ionizing particles, the average energy loss is about 160 MeV for muons passing through the 28-cm-long CsI(Tl) crystals of the EMC. The minimum muon momentum which can be identified is approximately 0.4 GeV/c at the beginning of the MUC, considering the bending in the solenoid magnetic field.

3.2.5 Trigger, data acquisition and online control systems

The trigger, data acquisition (DAQ) and online computing control systems are designed to accommodate multi-bunches of the beam and high event rate. A nearly dead-time-free operation can be achieved with the readout electronics system. The spectrometer can process a large amount of data in real time with high reliability in a very high-event-rate and high-background-rate environment.

The trigger system has two levels. Level 1 (L1) is based on hardware, and level 3 (L3) is based on software in an online computing farm. The L1 trigger, whose signals are provided by sub-detectors MDC, TOF and EMC, is designed to select good physics events with high efficiency and suppress the cosmic-ray and beam-related background events to a level smaller than 2 kHz, which is the expected physics event rate at J/ψ peak. Once an L1 trigger-acceptance signal is received, data in the buffers of the front-end electronics are read out and transmitted to an online computer farm where event filtering and building are implemented. Data are written into the permanent storage device after background events are further suppressed by the L3 trigger. Based on a global trigger logic, the entire trigger system is operated at 41.65 MHz, synchronized with the accelerator RF frequency of 499.8 MHz.

3.2.6 Luminosity measurement

To achieve the physics goals of BESIII, an accurate measurement of the integrated luminosity plays a crucial role. Three main QED processes, BhaBha, di-muon and di-gamma, are used to determine the luminosity. In the BESIII data-taking, a crude luminosity measurement is applied in real time using mainly the end cap of the EMC for data-quality monitoring. More accurate luminosity measurements are performed with the analysis of data offline, including background elimination and further corrections for detector efficiencies and other effects based on Monte Carlo (MC) simulations. The uncertainties of the accurate luminosity measurements mainly come from trigger efficiency, radiative corrections, MC simulatons and background elimination. An accuracy level of less than 1.0% can be acheived for the integrated luminosity measurement.

3.3 Overview of data sets

The physics data sets taken by BESIII can be classified into two types, large luminosity at resonances for limited energy points, limited luminosity from scan measurements for many energy points. Data sets up to the running period of November 2015 to June 2016 are summarized in Tab 3.3 and Tab. 3.4.

Large luminosity data sets are listed in Tab. 3.3, including the charmonium resonances

and the Y states. The numbers of events are shown for the very narrow resonances J/ψ and ψ', while the online luminosity measurement is quoted for the data set at 4.180 GeV. BESIII has collected the world's largest data sets [78] at the cms energies between J/ψ and 4.6 GeV for different resonances.

Tab. 3.3: Integrated luminosity of the large data sets at resonances.

$\sqrt{s}$ (GeV)	Int. Lumi. (pb^{-1})	Date	Sample
3.097	1.3×10^9 [73]	2009, 2012	J/ψ event number
3.686	0.5×10^9 [74, 75]	2009, 2012	ψ' event number
3.773	2916.94 [76]	2010, 2011	ψ''
4.009	481.96 [77]	2011	$\psi(4040)$
4.180	3000	2016	$\psi(4180)$ (online)
4.230	1047.34 [77]	2013	Y(4260)
4.260	825.67 [77]	2013	Y(4260)
4.360	539.84 [77]	2013	Y(4360)
4.420	1028.89 [77]	2014	Y(4420)
4.600	566.93 [77]	2014	Y(4600)

Different scan data sets were collected for specific purposes, such as the study of the hadronic R ($\frac{\sigma_{e^+e^-\to\text{hadrons}}}{\sigma_{e^+e^-\to\mu^+\mu^-}}$), tau physics, baryon FFs, threshold effects of hadronic productions and lineshapes of resonances. The so called "R-scan" data, mainly dedicated to the measurement of R, were collected in two phases or energy ranges: a low energy range 2.232-3.671 GeV with total luminoisty 156.94 pb^{-1} at 12 energy points [42], and a high energy range 3.800-4.600 GeV with total luminosity around 800 pb^{-1} at 104 energy points. In the running period of 2014-2015, BESIII has collected high-luminosity scan data at 2.000-3.080 GeV for the main purpose of measuring baryon FFs and threshold effects of baryon pair production with unprecedented statistical accuracy. The integrated luminosity at 22 energy points was measured through the BhaBha process to be 651 pb^{-1} [79]. For the data sets from this running period with high luminosities, the staticical uncertainty of the ratio of proton FFs is expected to be below 10%. Table 3.4 summarizes the scan data mentioned above, except for the ones collected around the main resonances for lineshapes studies.

Tab. 3.4: Scan data for the measurement of the hadronic R and bayron FFs.

$\sqrt{s}$ Range (GeV)	Scan points	Int. Lumi. (pb^{-1})	Date	Sample
2.232 - 3.671	12	156.94 [42]	2011	R-scan (τ mass)
3.800 - 4.600	104	800	2014	R-scan (online)
2.000 - 3.080	22	651.09 [79]	2015	Energy scan

CHAPTER 4

Data Sets and Monte Carlo Simulation

As mentioned in Section 3.3, since the first physics run in 2009, BESIII has collected many data sets at the cms energies of different resonances and at many energy-scan points. From the analysis of the scan data collected at different energy points, the proton FFs and the effective FF can be obtained using Eq. 2.17 and Eq. 2.21, respectively. While the effective FF can be obtained from the measurement of the cross section of the process $e^+e^- \to p\bar{p}$, high statistics and a precise luminosity measurement are essential to extract the proton FFs. As mentioned in Section 2.3.1, results from analysis of the R-scan data (Tab. 3.4, total luminosity 156.94 pb^{-1} at 12 energy points at cms energies 2.232-3.671 GeV) were published in 2015 [42]. Analysis of $e^+e^- \to p\bar{p}$ using the energy-scan data with high luminosity (Tab. 3.4) to extract the proton FFs (electric and magnetic FF separately) is ongoing at the time of writing this thesis.

In this analysis, the ISR process $e^+e^- \to p\bar{p}\gamma$ is studied by using the data collected at the cms energies corresponding to different resonances between 3.773 and 4.6 GeV (Tab. 3.3). It is very difficult to measure the proton FFs through the direct annihilation process with these data. There are two main reasons: first, the cross section of the proton-antiproton production is very low (less than picobarn) at high cms energy; second, the very high background is produced through the strong decays of the resonances (J/ψ or ψ') into the $p\bar{p}$ final state. By the emission of one or more photons in the initial state as discussed in Section 2.3.3, the

invariant mass of the hadronic final state is reduced to values below the e^+e^- cms energy, where the cross section of $e^+e^- \to p\bar{p}$ is larger. This allows for extraction of the proton FFs in a wide q^2 range close to the $p\bar{p}$ threshold through the ISR process from the high-energy data sets.

4.1 Data sets used for $e^+e^- \to p\bar{p}\gamma$ studies

The data sets used for analysis of the ISR process $e^+e^- \to p\bar{p}\gamma$ are listed in Tab. 4.1. The total luminosity is 7.41 fb^{-1} and the data were collected at seven cms energies between 3.773 and 4.600 GeV. Two data sets at the cms energies of the J/ψ and ψ' resonances, listed in Tab. 3.3, are not included in this analysis. It is very difficult to separate the signal of the electromagnetic process $e^+e^- \to p\bar{p}\gamma$ from the very high background of the strong interaction process $e^+e^- \to J/\psi$ (ψ'), with J/ψ (ψ') decaying into the same final state of $p\bar{p}\gamma$. The branching ratios are 3.8×10^{-4} and 3.9×10^{-5} for the $p\bar{p}\gamma$ decay from J/ψ and ψ', respectively. Thus, at the J/ψ and ψ' resonances, the strong decay process is estimated to be around 500 and 30 times larger, respectively, than the signal channel.

Tab. 4.1: Data sets used for the $e^+e^- \to p\bar{p}\gamma$ analysis.

$\sqrt{s}$ (GeV)	Int. Lumi. (pb^{-1})	Run No.	Date	Sample
3.773	2916.94 [76]	[11414, 13988], [14395, 14604], [20448, 23454]	2010, 2011	ψ''
4.009	481.96 [77]	[23463, 24141]	2011	$\psi(4040)$
4.230	1047.34 [77]	[32239, 33484]	2013	Y(4260)
4.260	825.67 [77]	[29677, 30367], [31561, 31981]	2013	
4.360	539.84 [77]	[30616, 31279]	2013	Y(4360)
4.420	1028.89 [77]	[36773, 38140]	2014	$\psi(4420)$
4.600	566.93 [77]	[35227, 36213]	2014	Y(4600)

4.2 Analysis framework – BESIII offline software

The BESIII OFFLINE SOFTWARE SYSTEM (BOSS) [69], based on the C++ language and object-oriented techniques, is used for the data processing and physics analysis. BOSS consists of five functional parts: framework, simulation, reconstruction, calibration and analysis tools.

Three types of event data are defined in the BOSS framework: raw data, reconstructed data and Data-Summary-Tape (DST) data. Both data of the last two types are in ROOT [70] (a modular scientific software framework) format for easy management and usage. The geometry and the material information of the detector can be retrieved from the stored GDML (Geometry Description Markup Language) files, while the magnetic-field service provides the value of the field at any space point within the detector.

Because the data sets were collected at different data-taking periods, data were reconstructed with different BOSS subversions, 6.6.4 (ψ'' - Y(4360)) and 6.6.4.p01 (Y(4420) and Y(4600)).

4.3 Monte Carlo simulation

Signal and background MC simulations are performed to optimize the event-selection criteria, estimate the physics background contamination and calculate the selection efficiencies. The simulation, based on the GEANT4 package [80,81], consists of four parts: event generators, geometrical and material description of the BESIII detector, particle tracking and detector response including digitization models [69, 71, 82].

In the analysis, the event generator PHOKHARA 9.1 [83] is used to generate the process $e^+e^-\to p\bar{p}\gamma$, including radiative corrections of ISR up to Next-to-Leading Order (NLO), Final State Radiation (FSR) and Vacuum Polarization (VP). The selection efficiencies and geometrical acceptances are obtained from MC simulations including all the corrections mentioned above. Radiative corrections are also evaluated using MC simulations, but with radiative effects not included (pure Born process). The built-in model of the proton FFs in the event generator [83] was defined by a fit to the effective FF of the world data in the SL and

TL regions and by a fit to the ratio of proton FFs from BABAR's measurement [47].

For the background evaluation, the inclusive MC samples, which include all the hadronic final states $q\bar{q}$ that can be built with the u, d and s quarks and antiquarks, were generated according to the luminosity of each data set by the BESIII collaboration with the BesEvtGen event generator [84, 85]. The exclusive MC simulation for the dominant background channel, $e^+e^- \to p\bar{p}\pi^0$, is performed with the ConExc model [84] in the BesEvtGen generator.

For each of seven data sets analyzed in this work (Tab. 4.1), MC samples with 10^7 events were produced for the signal channel, $e^+e^- \to p\bar{p}\gamma$. For the dominant background channel, $e^+e^- \to p\bar{p}\pi^0$, two groups of the MC samples were produced: 10^7 events were generated by using the angular distribution based on the available phase space (PHSP); 5×10^4 events were generated by using the angular distribution obtained from the Partial Wave Analysis (PWA) studies [86].

4.4 Tagged and untagged analyses of $e^+e^- \to p\bar{p}\gamma$

As described in Section 3.2, the solid-angle acceptance of the BESIII detector is 93%; particles emitted with a very small or very large polar angle ($|\cos\theta| > 0.93$) cannot be detected. However, as inferred from Eq. 2.27, in most of the ISR events the photon is emitted into the region with the small polar angle with respect to the corresponding beam, therefore the ISR photon escapes from the beam pipe in the forward (positron beam) or backward (electron beam) direction. Figure 4.1 shows the angular distribution of the ISR photons from the $e^+e^- \to p\bar{p}\gamma$ MC simulation at 4.230 GeV. The red shaded regions correspond to the solid-angle acceptance of the EMC subdetector.

Two independent analyses are performed to measure the proton FFs with the same data sets. The tagged (ISR photon) analysis requires all three particles to be detected. The untagged (ISR photon) analysis requires only the two charged particles, proton and antiproton, to be inside the detector acceptance and without a high-energetic neutral shower simultaneously in the EMC subdetector. Table 4.2 summarizes the geometrical acceptance for both analyses. Depending on the cms energy of e^+e^-, around 11-12% of the signal events land in the detector acceptance for the tagged analysis, while the acceptance of the detector for the signal

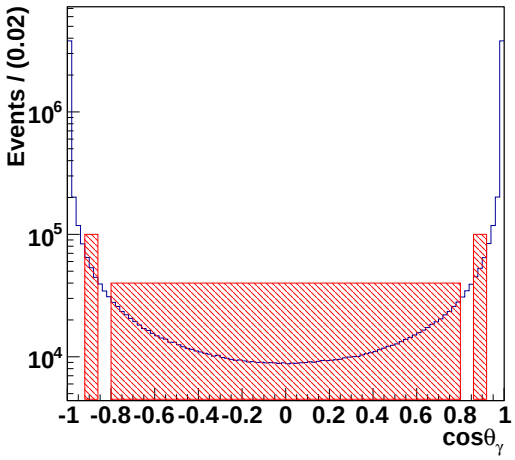

Fig. 4.1: The angular distribution of the ISR photon from the $e^+e^- \to p\bar{p}\gamma$ MC simulation at 4.230 GeV.

events of the untagged analysis is around 31-46%. Therefore the starting statistics of the untagged analysis are around three times higher than those of the tagged analysis, which is a big advantage. The tagged analysis has two important advantages. First, it provides a flat angular detection efficiency for the full angular distribution of the proton, which allows for the ratio of proton FFs extracted with a high precision. Second, it is the only way to access the threshold of $p\bar{p}$ production in the experiment of e^+e^- collision.

The $e^+e^- \to p\bar{p}\gamma$ analysis with the ISR photon tagged is presented in detail in this thesis. The results from the analysis with the ISR photon untagged are reported in Chapter 10.

Tab. 4.2: Geometrical acceptance (%) of the BESIII detector for $e^+e^- \to p\bar{p}\gamma$ events.

$\sqrt{s}$ [GeV]	$p\bar{p}$ pair in MDC (%)	ISR photon	
		tagged (%)	untagged (%)
3.773	58.55	12.27	46.28
4.009	53.41	11.84	41.57
4.230	48.93	11.53	37.40
4.260	48.33	11.49	36.84
4.360	46.40	11.34	35.06
4.420	45.27	11.27	34.00
4.600	42.06	11.07	30.99

CHAPTER 5

Analysis of $e^+e^- \to p\bar{p}\gamma$ with ISR Photon Tagged

This chapter describes the selection of events from the ISR process $e^+e^- \to p\bar{p}\gamma$ with the ISR photon tagged. All three particles, proton, antiproton and ISR photon, are detected in the BESIII detector. To illustrate the strategy of the whole analysis, figures from the data set at 4.230 GeV are shown. Without as special notice, the plots shown are from the events passing the full selection criteria presented in this chapter.

5.1 Event selection

In the final state, a proton-antiproton pair and a high-energy photon are required in the spectrometer acceptance region. Information from all the subdetectors is used: the momentum and dE/dx of charged particles from the MDC, the time information from the TOF, the energy-deposition information from the EMC and the hits information from the MUC.

5.1.1 Selection criteria for three particles

The criteria to select the three particles of a signal event can be divided in two kinds: the criteria applied to the charged tracks (charged-track selection and particle identification), and

the criteria applied to the neutral showers (neutral-shower selection). The goal of these criteria is to identify the events with a proton-antiproton pair and at least one high-energetic ISR photon.

- Charged-track selection
  - A vertex requirement ensures that the charged tracks of the event originate from the interaction point of the two beams. R_{xy} and R_z are defined as the closest distance of approach between the interaction point and the reconstructed track in the xy-frame and in the z-direction, respectively. Values of $|R_{xy}|$ <1 cm and $|R_z| < 10$ cm are required for each good charged-track candidate. Figure 5.1 shows the reconstructed vertex distribution from the MC simulation, for which no selection creteria have yet been applied.

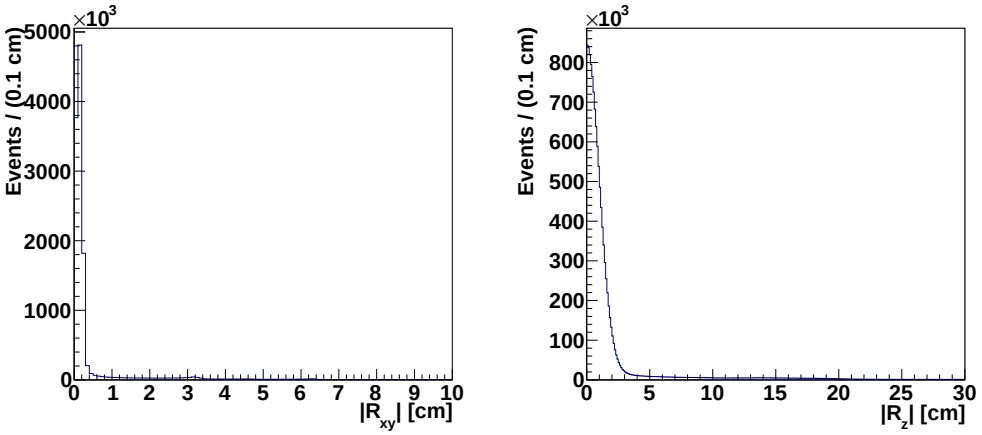

(a) xy-plane (b) z-direction

Fig. 5.1: The vertex distribution of reconstructed tracks in (a) the xy-plane, and (b) the z-direction from the MC simulation. No selection criteria have yet been applied.

  - To improve the momentum resolution, the track has to pass the track-fitting algorithm by using the Kalman filter method [87].
  - Each good track candidate must be within the geometrical acceptance of the MDC: $|\cos\theta| < 0.93$, with the polar angle (θ) of the track defined with respect to the horizontal direction of the positron beam (z-axis). Figure 5.2 shows the angular

distribution of reconstructed tracks from the MC simulation. No selection criteria have yet been applied.

Only events with exactly two oppositely charged tracks with fulfilling the above requirements are accepted for further selection.

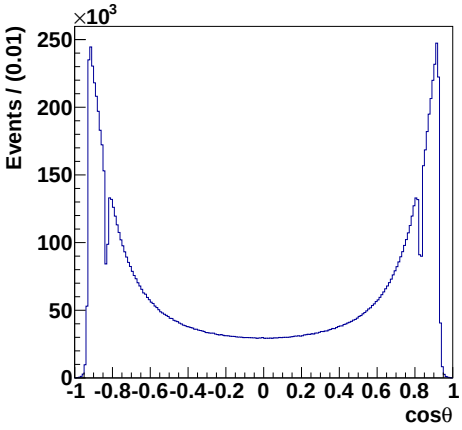

Fig. 5.2: The angular distribution of reconstructed tracks from the MC simulation. No selection criteria have yet been applied.

- Particle Identification (PID)
  - The particle identification mainly uses the information from the MDC about the dE/dx and the momentum of the tracks, the time-of-flight provided by the TOF and the information provided by the EMC and MUC subdetectors concerning the energy deposition and the number of hits, respectively. The probability of each charged track, $\mathrm{Prob}(i=\pi,K,p,\mu,e)$, for the hypothesis that the track is a pion, kaon, proton, muon or electron is calculated using the information from the subdetectors. For the proton or antiproton candidate, it is required that:

$$\mathrm{Prob}(p) > Prob(i),\ i = \pi,\ K,\ \mu \text{ or } e, \tag{5.1}$$

or, equivalently:

$$\log\left[\frac{\mathrm{Prob}(p)}{\mathrm{Prob}(i)}\right] > 0,\ i = \pi,\ K,\ \mu \text{ or } e. \tag{5.2}$$

- For the proton candidate, if the track can reach the EMC, the ratio (E/p) of the energy (E) deposited in the EMC to the momentum (p) measured in the MDC is required to be less than 0.5. This requirement suppresses BhaBha background events, in which the ratio E/p of the electron or positron is centered at 1.0. Figure 5.3 shows the E/p distribution of both the positive (proton) and negative (antiproton) charged tracks from the MC simulation. Due to possible annihilation of the antiproton in the EMC, the E/p can be larger than 1.0.

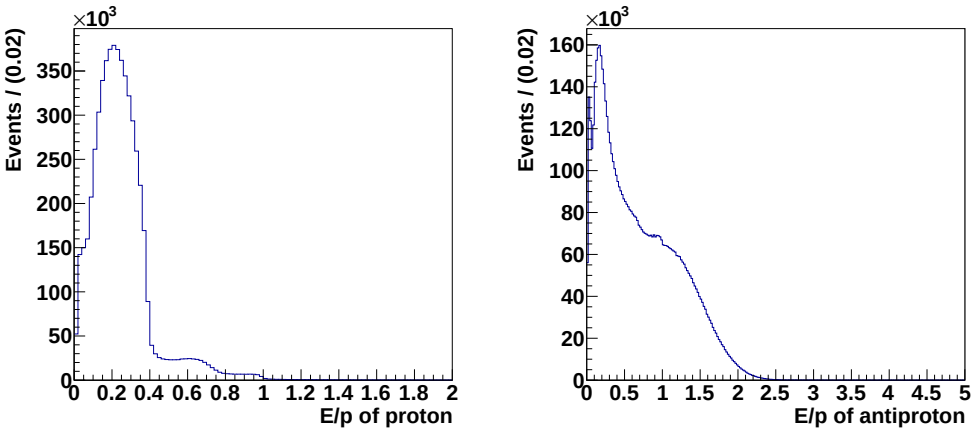

(a) Proton (b) Antiproton

Fig. 5.3: The reconstructed E/p distribution of the energy deposited in the EMC over the momentum measured in the MDC, from the MC simulation for (a) the proton and (b) antiproton. No selection criteria have yet been applied.

- Neutral-shower selection

  - To avoid electronic noise, requirements on the energy and the polar angle are applied to the neutral showers in the EMC.

$$\begin{cases} \text{EMC barrel} : E_{\text{shower}} > 25 \text{ MeV}, \ |\cos\theta| < 0.80, \\ \text{EMC endcaps} : E_{\text{shower}} > 50 \text{ MeV}, \ 0.86 < |\cos\theta| < 0.92 \end{cases} \tag{5.3}$$

  The neutral showers are also required to have no information in the MDC.

Events with at least one good shower fulfilling the requirements above are accepted for the further selection.

5.1.2 Selection criteria for signal events

Based on the previous selections for the three particles, the following selection criteria are applied to identify the signal process $e^+e^- \to p\bar{p}\gamma$, by considering the kinematic features of the initial (e^+e^-) and final ($p\bar{p}\gamma$) states.

- ISR photon: the most energetic neutral shower with energy larger than 0.4 GeV is assigned as the ISR photon.

- Four-constraint (4C) kinematic fit: information about the two charged tracks and the assigned ISR photon is combined to perform a kinematic fit, with the initial four-momenta of the e^+e^--beams as constraint. Figure 5.4 shows the χ^2_{4C} distribution of the 4C kinematic fit from the data (red points with error bars) and MC simulation (blue histogram), respectively.

- A tight cut of $\chi^2_{4C} \leq 50$ is applied to the χ^2_{4C} distribution for the study of the proton FFs, as discussed in Chapter 8.

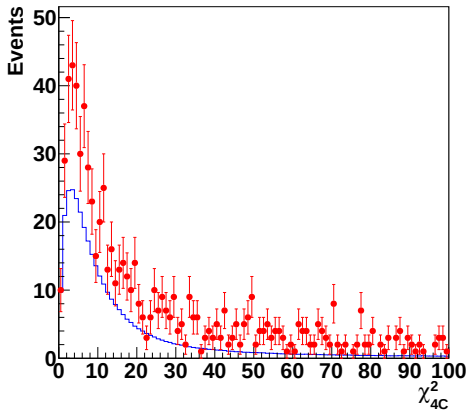

Fig. 5.4: The χ^2_{4C} distribution of the 4C kinematic fit for data (red points) and MC simulation (blue histogram).

- $p\bar{p}\pi^0(\eta)$ event veto: if the event surviving the 4C kinematic fit has more than one photon (including the high-energy photon) detected, a five-constraint (5C) kinematic fit is applied. Any two photons are combined to a potential π^0 (η) by looping over all available photons and the two photons are constrained to be a π^0 (0.135 GeV, or η (0.548 GeV)). The event is discarded if χ^2_{5C} <25, where the combination with the smallest χ^2_{5C}, if more than one meets this selection criterion, is chosen.

After the event selection above, all $p\bar{p}\gamma$-like events are selected and background is not completely removed. Figure 5.5 shows the ISR photon energy and $p\bar{p}$ invariant-mass distributions. The red points with error bars represent the distributions from data, and the blue histogram represents the distributions normalized by the luminosity and cross section of $e^+e^-\to p\bar{p}\gamma$ from the MC simulation. In the photon energy spectrum (Fig. 5.5(a)), the peak at 0.9 GeV in the data corresponds to the ISR photon from $e^+e^-\to J/\psi\gamma$, while in the $p\bar{p}$ invariant-mass spectrum (Fig. 5.5(b)), the sharp peak from data corresponds to the decay of $J/\psi\to p\bar{p}$. Furthermore, the differences between the data and MC simulation in the distributions, shown in Fig. 5.4 and Fig. 5.5, are due to the $p\bar{p}\pi^0$ background not being completely removed from data.

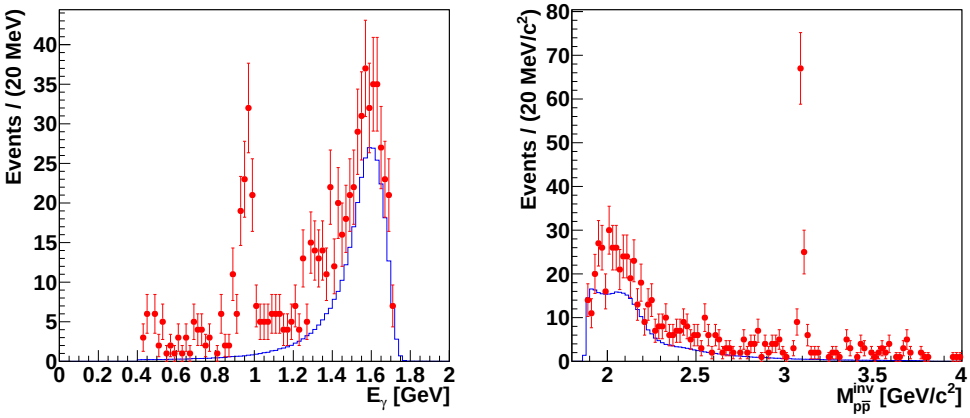

(a) Photon energy (b) $p\bar{p}$ invariant mass

Fig. 5.5: Distributions of (a) the photon energy and (b) the $p\bar{p}$ invariant mass from the data (red points with error bars) and MC simulation (blue histogram).

5.2 Data quality: study of $J/\psi \to p\bar{p}$ from $e^+e^-\to J/\psi\gamma$

As mentioned above, it is possible to access the narrow resonance J/ψ with J/ψ decaying into $p\bar{p}$ through the $e^+e^-\to p\bar{p}\gamma$ study. The branching ratio of $J/\psi \to p\bar{p}$ is determined by

$$\mathrm{Br}_{J/\psi\to p\bar{p}} = \frac{N^{\mathrm{fit}}_{J/\psi}}{\mathcal{L}_{\mathrm{int}} \times \sigma_{J/\psi\gamma} \times \epsilon_{\mathrm{MC}}}, \tag{5.4}$$

where $N^{\mathrm{fit}}_{J/\psi}$ is the number of $J/\psi \to p\bar{p}$ events given by a fit (see Eq. 5.6), $\mathcal{L}_{\mathrm{int}}$ is the integrated luminosity of the data, ϵ_{MC} is the MC efficiency which is taken from the corresponding $p\bar{p}$ invariant-mass region of the $e^+e^-\to p\bar{p}\gamma$ MC simulations, and $\sigma_{J/\psi\gamma}$ is the cross section of $e^+e^-\to J/\psi\gamma$ which reads as:

$$\frac{d\sigma_{e^+e^-\to J/\psi\gamma}}{ds'} = \frac{1}{s}W(s,x)\frac{12\pi\Gamma_{ee}\times\Gamma_{\mathrm{tot}}}{(s'-M^2_{J/\psi})^2 + M^2_{J/\psi}\Gamma^2_{\mathrm{tot}}}. \tag{5.5}$$

In the previous equation, $M_{J/\psi}$ (3096.900 MeV) and Γ_{tot} (92.9 keV) are the mass and full width of J/ψ, respectively, Γ_{ee} (5.55 keV) is the electronic width of J/ψ from PDG [4], and $W(s,x)$ is the radiator function (Eq. 2.27). Figure 5.6 shows the full $p\bar{p}$ invariant-mass spectrum (a) from the threshold to 4.0 GeV/c^2, and an unbinned fit result of $J/\psi \to p\bar{p}$ (b) for the data set at 4.230 GeV. In the fit, the data are described by a function consisting of two parts: a Breit-Wigner convoluted with a Gaussian to account for the resonance and a one-degree polynomial function to account for the continuum contribution. The fit function reads as,

$$\frac{dN}{dM_{p\bar{p}}} = N^{\mathrm{fit}}_{J/\psi} \times \frac{1}{(M_{p\bar{p}} - M_{J/\psi})^2 + \Gamma^2_{\mathrm{tot}}/4} \times e^{-\frac{1}{2}(\frac{M_{p\bar{p}}}{\Sigma})^2} + N^{\mathrm{fit}}_{\mathrm{con}} \times (1 + p_0 \times M_{p\bar{p}}), \tag{5.6}$$

where $N^{\mathrm{fit}}_{\mathrm{con}}$ is the number of events from the continuum contribution, and the parameter Σ is the $p\bar{p}$ invariant-mass resolution determined by the proton- and antiproton-momentum resolutions. The J/ψ mass ($M_{J/\psi}$) and the polynomial constant (p_0) can be obtained from the fit.

The unbinned fit results from the rest of the data sets at other cms energies are shown in

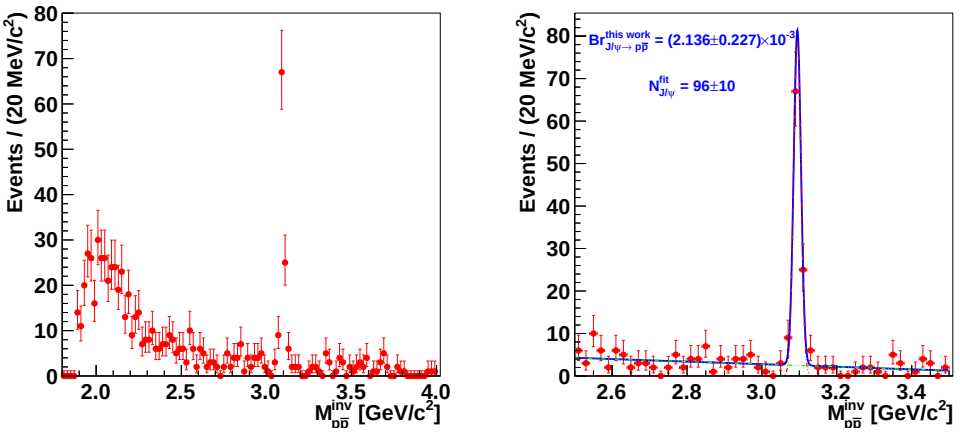

(a) $p\bar{p}$ invariant mass (b) J/ψ resonance fit

Fig. 5.6: The $p\bar{p}$ invariant mass (red points with error bars) from the data set at 4.230 GeV: (a) full spectrum; (b) unbinned fit (blue solid line) of the $J/\psi \to p\bar{p}$ data to a Breit-Wigner convoluted with a Gaussian function (red dash-dotted line) for the resonance, and a one-degree polynomial function (green dash-dotted line) for the continuum contribution.

Fig. 5.7. The red dash-dotted line represents the J/ψ resonance and the green dash-dotted line represents the continuum contribution.

An unbinned fit is performed on the $J/\psi \to p\bar{p}$ data from the combined data sets (Fig. 5.8(a)) to the fit function Eq. 5.6 and the branching ratio is calculated according to

$$\mathrm{Br}_{J/\psi\to p\bar{p}} = \frac{N^{\mathrm{fit}}_{J/\psi}}{(\sum_{i=1}^{7} \mathcal{L}^i_{\mathrm{int}} \times \sigma^i_{J/\psi\gamma}) \times \frac{\sum_{i=1}^{7} \mathcal{L}^i_{\mathrm{int}} \times \epsilon^i_{\mathrm{MC}}}{\sum_{i=1}^{7} \mathcal{L}^i_{\mathrm{int}}}}, \tag{5.7}$$

where the index i runs over all seven data sets and a weighted average MC efficiency is used by taking into account the luminosity of each data set.

Table 5.1 summarzies the fit results from all data sets with statistical errors included. Figure 5.8 (b) shows the results for the branching ratio of $J/\psi \to p\bar{p}$ from the different data sets and from their sum, together with the value from the PDG [4]. The data set at 4.360 GeV shows a two-sigma deviation with respect to the PDG value, while the result from the combined data sets shows good agreement with the world data.

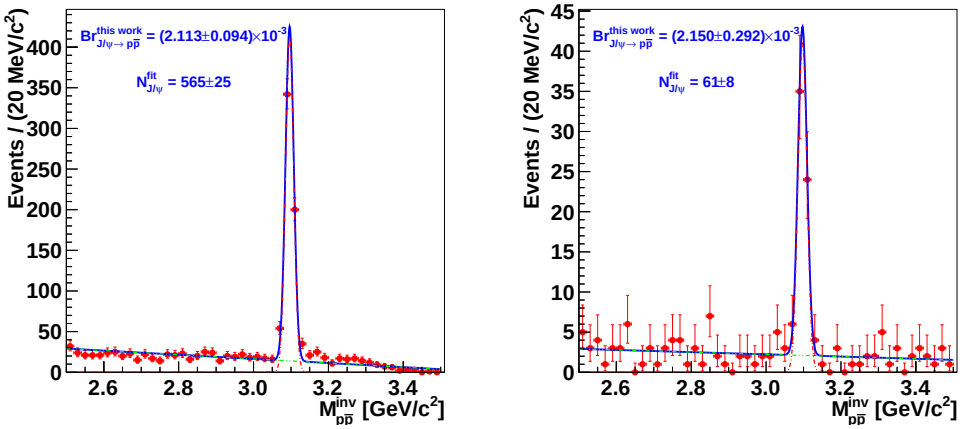

(a) 3.773 GeV

(b) 4.009 GeV

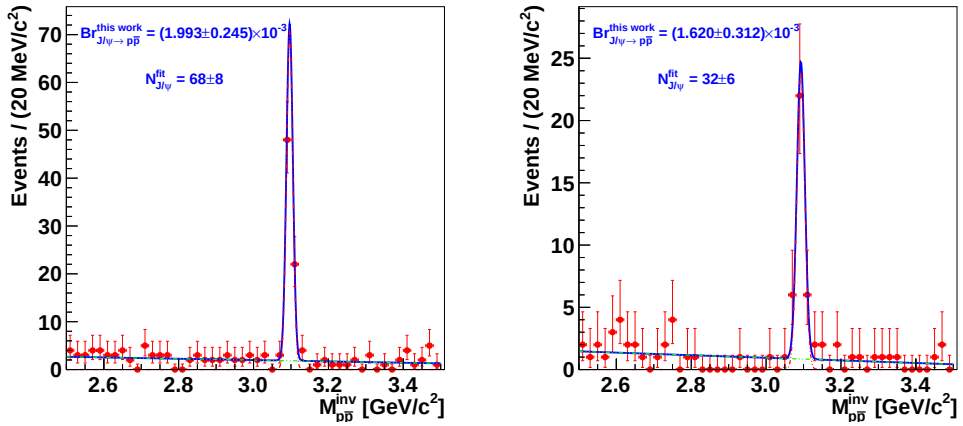

(c) 4.260 GeV

(d) 4.360 GeV

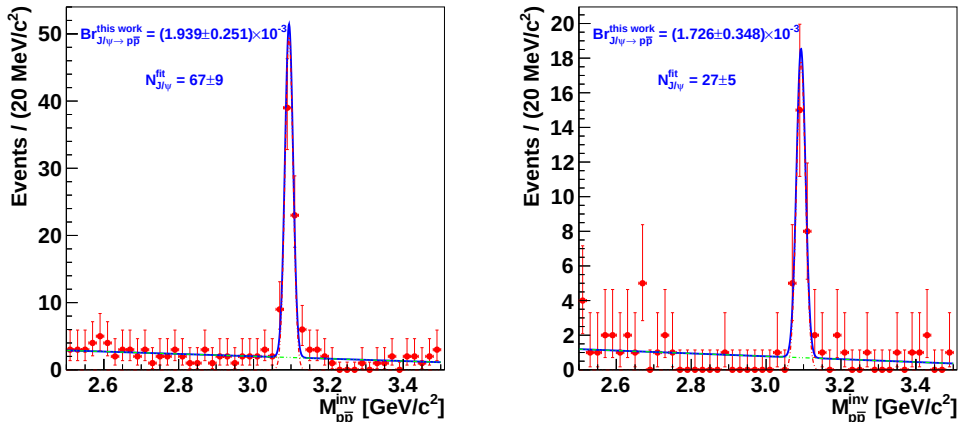

(e) 4.420 GeV

(f) 4.600 GeV

Fig. 5.7: Unbinned fit (blue solid line) of the $J/\psi \to p\bar{p}$ data to a Breit-Wigner convoluted with a Gaussian function (red dash-dotted line) for resonance, and a one-degree polynomial function (green dash-dotted line) for the continuum contribution.

Tab. 5.1: The branching ratio of J/ψ decaying to $p\bar{p}$, from the analysis of $e^+e^- \to p\bar{p}\gamma$ with the ISR photon tagged.

E_{cms} (GeV)	$\mathcal{L}_{\mathrm{int}}$ (pb^{-1})	σ (pb)	ϵ_{MC} (%)	$\mathcal{N}^{\mathrm{fit}}_{J/\psi}$	$\mathrm{Br}_{J/\psi\to p\bar{p}}$ ($\times 10^{-3}$)	$\mathrm{Br}^{\mathrm{PDG2016}}_{J/\psi\to p\bar{p}}$ ($\times 10^{-3}$) [4]
3.773	2916.94	991.73	9.25	565±25	2.11±0.09	2.120±0.029
4.009	481.96	679.14	8.73	61±8	2.15±0.29	
4.230	1047.34	512.22	8.41	96±10	2.14±0.23	
4.260	825.67	494.83	8.39	68±8	1.99±0.25	
4.360	539.84	443.80	8.22	32±6	1.62±0.31	
4.420	1028.89	417.49	8.09	67±9	1.94±0.25	
4.600	566.93	352.08	7.82	27±5	1.73±0.35	
combined			8.65	915±32	2.10±0.07	

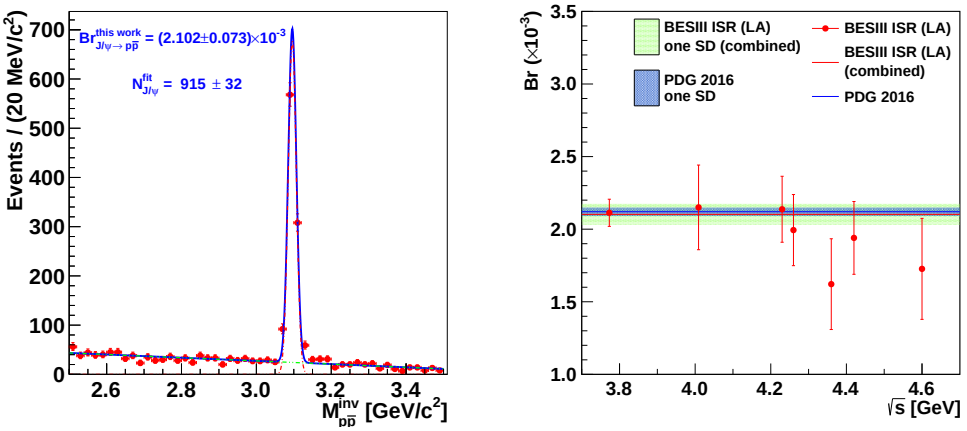

(a) J/ψ fit (combined) (b) branching ratio

Fig. 5.8: Unbinned fit of the $J/\psi \to p\bar{p}$ data and the branching ratio of $J/\psi \to p\bar{p}$ from the process $e^+e^- \to p\bar{p}\gamma$: (a) unbinned fit of J/ψ from the combined data sets, (b) results for the branching ratio of $J/\psi \to p\bar{p}$ obtained from the different data sets and from their sum, together with the PDG value from 2016 [4]. The green and blue areas represent one standard deviation (SD) of the result from the combined data sets and the PDG value, respectively.

CHAPTER 6

Background Evaluation

As mentioned in Sections 4.3 and 5.1.2, there is still some background contamination in the selected events after the $e^+e^- \to p\bar{p}\gamma$ selection criteria have been applied. The composition of the remaining background is studied by analyzing the inclusive ($q\bar{q}$) MC samples generated by the BESIII collaboration. These samples contain the expected number of $q\bar{q}$ events (Section 4.3) according to the luminosity at each energy point and are used to determine the topology of the events surviving the $e^+e^- \to p\bar{p}\gamma$ selection criteria. Table 6.1 shows the $q\bar{q}$ events surviving the signal selection criteria. Only the signal $p\bar{p}\gamma$ and some background $p\bar{p}\pi^0$ with $\pi^0 \to \gamma\gamma$ pass all selection requirements. Other ISR charged-pair channels like $\pi^+\pi^-\gamma$, $K^+K^-\gamma$ and $\mu^+\mu^-\gamma$, and the channel $p\bar{p}\eta$ ($\eta \to \gamma\gamma$), are highly suppressed by the signal selection criteria. The contamination from such background channels is negligible.

Tab. 6.1: Topology of the inclusive MC simulation at 4.230 GeV after the signal $e^+e^- \to p\bar{p}\gamma$ selection.

Generated	Surviving Events		
$q\bar{q}$ events	$p\bar{p}\gamma$	$p\bar{p}\pi^0$	Other channels
2×10^7	4226	164	3

6.1 Method to determine contamination from $e^+e^-\to p\bar{p}\pi^0$ background

To estimate the background contamination, $e^+e^-\to p\bar{p}\pi^0$ MC samples are generated by using the BesEvtGen event generator with the ConExc model [84, 85] based on the PHSP angular distribution (Section 4.3). The real angular distribution of the $p\bar{p}\pi^0$ events is obtained from the analysis of $e^+e^-\to p\bar{p}\pi^0$ data (Section 6.2). The background contamination, $H^{\rm bkg}_{\rm isr}$, is calculated as follows:

$$H^{\rm bkg}_{\rm isr} = H^{\rm dat}_{\pi^0} \times \frac{H^{\rm MC}_{\rm isr}}{H^{\rm MC}_{\pi^0}}, \tag{6.1}$$

where $H^{\rm dat}_{\pi^0}$ is the distribution of the data surviving the $p\bar{p}\pi^0$ selection criteria, and $H^{\rm MC}_{\rm isr}$ and $H^{\rm MC}_{\pi^0}$ are the distributions obtained after the analysis of the $p\bar{p}\pi^0$ MC sample using $p\bar{p}\gamma$ and $p\bar{p}\pi^0$ analyses, respectively.

6.2 Analysis strategy of $e^+e^-\to p\bar{p}\pi^0$ events

For the $e^+e^-\to p\bar{p}\pi^0$ analysis, the selection of good charged tracks and good showers is the same as in the $e^+e^-\to p\bar{p}\gamma$ single-particle selection (Section 5.1.1), but requires at least two good neutral showers instead of one. A 5C kinematic fit is performed for the two oppositely charged tracks and the two showers. If the number of good showers is larger than two, the combination of two good showers giving the minimum χ^2_{5C} is accepted as a $p\bar{p}\pi^0$ candidate. A $\chi^2_{5C}\leq$60 is required. To veto $e^+e^-\to p\bar{p}\gamma$ events, which are background for the $e^+e^-\to p\bar{p}\pi^0$ event selection, a 4C kinematic fit is performed with the highest energetic shower as the ISR photon. It is required that $\chi^2_{4c}\geq$25. To find out if there is remaining $p\bar{p}\gamma$ backgound in the $e^+e^-\to p\bar{p}\pi^0$ data, the $p\bar{p}\gamma$ MC sample at 4.230 GeV is analyzed using the $e^+e^-\to p\bar{p}\pi^0$ selection criteria. The result shows that the $p\bar{p}\gamma$ contamination is less than 1/1000, which is negligible for this study.

Figure 6.1 and Fig. 6.2 show the $p\bar{p}$ invariant-mass spectrum and the proton angular distribution for the mass interval th.–1.950 GeV/c^2. The angle distribution shown here is the

helicity distribution of the proton, as explained in Section 2.3.3. In these figures, (a), (b), (c) and (d) correspond to $H_{\mathrm{isr}}^{\mathrm{MC}}$, $H_{\pi^0}^{\mathrm{MC}}$, $H_{\pi^0}^{\mathrm{dat}}$ and background contamination distributions from Eq. 6.1. Figure 6.3 shows the proton angular distributions of the estimated $p\bar{p}\pi^0$ background together with the $p\bar{p}\gamma$ signal for different invariant-mass intervals.

As a cross-check, small MC samples (5×10^4), generated according to the angular distribution from the partial-wave-analysis (PWA) studies, are analyzed with the $p\bar{p}\gamma$ event selection. The results are normalized by a factor according to the $e^+e^-\to p\bar{p}\pi^0$ cross section* and the integrated luminosity of the corresponding data set.

Figure 6.4 shows a comparison of the proton angular distribution of the expected $p\bar{p}\pi^0$ background using the two different methods presented in this section. The results show good agreement for both the proton angular distribution and the absolute number of the statistics from the two methods to estimate the $p\bar{p}\pi^0$ background contamination.

*Unpublished results by X.C. Ai and J. Liu from BESIII

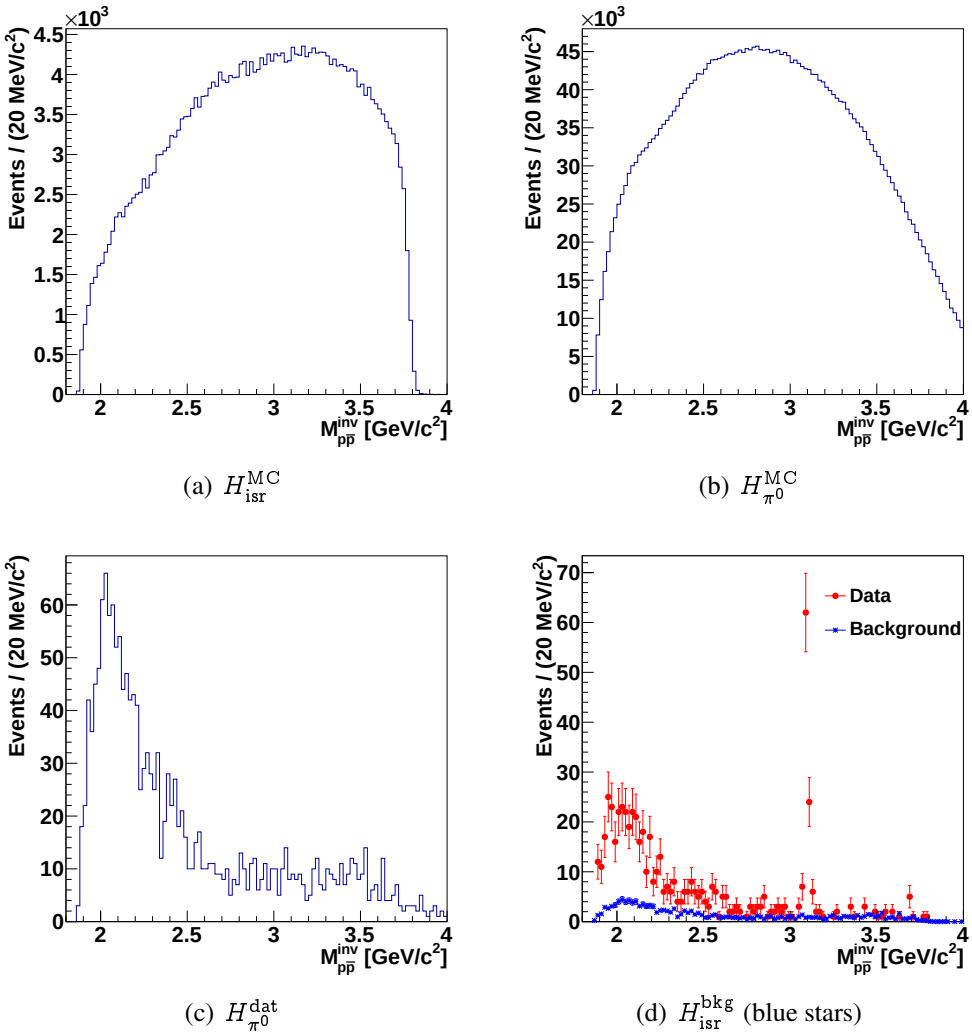

(a) $H^{\rm MC}_{\rm isr}$ (b) $H^{\rm MC}_{\pi^0}$

(c) $H^{\rm dat}_{\pi^0}$ (d) $H^{\rm bkg}_{\rm isr}$ (blue stars)

Fig. 6.1: The distributions of the $p\bar{p}$ invariant-mass spectrum from the MC simulation of $e^+e^-\to p\bar{p}\pi^0$ and the data set at 4.230 GeV after different event selections: (a) $p\bar{p}\pi^0$ MC simulation after $p\bar{p}\gamma$ event selection, (b) $p\bar{p}\pi^0$ MC simulation after $p\bar{p}\pi^0$ event selection, (c) data after $p\bar{p}\pi^0$ event selection, (d) blue stars represent the estimated $p\bar{p}\pi^0$ background distribution as a function of the $p\bar{p}$ invariant mass, red points represent the $p\bar{p}$ invariant-mass distribution from the signal $e^+e^-\to p\bar{p}\gamma$ events collected from data.

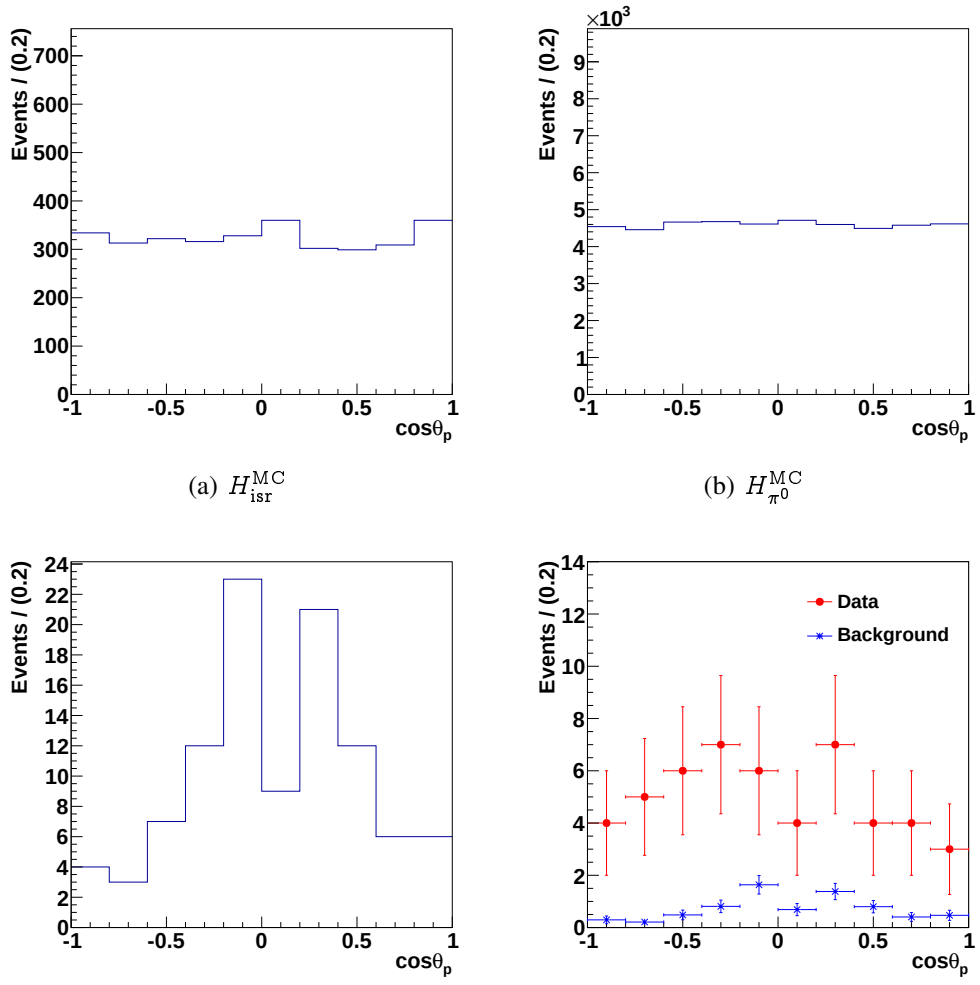

(a) $H_{\mathrm{isr}}^{\mathrm{MC}}$ (b) $H_{\pi^0}^{\mathrm{MC}}$

(c) $H_{\pi^0}^{\mathrm{dat}}$ (d) $H_{\mathrm{isr}}^{\mathrm{bkg}}$ (blue stars)

Fig. 6.2: The proton angular distribution for the mass interval th.–1.950 GeV/c^2 from the MC simulation of $e^+e^-\to p\bar{p}\pi^0$ and the data set at 4.230 GeV after different event selections: (a) $p\bar{p}\pi^0$ MC simulation after $p\bar{p}\gamma$ event selection, (b) $p\bar{p}\pi^0$ MC simulation after $p\bar{p}\pi^0$ event selection, (c) data after $p\bar{p}\pi^0$ event selection, (d) blue stars represent the estimated $p\bar{p}\pi^0$ background distribution as a function of the proton angle, red points represent the proton angular distribution from the signal $e^+e^-\to p\bar{p}\gamma$ events collected from data.

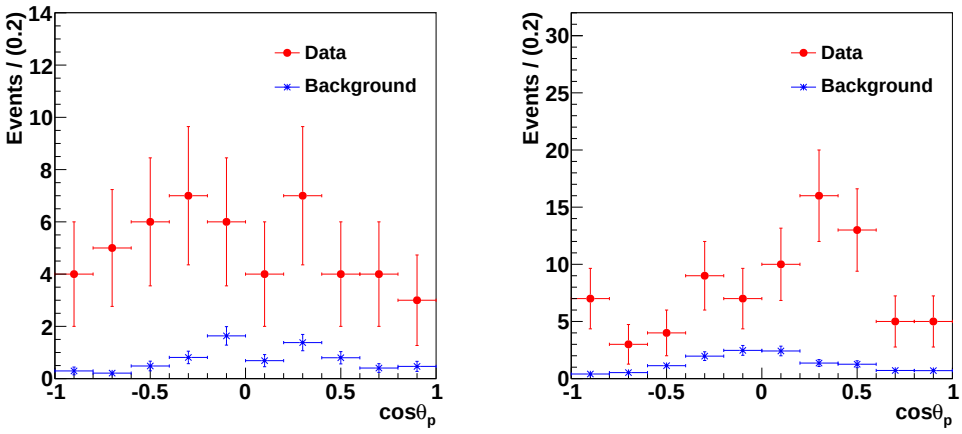

(a) th.–1.950 GeV/c^2

(b) 1.950–2.025 GeV/c^2

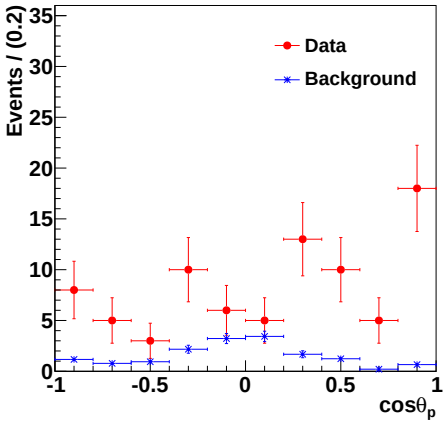

(c) 2.025–2.100 GeV/c^2

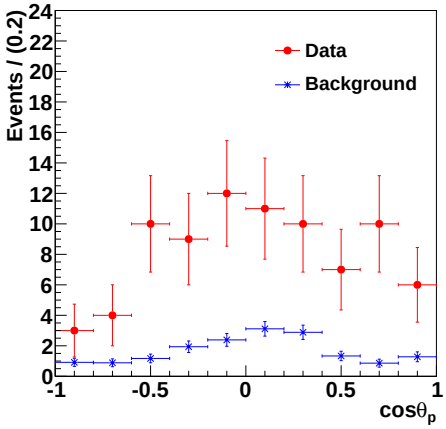

(d) 2.100–2.200 GeV/c^2

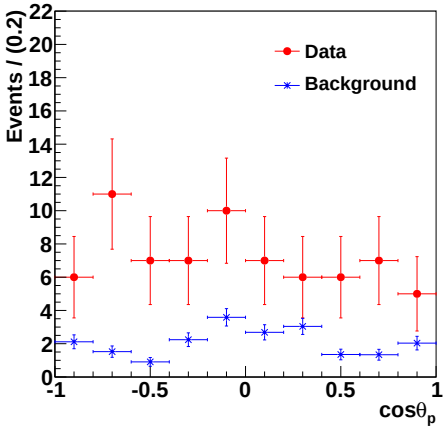

(e) 2.200–2.400 GeV/c^2

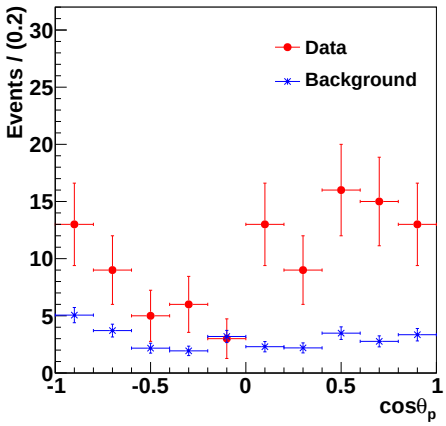

(f) 2.400–3.000 GeV/c^2

Fig. 6.3: The proton angular distribution of the selected $p\bar{p}\gamma$ data (red points) and the estimated background (blue stars) for different $p\bar{p}$ invariant-mass intervals at $\sqrt{s}$=4.230 GeV.

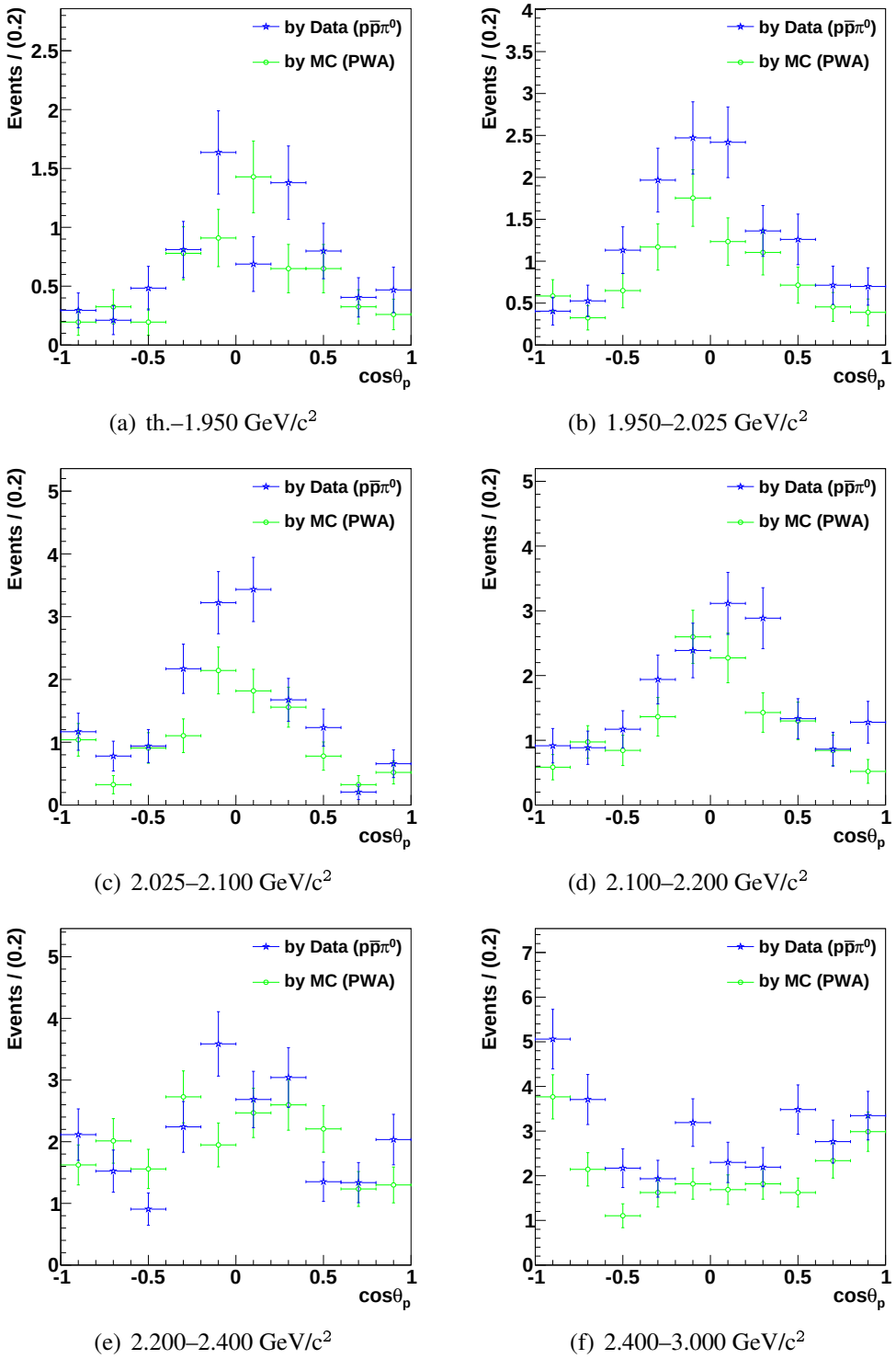

(a) th.–1.950 GeV/c^2

(b) 1.950–2.025 GeV/c^2

(c) 2.025–2.100 GeV/c^2

(d) 2.100–2.200 GeV/c^2

(e) 2.200–2.400 GeV/c^2

(f) 2.400–3.000 GeV/c^2

Fig. 6.4: Comparison of the estimated background from the methods of the $p\bar{p}\pi^0$ data analysis (blue stars) and the MC PWA simulations (green circles).

CHAPTER 7

Understanding of Data: Comparison between Data and MC Simulation

After the full event selection of the signal $e^+e^- \to p\bar{p}\gamma$, and the evaluation of the remaining background $e^+e^- \to p\bar{p}\pi^0$, a comparison is performed between the data and the MC signal simulation for the distributions of χ^2_{4C}, the $p\bar{p}$ invariant mass and the proton angle.

Figure. 7.1 shows the $p\bar{p}$ invariant-mass distribution (a) and the χ^2_{4C} distributon (b) of data, and the expected signal and background contributions. Figure 7.2 shows the proton angular distributions for different $p\bar{p}$ invariant-mass intervals. The red points with error bars represent the combined data of all seven data sets, the blue histogram represents the signal and background contributions, and the green shaded area represents the estimated background. The signal MC simulation is normalized according to the luminosity and cross section of $e^+e^- \to p\bar{p}\gamma$ from the event generator, PHOKHARA 9.1 [83]. All the signal MC simulations at different cms energies are combined after the normalization. The total background is a sum of the estimated background from each data set. In the χ^2_{4C} distribution, the background distribution is a normalized distribution from the MC simulation (PHSP) of $e^+e^- \to p\bar{p}\pi^0$, selected as $p\bar{p}\gamma$ events according to the luminosity and cross section of the $p\bar{p}\pi^0$ production. In the low χ^2_{4C} range, differences can be observed between the data and the mixture of

signal and background MC simulations. The reason is that the data contains the process $e^+e^- \to J/\psi\gamma$ with $J/\psi \to p\bar{p}$ (narrow peak in the $p\bar{p}$ invariant-mass distribution shown in Fig. 7.1), while the mixture of signal and background MC simulations does not include this process.

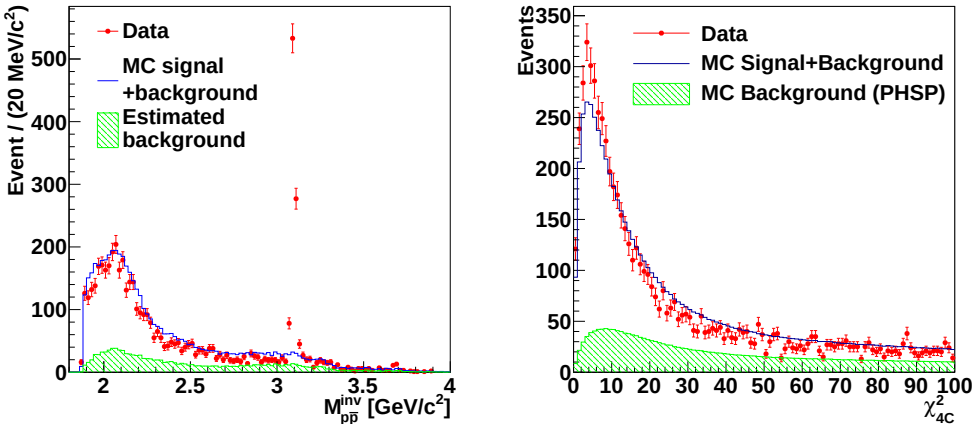

(a) $p\bar{p}$ invariant mass (b) χ^2_{4C}

Fig. 7.1: Comparison of the combined data sets (red points with error bars), the signal and background contributions (blue histogram), and the estimated background (green-shaded area): (a) $p\bar{p}$ invariant mass, (b) χ^2_{4C} of the 4C kinematic fit.

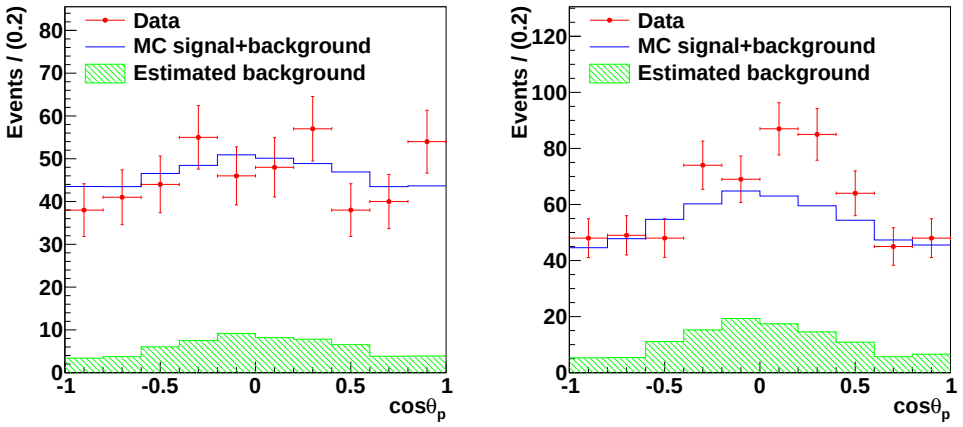

(a) th. – 1.950 GeV/c^2 (b) 1.950 – 2.025 GeV/c^2

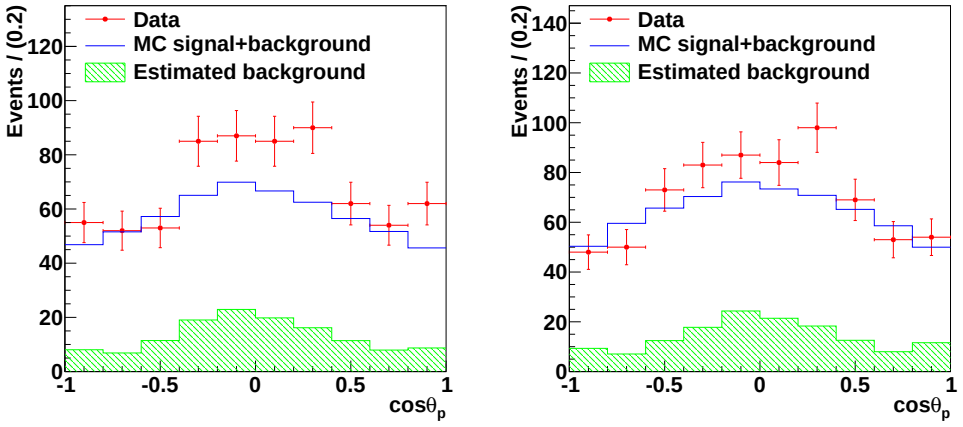

(c) 2.025 – 2.100 GeV/c^2 (d) 2.100 – 2.200 GeV/c^2

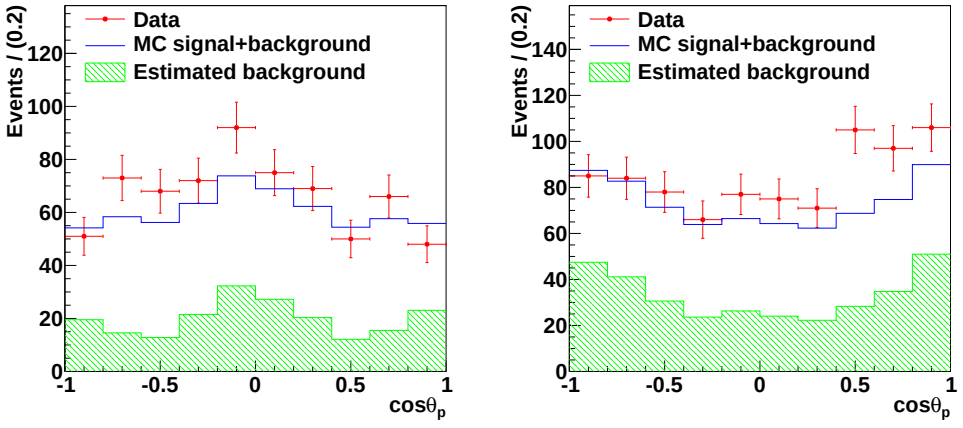

(e) 2.200 – 2.400 GeV/c^2 (f) 2.200 – 3.000 GeV/c^2

Fig. 7.2: The proton angular distribution for different mass intervals, from the combined data sets (red points with error bars), the signal and background contributions (blue histogram), and the estimated background (green-shaded area).

CHAPTER 8

Extraction of Observables

The clean signal events, $e^+e^- \to p\bar{p}\gamma$, are obtained by subtracting the estimated background for each data set separately. The ratio (modulus) of the proton FFs, the cross section of $e^+e^- \to p\bar{p}$ and the effective FF of the proton are studied based on these clean signal events.

8.1 Ratio of proton form factors

The ratio of proton electric and magnetic form factors can be extracted from a fit to the proton angular distribution (θ_p):

$$\frac{dN}{d\cos\theta_p} = \mathcal{A}\Big[H_M(\cos\theta_p, M_{p\bar{p}}) + \frac{R_{em}^2}{<\tau>} H_E(\cos\theta_p, M_{p\bar{p}})\Big], \tag{8.1}$$

where $\mathcal{A}$ is a global parameter, $R_{em} = \frac{|G_E|}{|G_M|}$ is the ratio of proton FFs and $<\tau> = \frac{q^2}{4m_p^2}$. The momentum transfer squared q^2 is the mean value of the square of the $p\bar{p}$ invariant mass calculated according to the distribution in an invariant-mass interval. The functions $H_M(\cos\theta_p, M_{p\bar{p}})$ and $H_E(\cos\theta_p, M_{p\bar{p}})$ do not have analytic forms for the ISR process $e^+e^- \to p\bar{p}\gamma$ and must be determined from the MC simulations.

Two MC simulations of $e^+e^- \to p\bar{p}\gamma$ are performed at $\sqrt{s} = 4.230$ GeV with G_E=0

and G_M=0 to produce the terms of $H_M(\cos\theta_p, M_{p\bar{p}})$ and $H_E(\cos\theta_p, M_{p\bar{p}})$, respectively. Both simulations include the full radiative corrections ISR-NLO, FSR and VP. A comparison of $H_M(\cos\theta_p, M_{p\bar{p}})$ and $H_E(\cos\theta_p, M_{p\bar{p}})$ with the terms $(1+\cos^2\theta_p)$ and $(1-\cos^2\theta_p)$ of Eq. 2.17 shows that they behave similarly. Figure 8.1 shows the comparison of $H_M(\cos\theta_p, M_{p\bar{p}})$ and $H_E(\cos\theta_p, M_{p\bar{p}})$ to the functions $(1+\cos^2\theta_p)$ and $(1-\cos^2\theta_p)$, respectively, for the mass interval corresponding to th.–1.950 GeV/c^2. For a 10-bin distribution, the maximum difference between $H_M(\cos\theta_p, M_{p\bar{p}})$ and $(1+\cos^2\theta_p)$ is less than 4.0%. The situation changes a little for the comparison of $H_E(\cos\theta_p, M_{p\bar{p}})$ and $1-\cos^2\theta_p$: the maximum difference is still less than 4.0% for the 8 bins in the center, while for the bins at the edges differences between 20% and 30% are observed.

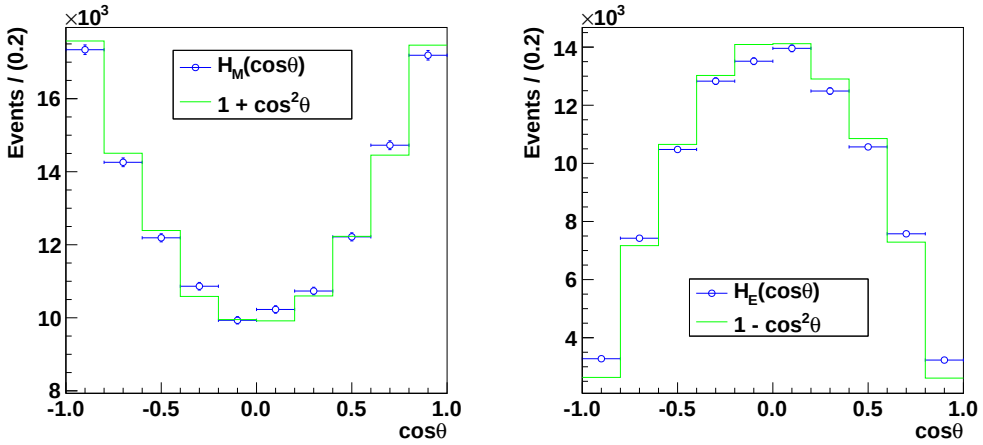

(a) $H_M(\cos\theta_p, M_{p\bar{p}})$ (b) $H_E(\cos\theta_p, M_{p\bar{p}})$

Fig. 8.1: Comparison of $H_M(\cos\theta_p, M_{p\bar{p}})$ and $H_E(\cos\theta_p, M_{p\bar{p}})$ (blue circles), as extracted from the MC simulation, and the $(1+\cos^2\theta_p)$ and $(1-\cos^2\theta_p)$ distributions (green histograms), for the mass interval corresponding to th.–1.950 GeV/c^2.

In Eq. 8.1, a normalization factor must be considered between the two contributions $H_M(\cos\theta_p, M_{p\bar{p}})$ and $H_E(\cos\theta_p, M_{p\bar{p}})$ by integrating the functions $1+\cos^2\theta_p$ and $1-\cos^2\theta_p$. This factor is equal to 2 for the full angular distribution of the proton. To extract the ratio of proton FFs, the following fit function is used:

$$f(\cos\theta_p) = \mathcal{A}\left[H_M(\cos\theta_p, M_{p\bar{p}}) + \frac{R_{em}^2}{2<\tau>} H_E(\cos\theta_p, M_{p\bar{p}})\right], \tag{8.2}$$

where $f(\cos\theta_p) = \frac{dN}{d\cos\theta_p}$ is the proton angular distribution after the background subtraction, divided by the MC efficiency (see Appendix C). The global parameter $\mathcal{A}$ is equivalent to an overall normalization factor. Due to the finite invariant-mass range of the proton angular distribution, the constant $< \tau >$ has an uncertainty which affects the uncertainty of the ratio (R_{em}). However, considering the low statistics, this effect is negligible and a fixed constant $< \tau >$ is included in the fit function to avoid the additional calculation.

The steps below summarize the procedure to extract the ratio of proton FFs for each mass interval:

- The proton angular distribution, H_{ij}^{rec}, is produced for each mass interval at each cms energy, with $i \in [1,6]$ representing the mass interval and $j \in [1,7]$ representing seven different data sets.

- The pure reconstructed signal, H_{ij}^{sig}, is obtained by subtracting the background H_{ij}^{bkg} from H_{ij}^{rec}.

- The expected physics data, H_{ij}^{dat}, is obtained from H_{ij}^{sig} divided by the MC efficiency H_{ij}^{eff}.

- The expected physics data from the different energy data sets are combined: $H_i^{\mathrm{dat}} = \sum_{j=1}^{n=7} H_{ij}^{\mathrm{dat}}$.

- The three distributions, H_i^{dat}, $H_M(\cos\theta_p, M_{p\bar{p}})$ and $H_E(\cos\theta_p, M_{p\bar{p}})$, are normalized.

- The ratio of proton FFs is extracted by fitting the combined proton angular distribution, H_i^{dat}, to Eq. 8.2 with the distributions $H_M(\cos\theta_p, M_{p\bar{p}})$ and $H_E(\cos\theta_p, M_{p\bar{p}})$ for each mass interval.

Figure 8.2 shows the fit results for the proton angular distribution combined from all seven data sets. The goodness of fit, χ^2/ndf with $ndf = 9$, is also shown in the figures.

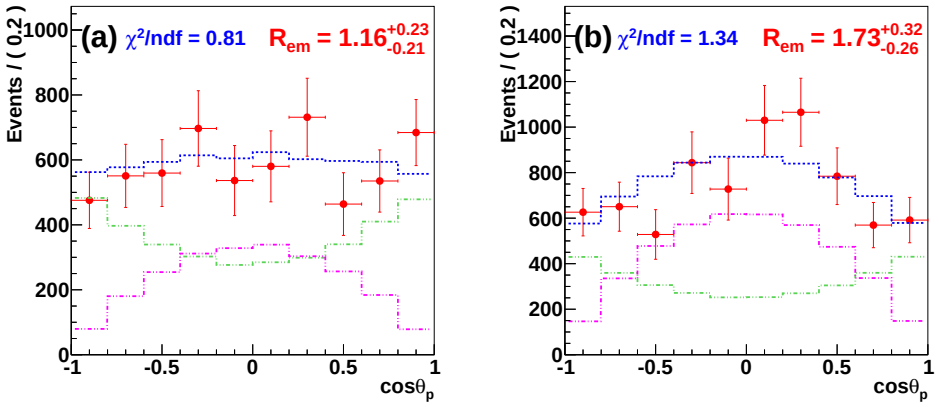

(a) th.–1.950 GeV/c^2 (b) 1.950–2.025 GeV/c^2

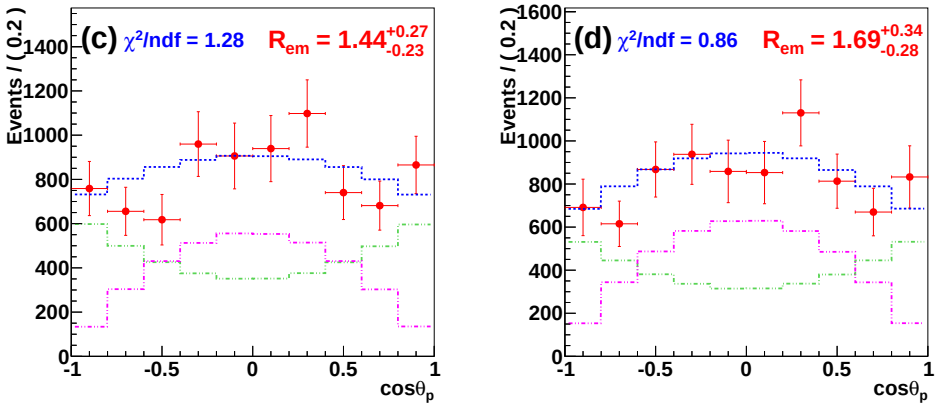

(c) 2.025–2.100 GeV/c^2 (d) 2.100–2.200 GeV/c^2

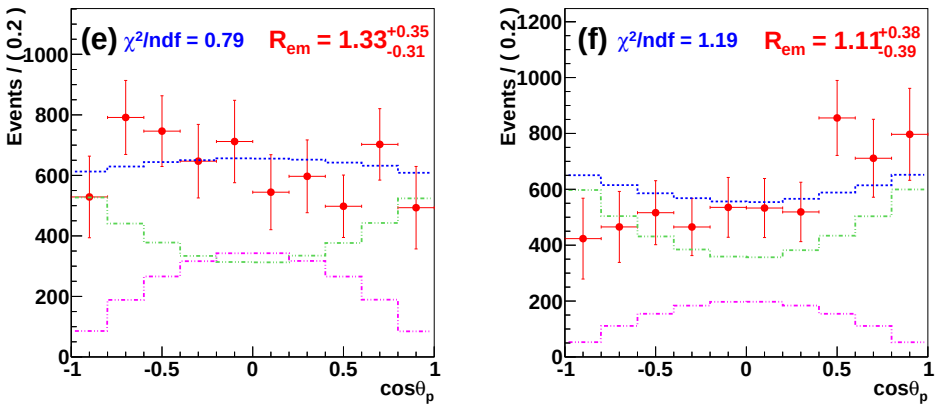

(e) 2.200–2.400 GeV/c^2 (f) 2.400–3.000 GeV/c^2

Fig. 8.2: The $\cos\theta_p$ distribution for different $p\bar{p}$ mass intervals. The red points with error bars show the data, the blue dashed line represents the fit results, and the green and pink dash-dotted lines correspond to G_M and G_E contributions, respectively.

An alternative method, the so called "method of moments" (MM) [88] (for details see Appendix A.2), is applied to extract the ratio of proton FFs, which provides a cross-check to the results from the fit. For the direct process of $e^+e^- \to p\bar{p}$, the expectation value, or the moment, of $\cos^2\theta_p$ derived from Eq. 2.17 is given by:

$$< \cos^2\theta_p >= \frac{1}{5} \times \frac{4\tau + R_{em}^2}{2\tau + R_{em}^2}. \tag{8.3}$$

The ratio of proton FFs and its uncertainty can be calculated with Eq. 8.3 as:

$$R_{em} = \sqrt{2 < \tau > \times \frac{5 < \cos^2\theta_p > -2}{1 - 5 < \cos^2\theta_p >}}, \tag{8.4}$$

$$\Delta R_{em} = \sqrt{\left(\frac{< \tau >}{R_{em}} \frac{5}{(1 - 5 < \cos^2\theta >)^2} \Delta < \cos^2\theta > \right)^2 + \left(\frac{R_{em}}{2 < \tau >} \Delta < \tau > \right)^2}, \tag{8.5}$$

where $< \cos^2\theta_p >$ and $\Delta < \cos^2\theta_p >$ are the average value and the uncertainty of the $\cos^2\theta_p$ distribution, and $< \tau >$ and $\Delta < \tau >$ are the average value and the uncertainty of the corresponding $p\bar{p}$ invariant-mass distribution, respectively. In principle, this method is only valid for the direct annihilation process $e^+e^- \to p\bar{p}$, in which the differential cross section has an analytic form (Eq. 2.17). For the ISR process, since the differences between the distributions $H_M(\cos\theta_p, M_{p\bar{p}})$ and $H_E(\cos\theta_p, M_{p\bar{p}})$ and the terms $1+\cos^2\theta_p$ and $1-\cos^2\theta_p$ are less than 4% for the central bins but 20%-30% for the edges of $H_E(\cos\theta_p, M_{p\bar{p}})$, this method is only used here as a cross-check of the fit results. The ratio of proton FFs calculated with the method of moments is an approximation for the ISR process.

Results for the ratio of proton FFs are summarized in Tab. 8.1, in which only statistical errors are included. Results from the fit and the method of moments are consistent with each other. Statistics ($\mathcal{N}_{\text{dat}}$) for the angular distribution of each mass interval are summarized in Tab. 8.2. The MC efficiency is the mean value from the seven MC simulations for the different data sets.

Tab. 8.1: Ratio of proton FFs from the fit and the MM calculation.

$M^{\mathrm{inv}}_{p\bar{p}}$ [GeV/c^2]	$R^{\mathrm{fit}}_{em} \pm \Delta R^{\mathrm{fit}}_{em}$	χ^2/ndf	$R^{\mathrm{MM}}_{em} \pm \Delta R^{\mathrm{MM}}_{em}$
1.876–1.950	$1.16^{+0.23}_{-0.21}$	0.80	1.16±0.20
1.950–2.025	$1.73^{+0.32}_{-0.26}$	1.22	1.75±0.26
2.025–2.100	$1.44^{+0.27}_{-0.23}$	1.29	1.34±0.20
2.100–2.200	$1.69^{+0.34}_{-0.28}$	0.86	1.60±0.23
2.200–2.400	$1.34^{+0.34}_{-0.30}$	0.71	1.17±0.24
2.400–3.000	$1.13^{+0.38}_{-0.38}$	1.22	1.14±0.30

Tab. 8.2: Statistics ($\mathcal{N}_{\mathrm{dat}}$) for the extraction of the ratio of proton FFs. The efficiency $\bar{\epsilon}_{\mathrm{MC}}$ is the mean value from the seven MC simulations for different data sets.

$M^{\mathrm{inv}}_{p\bar{p}}$ [GeV/c^2]	$\mathcal{N}_{\mathrm{dat}}$	$\mathcal{N}_{\mathrm{bkg}}$	$\mathcal{N}_{\mathrm{sig}}$	$\bar{\epsilon}_{\mathrm{MC}}(\%)$	$\mathcal{N}_{\mathrm{phy}}$
1.877–1.950	461	93±3	368±22	6.51	5578±330
1.950–2.025	617	180±4	437±25	6.44	6781±392
2.025–2.100	685	204±5	481±27	6.33	7547±418
2.100–2.200	699	225±5	474±27	6.30	7491±425
2.200–2.400	664	305±6	359±26	6.52	5312±395
2.400–3.000	844	493±8	351±30	7.34	4704±404

8.2 Cross section of $e^+e^- \to p\bar{p}$ and effective form factor of the proton

The cross section of the process $e^+e^- \to p\bar{p}$, measured for 31 $p\bar{p}$-invariant-mass bins, is calculated according to the following equation:

$$\sigma_i = \frac{1}{\mathcal{L}_i} \sum_{j=1}^{n=7} \frac{N_{ij}}{\epsilon_{ij}(1+\delta)_{ij}}, \tag{8.6}$$

where i stands for the ith invariant-mass bin and j, running over all seven data sets, for the jth data set. In Eq. 8.6, N_{ij} is the number of $p\bar{p}\gamma$ signal events after background subtraction and ϵ_{ij} and $(1+\delta)_{ij}$ are, respectively the efficiency and the radiative correction factor of the $e^+e^- \to p\bar{p}\gamma$ process. The luminosity $\mathcal{L}_i$ is the total ISR luminosity calculated according to

$$\mathcal{L}_i = -\sum_{j=1}^{n=7} \mathcal{L}_j^{\text{int}} \int W(s_j, x_{ij}) dx_{ij},\ x_{ij} = 1 - \frac{q_{ij}^2}{s_j}, \tag{8.7}$$

where $W(s_j, x_{ij})$ is the ISR radiator function (2.27), and $\mathcal{L}_j^{\text{int}}$ is the total luminosity of the data set at the cms energy $\sqrt{s_j}$. The MC efficiency, ϵ_{ij}, is obtained from the $e^+e^- \to p\bar{p}\gamma$ full MC simulation including ISR-NLO, FSR and VP. The radiative correction factor $(1+\delta)_{ij}$ is determined from both the full MC simulation and the MC simulation only including ISR Leading-Order (ISR-LO) process. Collected statistics, $p\bar{p}\pi^0$ background, MC efficiency and radiative correction factor are listed for each individual data set in Appendix C (Table B.1 - B.7).

Based on Eq. 2.22, the effective FF of the proton is extracted as

$$|G_{\text{eff}}|^2 = \frac{3\, q^2 \sigma}{4\pi\alpha^2\beta\, C(1+\frac{1}{2\tau})}. \tag{8.8}$$

The measured results of the cross section of $e^-e^+ \to p\bar{p}$ according to Eq. 8.6 and the effective FF of the proton according to Eq. 8.8 are summarized in Tab. 8.3. In this table, only statistical errors are quoted. The number $\mathcal{N}_{\text{phy}}$ is the expected number of physics signal events in the ith bin.

Tab. 8.3: The cross section of $e^+e^- \to p\bar{p}$ and the effective FF of the proton, together with the ISR luminosity and the expected number of physics signal events for different $p\bar{p}$ invariant-mass bins.

$M_{p\bar{p}}^{\text{inv}}$ [GeV/c^2]	$\mathcal{L}$ [pb^{-1}]	$\mathcal{N}_{\text{phy}}$	σ [pb]	$\lvert G_{\text{eff}}\rvert$
1.877–1.900	2.10	1543±146	735.55±69.69	0.405±0.019
1.900–1.925	2.29	1685±166	736.75±72.36	0.320±0.016
1.925–1.950	2.34	1773±176	757.18±75.25	0.292±0.015
1.950–1.975	2.40	2094±192	873.26±80.23	0.295±0.014
1.975–2.000	2.45	2298±205	936.08±83.50	0.294±0.013
2.000–2.025	2.51	2202±202	876.06±80.42	0.276±0.013
2.025–2.050	2.57	2487±215	965.80±83.39	0.284±0.012
2.050–2.075	2.64	2748±227	1042.18±86.00	0.291±0.012
2.075–2.100	2.70	2159±206	798.97±76.27	0.252±0.012

$M^{\text{inv}}_{p\bar{p}}$ [GeV/c^2]	$\mathcal{L}$ [pb^{-1}]	N_{phy}	σ [pb]	$\lvert G_{\text{eff}}\rvert$
2.100–2.125	2.77	2323±210	839.13±75.97	0.256±0.012
2.125–2.150	2.84	1728±185	609.20±65.24	0.217±0.012
2.150–2.175	2.91	2028±196	697.51±67.36	0.232±0.011
2.175–2.200	2.98	1386±168	465.07±56.36	0.189±0.011
2.200–2.225	3.06	1151±158	376.66±51.63	0.170±0.012
2.225–2.250	3.13	1062±147	338.90±47.05	0.161±0.011
2.250–2.275	3.22	1034±144	321.45±44.70	0.157±0.011
2.275–2.300	3.30	646±122	195.82±36.84	0.123±0.012
2.300–2.350	6.86	1079±159	157.20±23.17	0.111±0.008
2.350–2.400	7.24	842±142	116.33±19.57	0.096±0.008
2.400–2.450	7.64	843±136	110.38±17.85	0.094±0.008
2.450–2.500	8.08	795±129	98.43±15.96	0.090±0.007
2.500–2.550	8.55	694±120	81.17±14.08	0.083±0.007
2.550–2.600	9.06	656±115	72.45±12.65	0.079±0.007
2.600–2.650	9.62	717±117	74.55±12.14	0.081±0.007
2.650–2.700	10.23	341± 93	33.29± 9.07	0.055±0.008
2.700–2.750	10.90	266± 89	24.36± 8.16	0.048±0.008
2.750–2.800	11.64	216± 85	18.58± 7.32	0.042±0.008
2.800–2.850	12.46	232± 88	18.60± 7.06	0.043±0.008
2.850–2.900	13.37	369± 99	27.59± 7.39	0.053±0.007
2.900–2.950	14.39	129± 82	8.96± 5.69	0.031±0.010
2.950–3.000	15.53	141± 86	9.07± 5.52	0.031±0.010

CHAPTER 9

Systematic Uncertainties and Summary of Results

In this chapter, the systematic uncertainties on the ratio of proton FFs and the $e^+e^- \to p\bar{p}$ cross section are presented. The final results of the ratio of proton FFs, the cross section and the effective FF of the proton are summarized in the last section of the chapter.

9.1 Systematic uncertainties on ratio of proton form factors

Systematic uncertainties on the ratio of proton FFs are studied separately for each mass interval. The value of the ratio is determined by the shape of the proton angular distribution. Sources of systematic uncertainties on the ratio include the number of bins for the fit of the proton angular distribution, the cut value on the χ^2_{4C} distribution and the background subtraction.

- As shown in the previous chapter, the full proton angular distribution is available for all the $p\bar{p}$ invariant-mass intervals from the $e^+e^- \to p\bar{p}\gamma$ analysis. To extract the ratio of proton FFs, the proton angular distribution is divided into 10 bins (Section 8.1). To study the possible systematic uncertainty due to the chosen binning, the number of bins

is changed to 8 or 15. The change of binning number affects only slightly the shape of the proton angular distribution. The largest difference between the nominal results for the ratio R_{em} (Tab. 8.1) and the new results using 8 and 15 bins is taken as the systematic uncertainty. The uncertainty for the method of moments is evaluated with the same method.

- The cut value on the χ^2_{4C} distributions is changed from 50 to 45 or 60, and the values of the ratio are extracted again. This change affects the proton angular distribution by changing the ratio of signal to background before the estimated background subtraction in the data, therefore it affects the value of the ratio of proton FFs. To compare the new values of the ratio to the nominal one in Tab. 8.1 separately, the largest difference between the nominal results for the ratio R_{em} (Tab. 8.1) and the new results using 45 and 60 as the new limits of χ^2_{4C} is taken as the systematic uncertainty. The uncertainty for the method of moments is evaluated with the same method.

- The angular distribution of the background calculated in Section 6.2 changes the proton angular distribution, thus the result of the form-factors ratio is affected depending on whether the background is subtracted correctly. To find out if a correct and stable background estimation is obtained in Chapter 6, two groups of random proton angular distributions are generated according to the proton angular distribution from the $p\bar{p}\pi^0$ data (see for instance Fig. 6.2 (c) for 4.230 GeV). For the proton angular distribution from the $p\bar{p}\pi^0$ data in the ith mass interval of the jth data set, assuming the total number of events is $\mathcal{N}_{ij} \pm \Delta\mathcal{N}_{ij}$, the two groups of random distributions of the proton are:

  - group I: 890 random distributions with the generated event number $\mathcal{N}_{ij} + \Delta\mathcal{N}_{ij}$,
  - group II: 886 random distributions with the generated event number $\mathcal{N}_{ij} - \Delta\mathcal{N}_{ij}$.

  By subtracting the weighted random background (same calculation as in Section 6.1) from the selected data, 890 or 866 values of the ratio are extracted for each mass interval. The values in the two groups are fitted to Gaussian distributions and their mean values are compared with the correspoding nominal ratio in Tab. 8.1. The largest absolute difference is taken as the systematic uncertainty for the background estimation.

Figure 9.1 shows the fit results of the ratio extracted after subtraction of the random background, for the mass interval th.–1.950 GeV/c^2. In the broadest and last mass interval (2.4–3.0 GeV/c^2), the systematic uncertainty is larger than in other bins due to low statistics and high background contamination. The results of the comparison show that the background estimation is correct and stable.

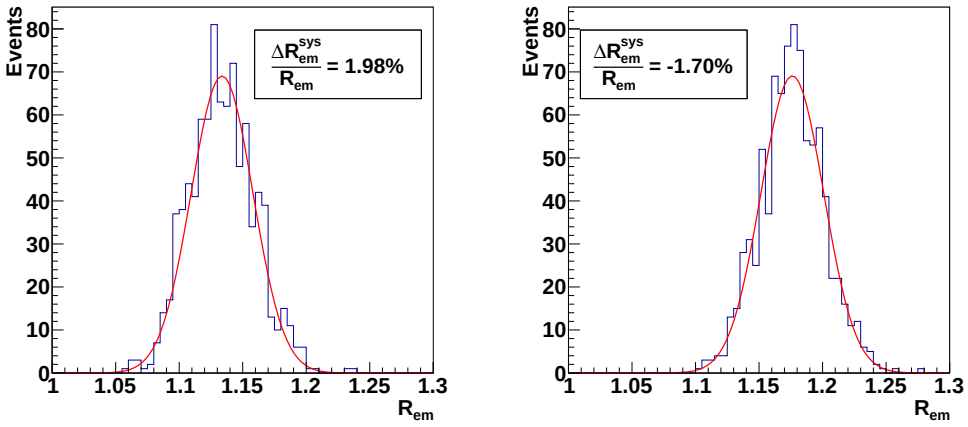

(a) Group I (b) Group II

Fig. 9.1: Fit of the distributions of the ratios (blue histogram) extracted after the random background subtraction from the data in the mass interval th.–1.950 GeV/c^2. The red line respresents the Gaussian fit result.

The systematic uncertainty from the model of the proton FFs in the event generator, PHOKHARA 9.1, is negligible for the ratio of proton FFs. The default model of the proton FFs in the event generator is provided by the fit to the world data in both the SL and TL regions [83]. In the TL region, BABAR results were used [47]. Figure 9.3 shows the ratio of proton FFs from this analysis (red dots with error bars) and from the model (light-blue curve) in the event generator. The results are consistent with the model within the uncertainty, therefore the possible systematic uncertainty introduced by using a different model in the event generator is assumed to be negligible within the precision of the measurement.

Table. 9.1 summarizes the summary of the systematic uncertainties on the ratio of proton FFs, after using the fit and the method of moments to extract R_{em}.

Tab. 9.1: Summary of systematic uncertainties (%) on the ratio of proton FFs.

$M^{\mathrm{inv}}_{p\bar{p}}$ [GeV/c^2]		th.–1.95	1.95–2.025	2.025–2.1	2.1–2.2	2.2–2.4	2.4–3.0
Fit (%)	Bins	6.1	3.7	2.3	9.0	13.3	7.7
	χ^2_{4C}	2.0	2.0	2.8	7.6	8.0	3.8
	Bkgd	2.0	1.6	2.1	1.3	1.0	6.0
	Total	6.7	4.5	4.2	11.9	15.6	10.5
MM (%)	Bins	6.2	4.8	3.9	5.3	9.5	9.1
	χ^2_{4C}	5.1	2.3	2.9	6.9	9.4	2.0
	Bkgd	1.6	1.4	1.4	1.0	0.6	4.1
	Total	8.2	5.5	5.1	8.8	13.4	10.2

9.2 Systematic uncertainties on cross section and effective form factor

The sources of systematic uncertainties on the cross section and on the effective FF measurements include the absolute number of signal events (which depends on the efficiencies of the selection criteria), the background estimation and the measurement of the luminosity.

- The systematic uncertainties on the cross section and on the effective form factor were carefully studied in the analysis of $e^+e^-\to p\bar{p}$ with scan data in 2012 at BESIII [42]. In particular, the effects of differences between the data and MC simulations concerning the tracking efficiency and the E/p cut were studied for cms energies between 2.2324 and 3.671 GeV, which is a similar $p\bar{p}$ invariant-mass range as in the $e^+e^-\to p\bar{p}\gamma$ analysis with the ISR photon tagged. Since the uncertainty associated with these two sources is constant for all cms energies, the uncertainties in the cross-section measurement are set to 2.0% and 1.0% from the tracking efficiency (1.0% for each track) and E/p cut, respectively.

- The systematic uncertainty from the difference of the PID efficiency in the data and in the MC simulation is studied through the $e^+e^-\to p\bar{p}\pi^0$ process by using the data set at 3.773 GeV. A very clean sample of $p\bar{p}\pi^0$ events (14063 events) is obtained from the data after applying the $e^+e^-\to p\bar{p}\pi^0$ full event selection (see Chapter 6 for details).

To study the difference of the PID efficiency in data and MC, two additional event selections are performed for both the data and MC simulation (PHSP) by requiring that only one of the tracks is identified as proton (antiproton). The proton (antiproton) PID efficiency is calculated as the ratio of the number of $p\bar{p}\pi^0$ events selected with both tracks identified as proton and antiproton by the PID system and the number of events with only one track identified as proton (antiproton). This procedure is followed for both the data and MC simulation. The ratio of the PID efficiency in the data and in the MC simulation is shown in Fig. 9.2 ((b) for proton and (d) for antiproton). The systematic uncertainty due to the different PID efficiency in data and MC simulation is set to 1.0% for each track.

- The uncertainty of the total luminosity measurement is 1.1% for the data set at 3.773 GeV [76] and 1.0% for the other data sets [77]. This leads to 1.0% systematic uncertainty in the cross-section measurement.

The following contributions to the systematic uncertainties on the cross section are studied for each invariant mass bin:

- The uncertainty from the backgound subtraction is estimated by using the same method as in Section 9.1. The largest difference between the nominal cross section in Tab. 8.3 and the values of the cross sections after changing the background distibution by $\pm\Delta N_j$ is taken as the systematic uncertainty.

- The cross section of $e^+e^-\to p\bar{p}$ is calculated by changing the cut value on the χ^2_{4C} distribution from 50 to 45 or 60. The largest difference between the nominal cross section in Tab. 8.3 and the two new ones is taken as the systematic uncertainty from the 4C kinematic fit.

The uncertainty from the trigger efficiency is negligible. The trigger is 100% efficient for events with charged particles in the final state [89]. As mentioned in Section 9.1, the possible systematic uncertainty introduced by using a different model of the proton FFs in the event generator is also negligible in the measurement of the cross section.

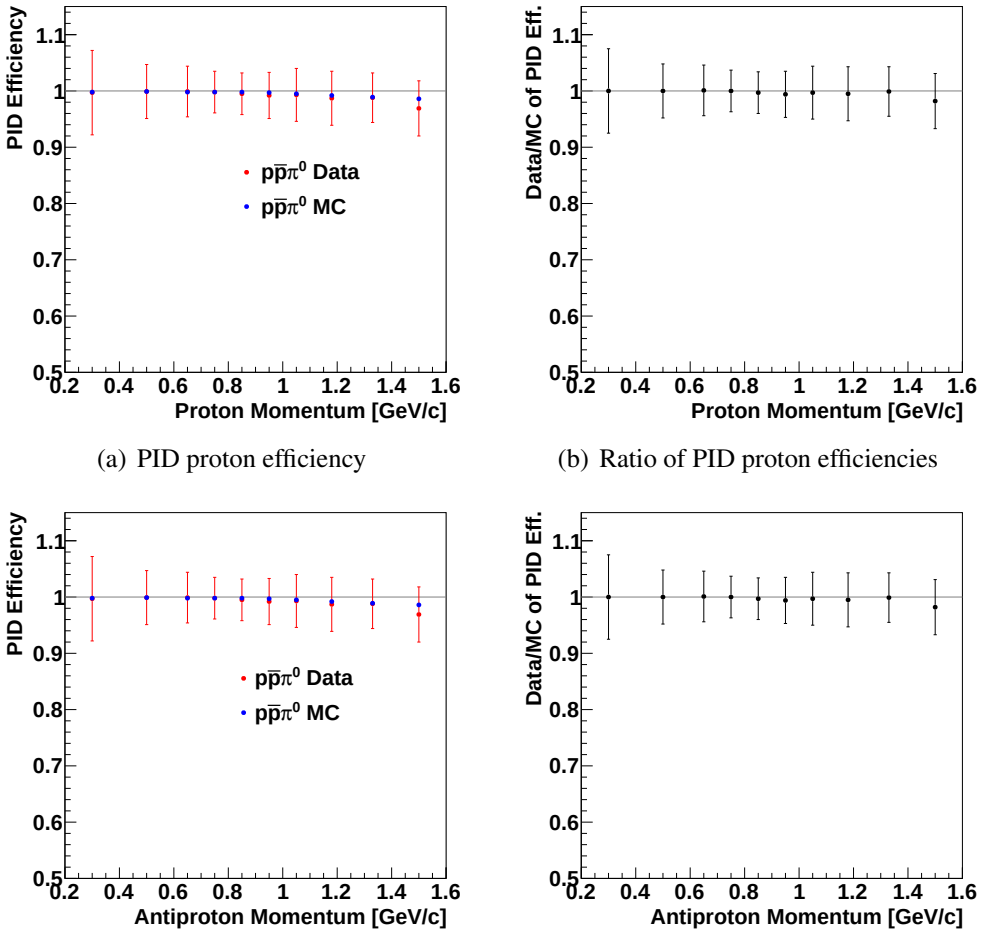

(a) PID proton efficiency

(b) Ratio of PID proton efficiencies

(c) PID antiproton efficiency

(d) Ratio of PID antiproton efficiencies

Fig. 9.2: PID efficiency obtained from the data and $p\bar{p}\pi^0$ MC simulation for (a) the proton and (c) the antiproton. The red and blue points represent the data and the MC simulation, respectively. The ratio of PID efficiencies in the data and MC simulation are shown in (b) and (d) for the proton and antiproton, respectively.

A summary of systematic uncertainties in the measurement of the $e^+e^- \to p\bar{p}$ cross section is listed in Tab. 9.2. According to Eq. 8.8, the systematic uncertainty in the measurement of the effective form factor of the proton is calculated as a half the uncertainty on the cross section for each invariant-mass bin.

Tab. 9.2: Summary of systematic uncertainties (%) on the cross section of $e^+e^- \to p\bar{p}$ and on the effective FF of the proton.

$M^{\mathrm{inv}}_{p\bar{p}}$ [GeV/c^2]	Trk. (%)	PID (%)	E/p (%)	Lumi. (%)	χ^2_{4C} (%)	Bkg (%)	Total on σ (%)	Total on $\lvert G_{\mathrm{eff}}\rvert$ (%)
1.877–1.900	2.0	2.0	1.0	1.0	1.0	2.5	4.1	2.1
1.900–1.925	2.0	2.0	1.0	1.0	3.7	0.4	4.9	2.4
1.925–1.950	2.0	2.0	1.0	1.0	0.8	0.6	3.3	1.7
1.950–1.975	2.0	2.0	1.0	1.0	2.1	0.6	3.8	1.9
1.975–2.000	2.0	2.0	1.0	1.0	2.3	0.7	4.0	2.0
2.000–2.025	2.0	2.0	1.0	1.0	0.5	0.6	3.3	1.6
2.025–2.050	2.0	2.0	1.0	1.0	2.4	0.6	4.0	2.0
2.050–2.075	2.0	2.0	1.0	1.0	2.3	0.6	3.9	2.0
2.075–2.100	2.0	2.0	1.0	1.0	3.3	0.7	4.6	2.3
2.100–2.125	2.0	2.0	1.0	1.0	1.7	0.6	3.7	1.8
2.125–2.150	2.0	2.0	1.0	1.0	3.9	0.6	5.0	2.5
2.150–2.175	2.0	2.0	1.0	1.0	1.1	0.6	3.4	1.7
2.175–2.200	2.0	2.0	1.0	1.0	1.4	0.7	3.5	1.8
2.200–2.225	2.0	2.0	1.0	1.0	1.4	1.0	3.6	1.8
2.225–2.250	2.0	2.0	1.0	1.0	4.0	1.0	5.2	2.6
2.250–2.275	2.0	2.0	1.0	1.0	2.7	0.8	4.2	2.1
2.275–2.300	2.0	2.0	1.0	1.0	4.0	1.3	5.3	2.6
2.300–2.350	2.0	2.0	1.0	1.0	4.1	1.5	5.4	2.7
2.350–2.400	2.0	2.0	1.0	1.0	0.9	1.5	3.6	1.8
2.400–2.450	2.0	2.0	1.0	1.0	2.1	1.3	4.0	2.0
2.450–2.500	2.0	2.0	1.0	1.0	2.8	1.1	4.3	2.2
2.500–2.550	2.0	2.0	1.0	1.0	4.8	1.4	5.9	2.9
2.550–2.600	2.0	2.0	1.0	1.0	4.0	1.1	5.2	2.6
2.600–2.650	2.0	2.0	1.0	1.0	3.0	0.9	4.4	2.2
2.650–2.700	2.0	2.0	1.0	1.0	8.7	1.6	9.4	4.7

$M^{\text{inv}}_{p\bar{p}}$ [GeV/c^2]	Trk. (%)	PID (%)	E/p (%)	Lumi. (%)	χ^2_{4C} (%)	Bkg (%)	Total on σ (%)	Total on $\lvert G_{\text{eff}}\rvert$ (%)
2.700–2.750	2.0	2.0	1.0	1.0	11.0	2.4	11.7	5.9
2.750–2.800	2.0	2.0	1.0	1.0	23.6	2.8	24.0	12.0
2.800–2.850	2.0	2.0	1.0	1.0	9.1	3.3	10.2	5.1
2.850–2.900	2.0	2.0	1.0	1.0	8.1	2.1	8.9	4.5
2.900–2.950	2.0	2.0	1.0	1.0	8.5	6.0	10.8	5.4
2.950–3.000	2.0	2.0	1.0	1.0	15.2	5.9	16.6	8.3

9.3 Summary of results

The ratio of proton FFs was studied from the process $e^+e^-\to p\bar{p}\gamma$ with the ISR photon tagged for q^2 from the threshold to 9.0 (GeV/c)^2, with a total luminosity of 7.41 fb^{-1} using the BESIII data collected at seven cms energies between 3.773 and 4.6 GeV. The ratio was extracted by fitting the proton angular distribution in 6 $p\bar{p}$ mass intervals; the method of moments was also used to calculate the ratio. Table 9.3 shows the results for R_{em} including statistical and systematic uncertainties. The third column shows the results for R_{em} after a two-parameter fit on the proton angular distribution, while the fourth column shows the results for R_{em} after applying the method of moments. Figure 9.3 shows the ratio of proton FFs extracted from the process $e^+e^-\to p\bar{p}\gamma$ with the ISR photon tagged through the fit and the method of moments; the light blue line represents the model of the FF ratio used in the MC event generator.

The cross section of $e^+e^-\to p\bar{p}$ and the effective FF of the proton were measured in 31 q^2-bins from the $p\bar{p}$-threshold up to 9.0 (GeV/c)^2. The results are summarized in Tab. 9.4 including statistical and systematic uncertainties. Figure 9.4 shows the cross section of $e^+e^-\to p\bar{p}$ and the effective FF of the proton measured from the $e^+e^-\to p\bar{p}\gamma$ analysis with the ISR photon tagged.

Tab. 9.3: The ratio of proton FFs from the $e^+e^-\to p\bar{p}\gamma$ process with the ISR photon tagged for different invariant mass bins.

$M^{\rm inv}_{p\bar{p}}$ [GeV/c^2]	$R_{em} \pm \Delta R^{\rm stat.}_{em} \pm \Delta R^{\rm syst.}_{em}$ (fit)	$R_{em} \pm \Delta R^{\rm stat.}_{em} \pm \Delta R^{\rm syst.}_{em}$ (MM)
1.877–1.950	$1.16^{+0.23}_{-0.21}\pm0.08$	$1.16\pm0.20\pm0.10$
1.950–2.025	$1.73^{+0.32}_{-0.26}\pm0.08$	$1.75\pm0.26\pm0.10$
2.025–2.100	$1.44^{+0.27}_{-0.23}\pm0.06$	$1.34\pm0.20\pm0.07$
2.100–2.200	$1.69^{+0.34}_{-0.28}\pm0.20$	$1.60\pm0.23\pm0.14$
2.200–2.400	$1.34^{+0.34}_{-0.30}\pm0.21$	$1.17\pm0.25\pm0.16$
2.400–3.000	$1.13^{+0.38}_{-0.38}\pm0.12$	$1.14\pm0.30\pm0.12$

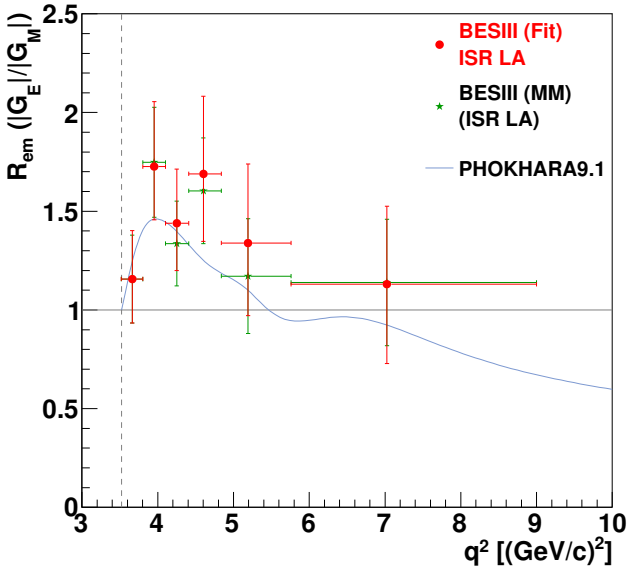

Fig. 9.3: The ratio of proton FFs extracted from the $e^+e^-\to p\bar{p}\gamma$ process with the ISR photon tagged. The light-blue line is the model of the FF ratio used in the event generator.

Tab. 9.4: The cross section of $e^+e^-\to p\bar{p}$ and the effective FF of the proton from the $e^+e^-\to p\bar{p}\gamma$ process with the ISR photon tagged, for different invariant mass bins.

$M^{\rm inv}_{p\bar{p}}$ [GeV/c^2]	σ [pb]	$\lvert G_{\rm eff}\rvert$
1.877–1.900	$736\pm70\pm30$	$0.405\pm0.019\pm0.009$
1.900–1.925	$737\pm72\pm36$	$0.320\pm0.016\pm0.008$

$M^{\mathrm{inv}}_{p\bar{p}}$ [GeV/c^2]	σ [pb]	$\lvert G_{\mathrm{eff}}\rvert$
1.925–1.950	757±75±25	0.292±0.015±0.005
1.950–1.975	873±80±33	0.296±0.014±0.006
1.975–2.000	936±83±37	0.294±0.013±0.006
2.000–2.025	876±80±29	0.276±0.013±0.004
2.025–2.050	966±83±39	0.284±0.012±0.006
2.050–2.075	1042±86±41	0.291±0.012±0.006
2.075–2.100	799±76±37	0.252±0.012±0.006
2.100–2.125	839±76±31	0.256±0.012±0.005
2.125–2.150	609±65±30	0.217±0.012±0.005
2.150–2.175	698±67±24	0.232±0.011±0.004
2.175–2.200	465±56±16	0.189±0.011±0.003
2.200–2.225	377±52±14	0.170±0.012±0.003
2.225–2.250	339±47±18	0.161±0.011±0.004
2.250–2.275	321±45±14	0.157±0.011±0.003
2.275–2.300	196±37±10	0.123±0.012±0.003
2.300–2.350	157±23±8	0.1107±0.0082±0.0030
2.350–2.400	116±20±4	0.0960±0.0081±0.0017
2.400–2.450	110±18±4	0.0944±0.0076±0.0019
2.450–2.500	98±16±4	0.0901±0.0073±0.0020
2.500–2.550	81±14±5	0.0828±0.0072±0.0024
2.550–2.600	72±13±4	0.0792±0.0069±0.0021
2.600–2.650	75±12±3	0.0814±0.0066±0.0018
2.650–2.700	33.3±9.1±3.1	0.0551±0.0075±0.0026
2.700–2.750	24.4±8.2±2.8	0.0478±0.0080±0.0028
2.750–2.800	18.6±7.3±4.5	0.0423±0.0083±0.0051
2.800–2.850	18.6±7.1±1.9	0.0430±0.0081±0.0022
2.850–2.900	27.6±7.4±2.5	0.0530±0.0071±0.0024
2.900–2.950	9.0±5.7±1.0	0.0307±0.0097±0.0017
2.950–3.000	9.1±5.5±1.5	0.0313±0.0095±0.0026

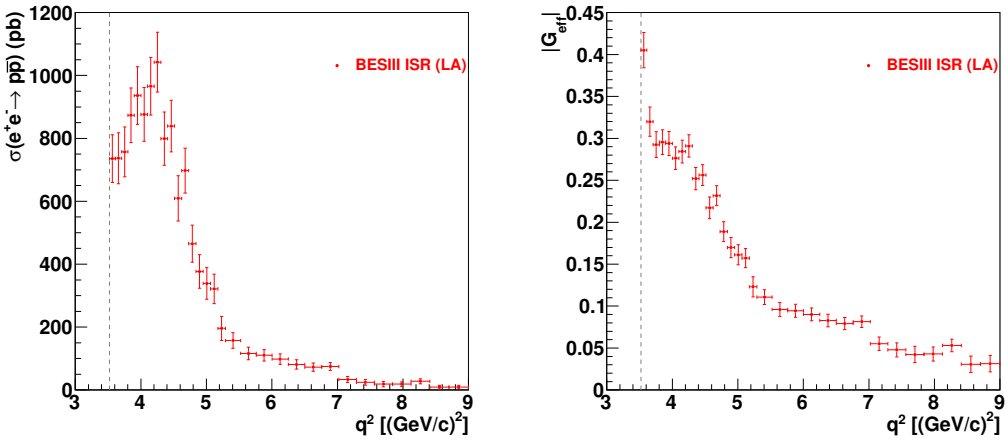

(a) Cross section (b) Effective FF

Fig. 9.4: (a) The cross section of $e^+e^- \to p\bar{p}$ and (b) the effective FF of the proton measured from the $e^+e^- \to p\bar{p}\gamma$ process with the ISR photon tagged (Large Angle, LA).

CHAPTER 10

Analysis of $e^+e^- \to p\bar{p}\gamma$ with ISR Photon Untagged

As mentioned in Chapter 4, the ISR photon is most likely emitted in the forward direction with respect to the emitting beam, therefore it escapes along the beam pipe undetected. An analysis with only the charged tracks detected is performed using the same data sets as in the analysis with the ISR photon tagged. The ratio of proton FFs and the cross section of $e^+e^- \to p\bar{p}$, as well as the effective FF of the proton, are measured. The advantages of the analysis with the ISR photon untagged are higher statistics and lower background compared to the one with the ISR photon tagged, but the selection efficiency is non-flat both in the angular distribution of the proton (see Appendix C) and in the $p\bar{p}$ invariant-mass distribution.

10.1 Signal event selection

The same criteria to select charged tracks as in the analysis with the ISR photon tagged (see Section 5.1.1) are used in this analysis. Instead of applying the cut on the 4C kinematic fit, cuts are performed on the missing momentum ($\vec{p}_{\rm miss}$) and the missing mass-squared ($M^2_{\rm miss}$) recoiling against the $p\bar{p}$ system. The missing momentum is defined as

$$\vec{p}_{\rm miss} = \vec{k}_1 + \vec{k}_2 - \vec{p}_1 - \vec{p}_2, \tag{10.1}$$

where $\vec{k}_1$ ($\vec{k}_2$) and $\vec{p}_1$ ($\vec{p}_2$) are the three-momentum of the electron (positron) and the antiproton (proton), respectively. The missing mass-squared is defined as

$$M^2_{\text{miss}} = (k_1 + k_2 - p_1 - p_2)^2, \tag{10.2}$$

where k_1 (k_2) and p_1 (p_2) are the four-momentum of the electron (positron) and the antiproton (proton), respectively.

To select the signal events and suppress the background, the following cuts based on the missing momentum and missing mass-squared are applied:

- For the process $e^+e^-\to p\bar{p}\gamma$, the missing momentum is equivalent to the momentum of the ISR photon and is required to be in small cones at low or high polar angles (θ_{miss}) with respect to the positron beam: θ_{miss} || $\pi - \theta_{\text{miss}} < 0.125$ rad.

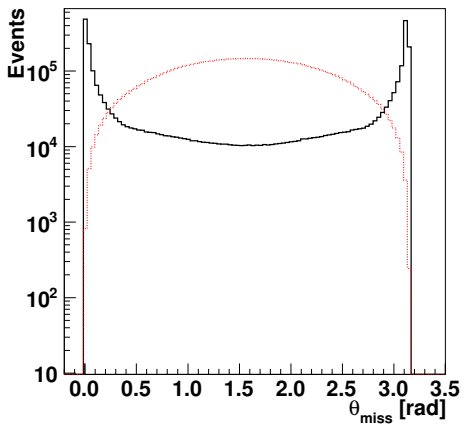

Fig. 10.1: Reconstructed angular distribution of the missing momentum from the signal MC simulation (black histogram) and the background channel $e^+e^- \to p\bar{p}\pi^0$ (red dotted histogram) after the charged-track selection.

Figure 10.1 shows the angular distribution of the missing momentum from the MC simulations of the $e^+e^-\to p\bar{p}\gamma$ signal and the $e^+e^-\to p\bar{p}\pi^0$ background. The distribution from signal MC is consistent with the angular distribution of the ISR photon at MC generator level in Fig. 4.1. The background from the process of $e^+e^-\to p\bar{p}\pi^0(\gamma)$ is strongly suppressed by this cut.

- A cut on the magnitude of the missing momentum, $|\vec{p}_{\text{miss}}| > 0.2$ GeV/c, is applied to ensure the emission of a hard ISR photon. This cut removes the events of the signal with low energetic ISR photons and helps to reject other background channels without ISR photons.

  For untagged $e^+e^- \to p\bar{p}\gamma$ events, the missing mass-squared corresponds to the mass-squared of the ISR photon, therefore it should be zero ($M^2_{\text{miss}} = 0$). Figure 10.2 shows the distributions of the missing mass-squared from the signal and background MC simulations at $\sqrt{s}$ = 3.773 and 4.230 GeV. The tails in the case of the signal MC simulations are due to the distortion from higher-order processes of the radiative corrections.

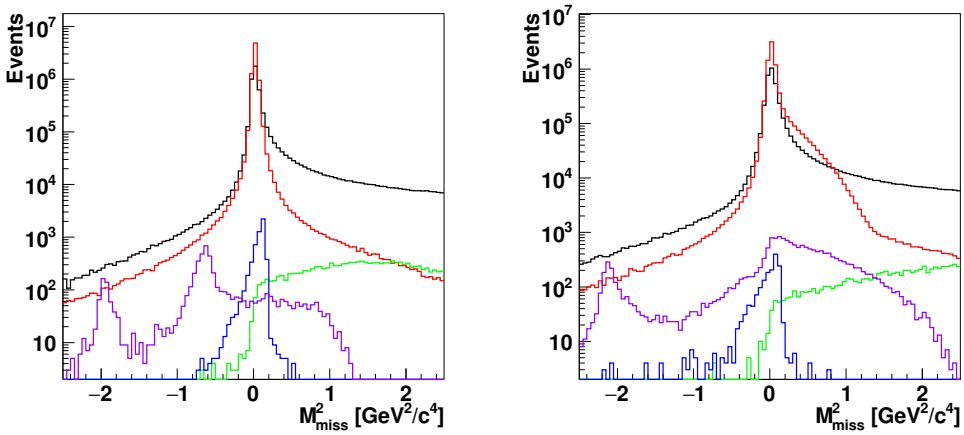

(a) 3.773 GeV (b) 4.230 GeV

Fig. 10.2: Reconstructed M^2_{miss} distribution from the MC simulations after the charged-track selection at (a) $\sqrt{s}$ = 3.773 GeV and (b) 4.230 GeV. The MC signal is shown in black together with different background channels: $e^+e^- \to p\bar{p}\pi^0$ in red, $e^+e^- \to \mu^+\mu^-\gamma$ in blue, two-gamma production in green and ISR BhaBha process in purple.

- A different cut on the missing mass-squared is applied according to the cms energy of the data set: $-0.02 < M^2_{\text{miss}} < 0.1$ GeV/c^2 for the data set at 3.773 GeV, and $-0.1 < M^2_{\text{miss}} < 0.2$ GeV/c^2 for the other data sets. This cut removes the background events from two charged tracks with an ISR photon, such as $e^+e^-\gamma$, $\mu^+\mu^-\gamma$, $K^+K^-\gamma$ and $\pi^+\pi^-\gamma$, and also suppresses the background from $e^+e^- \to p\bar{p}\pi^0$. The tight cut

on M^2_{miss} for the data set at 3.773 GeV is applied to reject the background from the radiative decays $J/\psi \to p\bar{p}\gamma$ and $\psi' \to p\bar{p}\gamma$.

- Previous cuts applied on θ_{miss} and M^2_{miss} lead to a near-zero efficiency of the signal in the region $|\cos\theta^{p\bar{p}}_{p,\bar{p}}| \geq 0.75$, where $\theta^{p\bar{p}}_{p,\bar{p}}$ is the angle of the proton or antiproton in the $p\bar{p}$ cms system. However, the background from the ISR BhaBha process is shown at $\cos\theta^{p\bar{p}}_{p,\bar{p}} \simeq 0.8$ (-0.8) for the positive (negative) charged track. These non-symmetric peaks are due to the interference of the initial- and final-state radiation of the BhaBha events. To remove this kind of background, a cut of $|\cos\theta^{p\bar{p}}_{p,\bar{p}}| < 0.75$ is required.

- An additional cut on the $p\bar{p}$ invariant mass is applied depending on the cms energy of the data set: $M_{p\bar{p}} < 2.9$ GeV/c^2 for the data set at 3.773 GeV, and $M_{p\bar{p}} < 4.0$ GeV/c^2 for other data sets. The reduced range of $p\bar{p}$ invariant mass for the data set at 3.773 GeV also helps to reject the background from the $p\bar{p}$ radiative decays of the J/ψ and ψ' resonances.

Figure 10.3 shows the $p\bar{p}$ invariant-mass distribution obtained by combining all the signal candidates from seven data sets, after applying all the cuts mentioned above. The $J/\psi \to p\bar{p}$ and $\psi' \to p\bar{p}$ decays are clearly seen at $M_{p\bar{p}} \sim 3.1$ and 3.7 GeV/c^2, respectively. Near the threshold of $p\bar{p}$ production, data are strongly suppressed by the selection criteria. When the photon has high energy and is emitted into the beam pipe, the hadronic system is in the low-mass range and strongly boosted into the opposite beam pipe. The opening angle between the two charged tracks is very small and at least one of them does not reach the detector. Consequently, events with an invariant mass of the $p\bar{p}$-system below 2.0 GeV/c^2 are rejected by the selection requirements.

Using the same method as in Section 5.2, the branching ratios of $J/\psi \to p\bar{p}$ and $\psi' \to p\bar{p}$ are calculated by fitting the peaks of the $p\bar{p}$ invariant mass in the J/ψ and ψ' regions, for all data sets apart from the one at 3.773 GeV. The results for the branching ratios are summarized in Tab. 10.1 together with the PDG values from 2016. The mean value of $\text{Br}_{J/\psi \to p\bar{p}}$ ($(2.127 \pm 0.062) \times 10^{-3}$) is in good agreement with the nominal one ($(2.120 \pm 0.029) \times 10^{-3}$), while the mean value of $\text{Br}_{\psi' \to p\bar{p}}$ ($(3.41 \pm 0.29) \times 10^{-4}$) is also compatible with the PDG value ($(2.88 \pm 0.09) \times 10^{-4}$) with large uncertainty [4]. Figure 10.4 shows the comparison of the

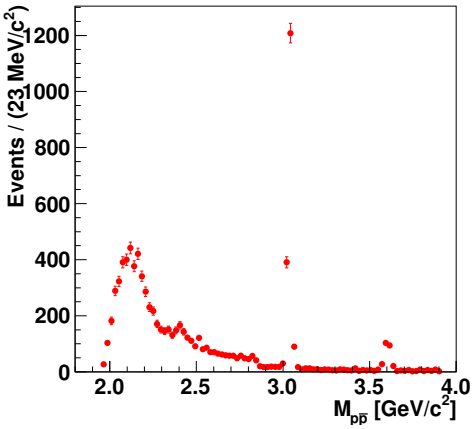

Fig. 10.3: The $p\bar{p}$ invariant-mass distribution from the combined seven data sets after the event selection.

Tab. 10.1: The branching ratios of $J/\psi \to p\bar{p}$ and $\psi' \to p\bar{p}$ from the $e^+e^- \to p\bar{p}\gamma$ analysis with the ISR photon untagged.

$\sqrt{s}$ [GeV]	$\mathrm{Br}_{J/\psi \to p\bar{p}}$ (10^{-3})	$\mathrm{Br}_{\psi' \to p\bar{p}}$ (10^{-4})
4.009	2.16 ± 0.15	3.38 ± 0.77
4.230	1.98 ± 0.11	4.09 ± 0.60
4.260	2.29 ± 0.14	2.56 ± 0.62
4.360	2.07 ± 0.17	3.60 ± 0.80
4.420	2.12 ± 0.13	3.93 ± 0.61
4.600	2.14 ± 0.19	2.89 ± 0.80
Mean	2.13 ± 0.06	3.41 ± 0.29
PDG2016	2.120 ± 0.029	2.88 ± 0.09

branching ratios of $J/\psi \to p\bar{p}$ and $\psi' \to p\bar{p}$ from different data sets.

10.2 Background evaluation

By applying the cuts of the event selection, most of the background is removed or suppressed. Only background from $e^+e^- \to p\bar{p}\pi^0$ and two-photon processes ($e^+e^- \to e^+e^-X$ through the two-photon fusion $\gamma\gamma \to X$) remains and therefore has to be removed from the event candidates individually.

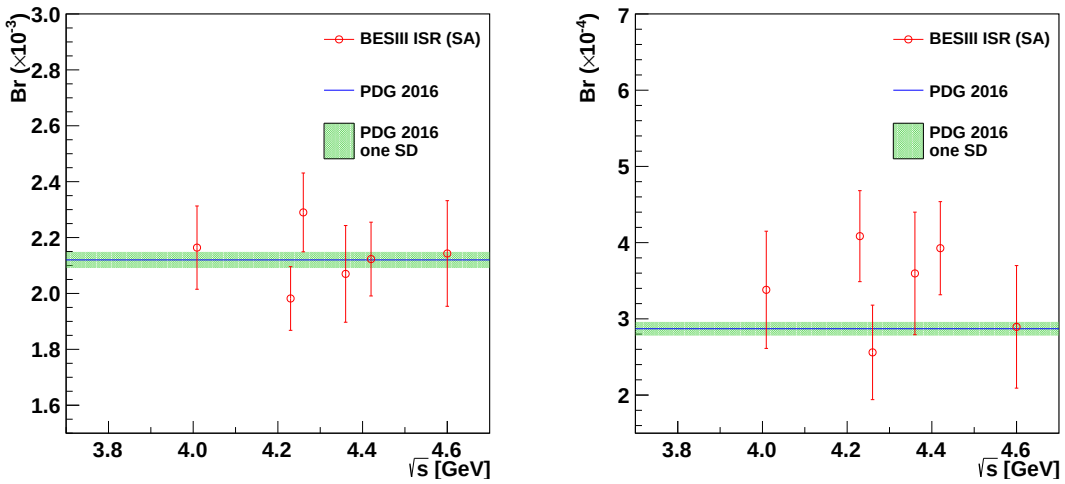

(a) $J/\psi \to p\bar{p}$ (b) $\psi' \to p\bar{p}$

Fig. 10.4: Comparison of the branching ratios: (a) $J/\psi \to p\bar{p}$ and (b) $\psi' \to p\bar{p}$. The green area shows the one standard deviation (SD) of the PDG value from 2016 [4].

10.2.1 Background from $e^+e^-\to p\bar{p}\pi^0$

To estimate the background from the $e^+e^-\to p\bar{p}\pi^0$ process, the sidebands of the angular distribution ($\theta_{\rm miss}$) of the missing momentum are studied. The cut applied on $\theta_{\rm miss}$ is the most powerful one to remove the background from this channel. The angular distribution is shown in Fig. 10.5 for the $p\bar{p}\gamma$ MC simulation (a), the $p\bar{p}\pi^0$ MC simulation (b) and the data (c) after applying all the selection conditions except for the cut on $\theta_{\rm miss}$. The red and green areas represent the signal and sideband regions, respectively. Assuming that both regions of the data consist of $p\bar{p}\gamma$ and $p\bar{p}\pi^0$ events, $N_{\rm bkg}$ is the number of $p\bar{p}\pi^0$ events in the signal region and can be estimated with the following equation:

$$N_{\rm bkg} = \frac{N_2 - \beta_{\rm isr} N_1}{\beta_{\pi^0} - \beta_{\rm isr}}, \tag{10.3}$$

where N_1 and N_2 are the number of data events in the signal and sideband regions, respectively (Fig. 10.5 (c)). The parameters $\beta_{\rm isr}$ and β_{π^0} are the ratio of events in the sideband and signal regions for the $p\bar{p}\gamma$ and $p\bar{p}\pi^0$ processes (Fig. 10.5 (a) and (b)), respectively.

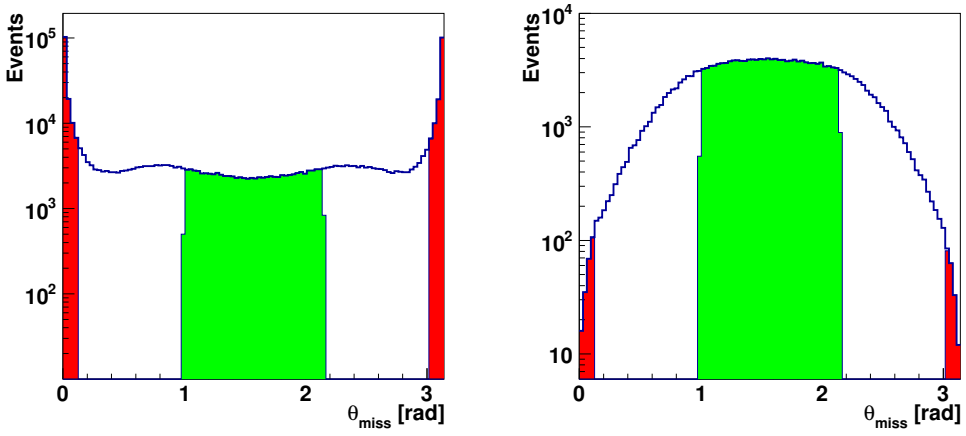

(a) $p\bar{p}\gamma$ MC

(b) $p\bar{p}\pi^0$ MC

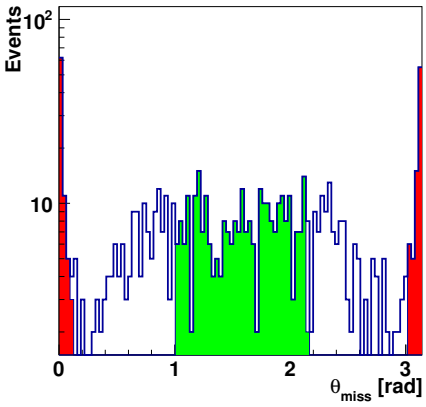

(c) data

Fig. 10.5: The angular distribution of the missing momentum in the mass region of 2.0-3.0 GeV/c^2 after applying all the selection conditions except for the cut on θ_{miss}: (a) $p\bar{p}\gamma$ MC simulation, (b) $p\bar{p}\pi^0$ MC simulation and (c) data. The red and green areas represent the signal and sideband regions, respectively.

10.2.2 Background from two-photon processes

To remove the background from the two-photon processes, the sidebands of the missing mass-squared are studied. A sideband region is defined by Eq. 10.4 and shown in the 2D scatter plot of M^2_{miss} and $M_{p\bar{p}}$ (Fig. 10.6).

The missing mass-squared is required as,

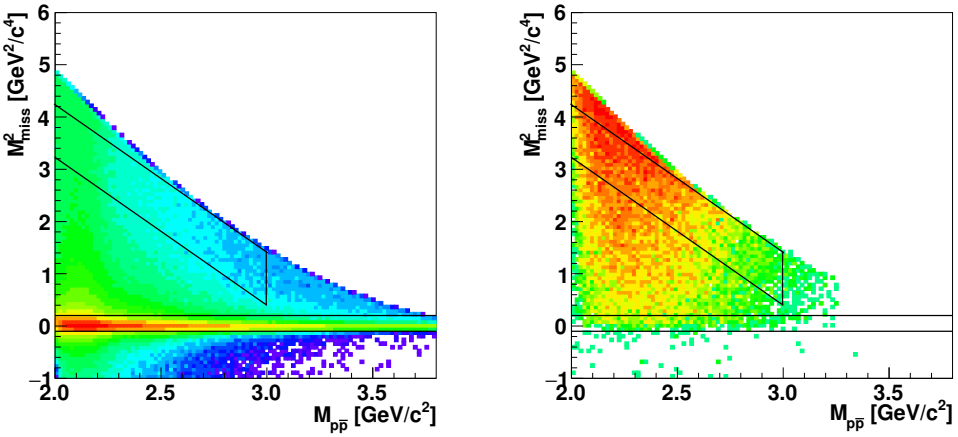

(a) $p\bar{p}\gamma$ MC

(b) two-photon processes MC

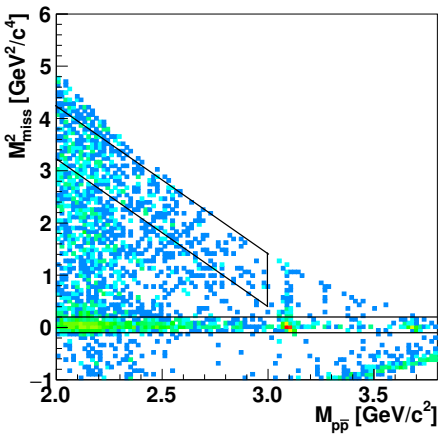

(c) data

Fig. 10.6: Scatter plot of missing mass-squared versus $p\bar{p}$ invariant mass after applying all the event selection conditions except for the cut on M^2_{miss}: (a) $p\bar{p}\gamma$ MC simulation, (b) two-photon processes MC simulation and (c) data. The black boxes and the two horizontal black lines mark the sideband and signal regions, repectively.

$$aM_{p\bar{p}} + b - y_{\text{min}} \; < \; M^2_{\text{miss}} \; < \; aM_{p\bar{p}} + b \tag{10.4}$$

where the parameters a, b and y_{min} are fixed according to the MC simulation of the two-photon processes. The values of these parameters are summarized in Tab. 10.2 for different cms energies.

The sideband region has to be large enough and only populated by the studied background

Tab. 10.2: Values of parameters describing the sideband region of the two-photon processes for different cms energies.

$\sqrt{s}$ [GeV]	a [GeV/c^2]	b [GeV^2/c^4]	$y_{\min}$ [GeV^2/c^4]
3.773	-1.93	6.35	0.3
4.009	-2.06	7.18	0.5
4.230	-2.83	9.89	1.0
4.260	-3.20	11.03	1.0
4.360	-3.26	11.48	1.0
4.420	-3.28	11.55	1.0
4.600	-3.35	12.44	1.0

to ensure the stability of the method. Table 10.3 lists background from both $p\bar{p}\pi^0$ ($N^{\rm bkg}_{p\bar{p}\pi^0}$) and two-photon ($N^{\rm bkg}_{2\gamma}$) processes as a function of the $p\bar{p}$ invariant mass from the combined seven data sets. The variables $N_{\rm obs}$ and $N_{\rm sub}$ are the number of selected events before and after the background subtraction. The background from the J/ψ and ψ' resonances is removed already.

Tab. 10.3: Estimated background in the $e^+e^-\to p\bar{p}\gamma$ analysis with the ISR photon untagged.

$M^{\rm inv}_{p\bar{p}}$ [GeV/c^2]	$N_{\rm obs}$	$N^{\rm bkg}_{p\bar{p}\pi^0}$	$N^{\rm bkg}_{2\gamma}$	$N_{\rm sub}$
2.000–2.025	186	1.0 ± 0.1	5.7 ± 1.3	179 ± 13.7
2.025–2.050	291	1.9 ± 0.2	5.7 ± 1.3	283 ± 17.1
2.050–2.075	349	2.7 ± 0.2	5.7 ± 1.3	341 ± 18.7
2.075–2.100	427	3.4 ± 0.3	8.5 ± 1.9	415 ± 20.8
2.100–2.125	436	3.0 ± 0.2	7.8 ± 1.5	425 ± 20.9
2.125–2.150	467	3.3 ± 0.2	7.2 ± 1.3	457 ± 21.6
2.150–2.175	432	3.7 ± 0.2	5.5 ± 0.9	423 ± 20.8
2.175–2.200	413	3.7 ± 0.3	7.0 ± 1.0	402 ± 20.3
2.200–2.225	343	4.1 ± 0.3	6.1 ± 1.0	333 ± 18.6
2.225–2.250	297	3.0 ± 0.2	6.5 ± 1.2	287 ± 17.3
2.250–2.275	231	3.2 ± 0.2	5.5 ± 1.0	222 ± 15.2
2.275–2.300	205	3.2 ± 0.2	4.7 ± 0.8	197 ± 14.3

2.300–2.350	318	5.7 ± 0.3	8.6 ± 1.1	304 ± 17.9
2.350–2.400	315	5.3 ± 0.3	7.0 ± 1.0	303 ± 17.8
2.400–2.450	333	4.4 ± 0.3	9.1 ± 1.3	320 ± 18.3
2.450–2.500	285	4.1 ± 0.3	8.7 ± 1.2	272 ± 16.9
2.500–2.550	219	4.2 ± 0.3	11.1 ± 1.5	204 ± 14.9
2.550–2.600	202	3.2 ± 0.2	6.7 ± 1.1	192 ± 14.3
2.600–2.650	153	3.7 ± 0.3	7.0 ± 1.2	142 ± 12.4
2.650–2.700	135	3.2 ± 0.2	6.3 ± 1.1	125 ± 11.7
2.700–2.750	127	3.5 ± 0.2	7.6 ± 1.5	116 ± 11.4
2.750–2.800	120	3.7 ± 0.2	4.8 ± 1.0	112 ± 11.0
2.800–2.850	105	3.6 ± 0.2	4.3 ± 1.1	97.1 ± 10.3
2.850–2.900	111	3.8 ± 0.3	3.1 ± 0.9	104 ± 10.6
2.900–2.950	42	1.3 ± 0.1	2.6 ± 0.6	38.2 ± 6.5
2.950–3.000	42	1.4 ± 0.1	2.6 ± 0.6	38.1 ± 6.5
3.000–3.200	152	4.5 ± 0.3	0 ± 0	148 ± 15.4
3.200–3.400	75	4.4 ± 0.3	0 ± 0	70.6 ± 8.7
3.400–3.600	61	4.1 ± 0.3	0 ± 0	56.9 ± 7.8
3.600–3.800	45	3.3 ± 0.3	0 ± 0	41.9 ± 15.1
SUM	6917	103.2 ± 1.3	165.3 ± 6.0	6649 ± 85

10.3 Extraction of observables

The cross section of $e^+e^- \to p\bar{p}$, the effective FF of the proton, and the ratio (modulus) of the proton FFs are studied from the combined candidates of the seven data sets. Before the combination, the background estimated in Section 10.3 is subtracted from each data, and the data are corrected by the MC efficiency for each data set.

10.3.1 Cross section of $e^+e^- \to p\bar{p}$ and effective form factor of the proton

The cross section of $e^+e^- \to p\bar{p}$ for each q^2-bin is calculated according to Eq. 8.6. For $p\bar{p}$ invariant mass from 2.0 to 3.8 GeV/c^2, the cross section is calculated for 30 bins with bin widths of 25, 50 and 200 MeV/c^2. The corresponding effective FF of the proton is calculated using Eq. 8.8.

The results for the cross section and the effective FF are listed in Tab. 10.4, where $\mathcal{N}_{\text{phy}}$ is the number of selected events after the background subtraction and the efficiency correction including the radiative correction factor.

Tab. 10.4: The cross section of $e^+e^- \to p\bar{p}$ and the effective FF of the proton from the $e^+e^- \to p\bar{p}\gamma$ process with the ISR photon untagged, for different invariant-mass bins.

$M^{\text{inv}}_{p\bar{p}}$ [GeV/c^2]	$\mathcal{L}$ [pb^{-1}]	$\mathcal{N}_{\text{phy}}$	σ [pb]	$\lvert G_{\text{eff}}\rvert$
2.000–2.025	2.38	1972±173	830.07±72.91	0.2685±0.0118
2.025–2.050	2.58	2184±145	847.87±56.46	0.2658±0.0089
2.050–2.075	2.64	1987±113	753.08±42.86	0.2468±0.0070
2.075–2.100	2.70	2039±104	754.56±38.51	0.2443±0.0062
2.100–2.125	2.77	1908± 95	689.16±34.43	0.2317±0.0058
2.125–2.150	2.84	1851± 89	652.19±31.20	0.2242±0.0054
2.150–2.175	2.91	1632± 81	561.07±27.79	0.2072±0.0051
2.175–2.200	2.98	1482± 75	497.11±25.25	0.1947±0.0049
2.200–2.225	3.06	1188± 66	388.58±21.74	0.1720±0.0048
2.225–2.250	3.14	991± 60	316.14±19.06	0.1552±0.0047
2.250–2.275	3.22	757± 52	235.43±16.18	0.1342±0.0046
2.275–2.300	3.30	650± 47	196.91±14.37	0.1230±0.0045
2.300–2.350	6.87	975± 58	142.03±8.38	0.1049±0.0031
2.350–2.400	7.24	943± 56	130.31±7.67	0.1013±0.0030
2.400–2.450	7.64	971± 56	127.12±7.30	0.1010±0.0029
2.450–2.500	8.08	811± 51	100.38±6.26	0.0907±0.0028
2.500–2.550	8.55	592± 43	69.19±5.07	0.0762±0.0028
2.550–2.600	9.06	554± 41	61.07±4.55	0.0725±0.0027

$M^{\rm inv}_{p\bar{p}}$ [GeV/c^2]	$\mathcal{L}$ [pb^{-1}]	$N_{\rm phy}$	σ [pb]	$\lvert G_{\rm eff}\rvert$
2.600–2.650	9.62	405± 36	42.09±3.69	0.0609±0.0027
2.650–2.700	10.23	359± 34	35.10±3.28	0.0564±0.0026
2.700–2.750	10.91	318± 31	29.14±2.88	0.0521±0.0026
2.750–2.800	11.65	311± 31	26.66±2.64	0.0505±0.0025
2.800–2.850	12.47	267± 29	21.44±2.29	0.0459±0.0025
2.850–2.900	13.37	288± 29	21.50±2.20	0.0466±0.0024
2.900–2.950	6.40	95± 16	14.82±2.53	0.0393±0.0034
2.950–3.000	6.80	95± 16	14.01±2.40	0.0387±0.0033
3.000–3.200	32.01	368± 38	11.50±1.19	0.0363±0.0019
3.200–3.400	42.63	175± 21	4.10±0.50	0.0229±0.0014
3.400–3.600	59.98	139± 19	2.32±0.32	0.0182±0.0013
3.600–3.800	86.84	103± 39	1.18±0.45	0.0137±0.0026

10.3.2 Ratio of proton form factors

As discussed in Section 8.1, the ratio of proton FFs ($R_{em} = \frac{|G_E|}{|G_M|}$) can be extracted by fitting the proton angular distribution ($\cos\theta_p$), where θ_p is the angle between the proton momentum in the $p\bar{p}$ rest frame and the $p\bar{p}$ momentum in the e^+e^- cms frame. For the analysis with the ISR photon untagged, the angular distribution of the combined data is studied in 4 intervals of $p\bar{p}$ invariant mass from 2.0 to 3.0 GeV/c^2. In each bin of the proton angular distribution, the background from the $p\bar{p}\pi^0$ final state is estimated through the sideband method and subtracted from the corresponding data set. After the backgound subtraction, the proton angular distribution from each data set is corrected by the corresponding MC efficiency.

Figure 10.7 shows the fit result (blue dashed line) for different $p\bar{p}$ invariant-mass intervals, and the distribution of the reconstructed events after background subtraction and efficiency correction (red points with error bars). The $|G_M|$ and $|G_E|$ contributions are represented by the green and red dash-dotted lines. The fitting range, the corresponding numbers of selected events from the combined data and the fit results are summarized in Tab. 10.5. The ratio of

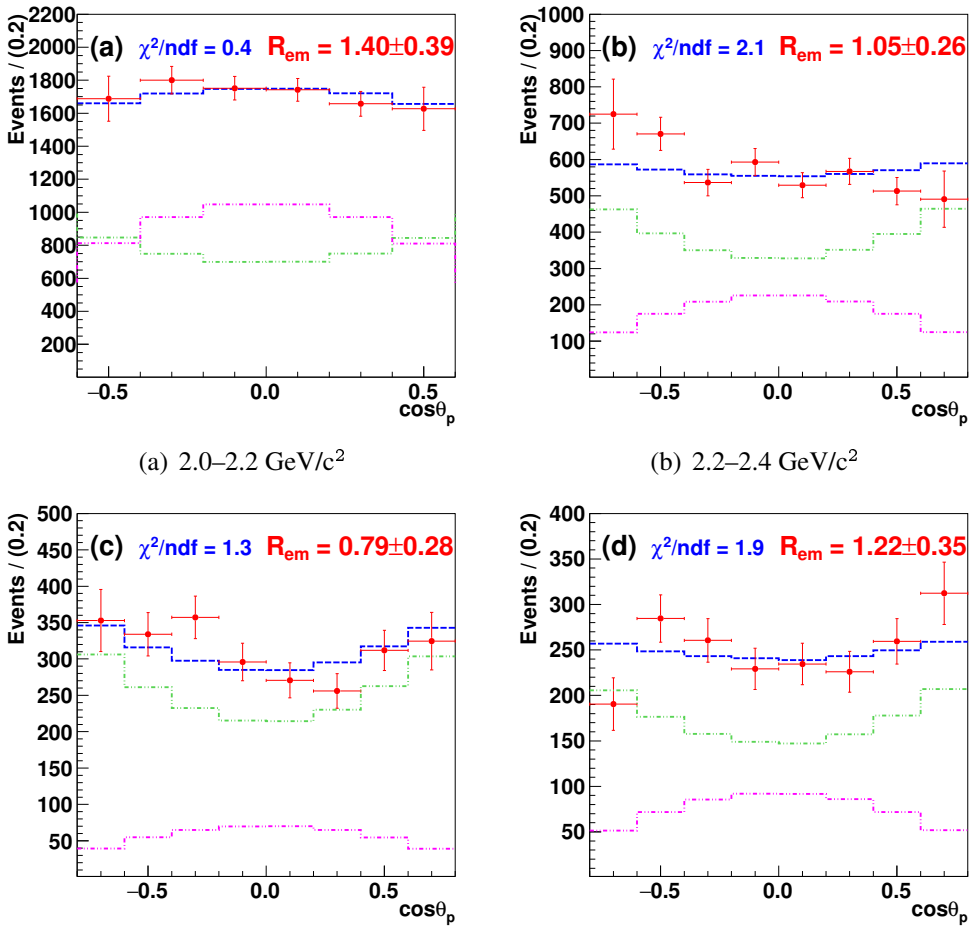

(a) 2.0–2.2 GeV/c^2

(b) 2.2–2.4 GeV/c^2

(c) 2.4–2.6 GeV/c^2

(d) 2.6–3.0 GeV/c^2

Fig. 10.7: The proton angular distribution ($\cos\theta_p$) for different $p\bar{p}$ invariant-mass intervals: (a) 2.0–2.2 GeV/c^2, (b) 2.2–2.4 GeV/c^2, (c) 2.4–2.6 GeV/c^2 and (d) 2.6–3.0 GeV/c^2. The red points with error bars show the data, the blue dashed line represents the fit results, and the green and pink dash-dotted lines correspond to G_M and G_E contributions, respectively.

proton FFs (R_{em}) includes only the statistical uncertainty.

10.4 Systematic uncertainties

Systematic uncertainties are studied separately for the cross section and the ratio of proton FFs.

Tab. 10.5: The fit results of the proton angular distribution and the ratio of proton FFs (R_{em}). The errors include only the statistical uncertainties.

$M^{\rm inv}_{p\bar{p}}$ [GeV/c^2]	Fitting range	$\mathcal{N}$	R_{em}	χ^2/ndf
2.0–2.2	[-0.6, 0.6]	2942	1.40±0.39	0.4
2.2–2.4	[-0.8, 0.8]	1648	1.05±0.26	2.1
2.4–2.6		1037	0.79±0.28	1.3
2.6–3.0		926	1.22±0.35	1.9

10.4.1 Systematic uncertainties on cross section and effective form factor of the proton

To evaluate the systematic uncertainty on the cross-section measurement, the following sources are considered: charged-tracking and PID efficiencies, E/p cut, luminosity measurement, radiative correction factor, background estimation, and cuts on $M^2_{\rm miss}$ and $\theta_{\rm miss}$. The uncertainties from the tracking efficiency (1.0% for each track) and E/p cut (1.0%) were studied in the previous measurement [42], while the uncertainty from the PID efficiency (1.0% for each track) was presented in Section 9.2. The uncertainty from the total luminosity measurement is 1.0% [76, 77].

Systematic uncertainties due to the background estimation and the radiative correction factor are treated as follows:

- From both the $p\bar{p}\pi^0$ and two-photon processes, a systematic uncertainty is defined as the difference in the cross-section measurement with and without applying background subtraction to the number of selected events.

- The uncertainty due to the $M^2_{\rm miss}$ cut is studied by changing the upper and lower limit of the $M^2_{\rm miss}$ window by around 20%. The data set at $\sqrt{s}$ = 3.773 GeV ($\sqrt{s}$ = 4.230 GeV) is used to study systematic uncertainties in the mass interval $M_{p\bar{p}}$ <2.9 GeV/c^2 ($\geq$ 2.9 GeV/c^2).

  - Case I (upper limit): $-0.02 < M^2_{\rm miss} < 0.08$ (GeV/c^2)^2 for the data set at 3.773 GeV and $-0.1 < M^2_{\rm miss} < 0.16$ (GeV/c^2)^2 for the other data sets.

- Case II (lower limit): $-0.016 < M^2_{\text{miss}} < 0.1$ (GeV/c^2)^2 for the data set at 3.773 GeV and $-0.08 < M^2_{\text{miss}} < 0.2$ (GeV/c^2)^2 for the other data sets.

The cross section is determined according to the new conditions, and the difference between it and the nominal result of the cross section (Tab. 10.4) is calculated for each case. The mean value of the differences from Case I and Case II is taken as the systematic uncertainty.

- The uncertainty on the θ_{miss} cut is studied by changing the upper and lower limits of the θ_{miss} windows by around 20%. The data set at $\sqrt{s}$ = 3.773 GeV ($\sqrt{s}$ = 4.230 GeV) is used to study systematic uncertainties in the mass intervals $M_{p\bar{p}}$ <2.9 GeV/c^2 ($\geq$ 2.9 GeV/c^2).

  - Case I (upper limit): $\theta_{\text{miss}} < 0.1 \,||\, \pi - \theta_{\text{miss}} < 0.125$
  - Case II (lower limit): $\theta_{\text{miss}} < 0.125 \,||\, \pi - \theta_{\text{miss}} < 0.1$

  For each case, the cross section is calculated and compared to the nominal result to get the difference. The mean value of the differences from the two cases is taken as the systematic uncertainty.

- 0.5% and 1.0% systematic uncertainty is associated with the radiator function $W(x, s)$ and the FSR calculation from PHOKHARA event generator, respectively [83].

The total systematic uncertainties are reported in Section 10.5 together with the final results for the cross section and the effective FF of the proton.

10.4.2 Systematic uncertainties on ratio of proton form factors

The main contributions to the systematic uncertainty on the ratio of proton FFs come from the fitting range, the background estimation, and the cuts on θ_{miss} and M^2_{miss}:

- The uncertainty from the fitting range is calculated by varying the range to a narrower one: [-0.6, 0.6] to [-0.5, 0.5] for the first mass interval, [-0.8, 0.8] to [-0.7, 0.7] for the other mass intervals.

- To evaluated the uncertainty from the background estimation, the same procedure as in the previous subsection is used for $\theta_{\rm miss}$ and $M^2_{\rm miss}$. Uncertainties are studied in the first and second mass intervals by using the large data set at 3.773 GeV.

The final result of the systematic uncertainties is reported in Section 10.5 together with the ratio of proton FFs.

10.5 Summary

With the same data sets as used in the analysis with the ISR photon tagged, the cross section of $e^+e^-\to p\bar{p}$, the effective FF of the proton and the ratio of proton FFs were measured, using the ISR process $e^+e^-\to p\bar{p}\gamma$ with the ISR photon untagged from 2.0 GeV/c^2 to 3.8 GeV/c^2 (3.0 GeV/c^2 for the ratio). Due to the higher statistics in this channel, the statistical precision of the cross section and the effective FF has been improved in comparison with the results from the analysis with the ISR photon tagged (Tab. 9.4) and from the results of previous experiments in the same invariant-mass bins [47, 48].

The cross section of $e^+e^-\to p\bar{p}$ and the effective FF of the proton are listed in Tab. 10.6 including the systematic uncertainties. The results are also shown in Fig. 10.8.

Tab. 10.6: The cross section of $e^+e^-\to p\bar{p}$ and the effective FF of the proton from the $e^+e^-\to p\bar{p}\gamma$ process with the ISR photon untagged.

$M^{\rm inv}_{p\bar{p}}$ [GeV/c^2]	σ [pb]	$\lvert G_{\rm eff}\rvert$
2.000–2.025	830±73±32	0.268±0.012±0.005
2.025–2.050	848±56±32	0.2658±0.0089±0.0050
2.050–2.075	753±43±36	0.2468±0.0070±0.0059
2.075–2.100	755±39±32	0.2443±0.0062±0.0053
2.100–2.125	689±34±30	0.2317±0.0058±0.0050
2.125–2.150	652±31±28	0.2242±0.0054±0.0048
2.150–2.175	561±28±27	0.2072±0.0051±0.0050
2.175–2.200	497±25±23	0.1947±0.0049±0.0045
2.200–2.225	389±22±18	0.1720±0.0048±0.0040

$M_{p\bar{p}}^{\mathrm{inv}}$ [GeV/c^2]	σ [pb]	$\lvert G_{\mathrm{eff}}\rvert$
2.225–2.250	316±19±17	0.1552±0.0047±0.0043
2.250–2.275	235±16±12	0.1342±0.0046±0.0035
2.275–2.300	197±14±12	0.1230±0.0045±0.0038
2.300–2.350	142.0±8.4±7.7	0.1049±0.0031±0.0028
2.350–2.400	130.3±7.7±7.9	0.1013±0.0030±0.0031
2.400–2.450	127.1±7.3±6.4	0.1010±0.0029±0.0025
2.450–2.500	100.4±6.3±6.3	0.0907±0.0028±0.0028
2.500–2.550	69.2±5.1±4.2	0.0762±0.0028±0.0023
2.550–2.600	61.1±4.5±3.6	0.0725±0.0027±0.0022
2.600–2.650	42.1±3.7±2.7	0.0609±0.0027±0.0020
2.650–2.700	35.1±3.3±2.4	0.0564±0.0026±0.0020
2.700–2.750	29.1±2.9±3.2	0.0521±0.0026±0.0028
2.750–2.800	26.7±2.6±2.6	0.0505±0.0025±0.0025
2.800–2.850	21.4±2.3±2.6	0.0459±0.0025±0.0028
2.850–2.900	21.5±2.2±2.0	0.0466±0.0024±0.0022
2.900–2.950	14.8±2.5±2.2	0.0393±0.0034±0.0029
2.950–3.000	14.0±2.4±1.5	0.0387±0.0033±0.0020
3.000–3.200	11.5±1.2±1.1	0.0363±0.0019±0.0018
3.200–3.400	4.10±0.50±0.59	0.0229±0.0014±0.0017
3.400–3.600	2.32±0.32±0.38	0.0182±0.0013±0.0015
3.600–3.800	1.18±0.45±0.21	0.0137±0.0026±0.0012

The ratio of proton FFs was extracted in 4 invariant-mass intervals from 2.0 to 3.0 GeV/c^2 by studying the proton angular distribution. Compared to the result from the analysis with the ISR photon tagged, the statistical uncertainty on the ratio was higher because of the reduced angular acceptance (see the angular distribution of the MC efficiency in Appendix C). For the same reason it was not possible to access the $p\bar{p}$ invariant-mass range below 2.0 GeV/c^2. Table 10.7 lists the values of the ratio including the systematic uncertainty. Figure 10.9 shows the ratio of proton FFs extracted in 4 invariant-mass intervals.

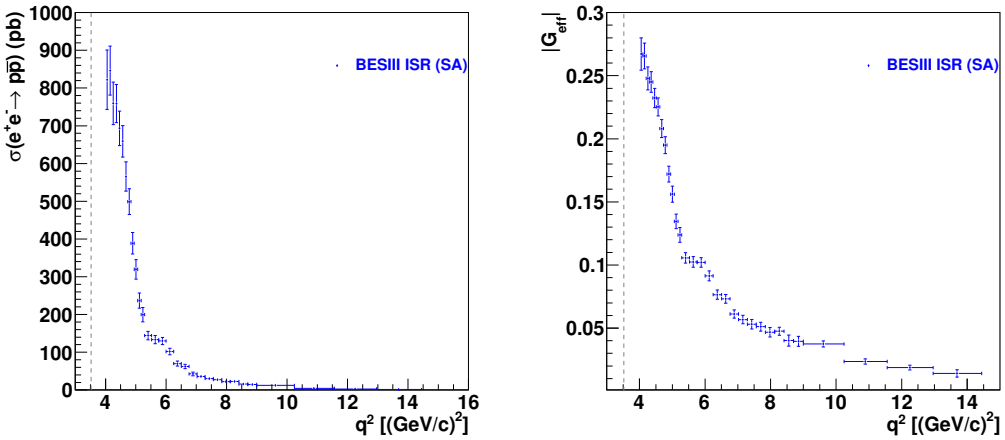

(a) Cross section (b) Effective FF

Fig. 10.8: (a) The cross section of $e^+e^-\to p\bar{p}$ and (b) the effective FF of the proton, measured from the $e^+e^-\to p\bar{p}\gamma$ process with the ISR photon untagged (Small Angle, SA).

Tab. 10.7: The ratio of proton FFs from the $e^+e^-\to p\bar{p}\gamma$ process with the ISR photon untagged.

$M^{\rm inv}_{p\bar{p}}$ [GeV/c^2]	Fitting range in $\cos\theta_p$	$R_{em}\pm\Delta R^{\rm stat.}_{em}\pm\Delta R^{\rm syst.}_{em}$
2.0–2.2	[-0.6, 0.6]	1.40±0.39±0.10
2.2–2.4	[-0.8, 0.8]	1.05±0.26±0.13
2.4–2.6		0.79±0.28±0.07
2.6–3.0		1.22±0.35±0.18

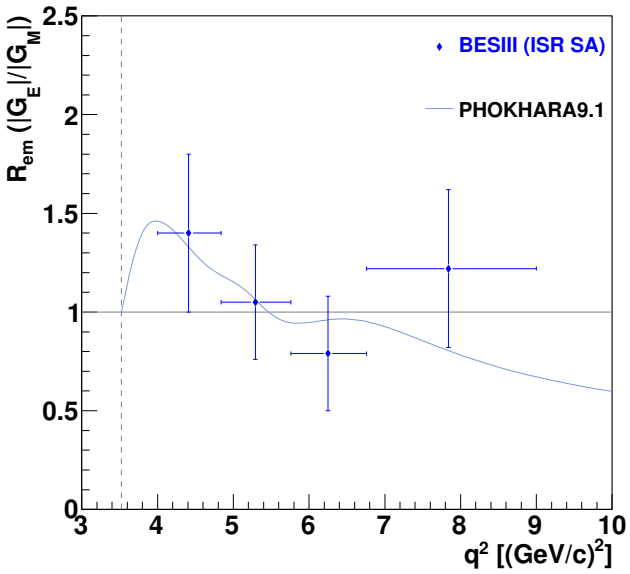

Fig. 10.9: The ratio of proton FFs extracted from the $e^+e^- \to p\bar{p}\gamma$ process with the ISR photon untagged. The light-blue line is the model used in the event generator.

CHAPTER 11

Conclusions

Using seven data sets with a total luminosity of 7.41 fb^{-1} collected by the BESIII experiment at $\sqrt{s}$ = 3.773, 4.009, 4.240, 4.260, 4.360, 4.420 and 4.600 GeV, the ratio of proton form factors, the cross section of $e^+e^- \to p\bar{p}$ and the effective form factor of the proton were measured through the initial-state-radiation process $e^+e^- \to p\bar{p}\gamma$. The ratio was extracted in 6 q^2-bins from the $p\bar{p}$ production threshold to 9.0 $(GeV/c)^2$ in the photon-tagged analysis, whereas it was extracted in 4 q^2-bins from 4.0 to 9.0 $(GeV/c)^2$ in the photon-untagged analysis. The cross section and the effective FF were measured in 31 q^2-bins from the $p\bar{p}$-threshold to 9.0 $(GeV/c)^2$ and in 30 q^2-bins from 4.0 to 14.44 $(GeV/c)^2$ in the photon tagged and untagged analyses, respectively.

In the measurements of the ratio of proton FFs, smaller statistical uncertainty has been achieved in the photon-tagged analysis, which benefits from a flat distribution for the full proton angular range (see Appendix C). The precision of the ratios measured in this thesis is comparable to the recent published measurement from the BABAR experiment. With around 1.6% of BABAR's luminosity (469 fb^{-1}), the statistical uncertainty of the ratio of proton FFs is ~ 1.7 times higher than the one from BABAR. The results for the proton FF ratio from both analyses, with the ISR photon tagged and untagged, are shown in Fig. 11.1, together with all the previous measurements [42, 43, 47, 54]. Except for the measurement from PS170 [54],

the new results are consistent with most of the previsous ones.

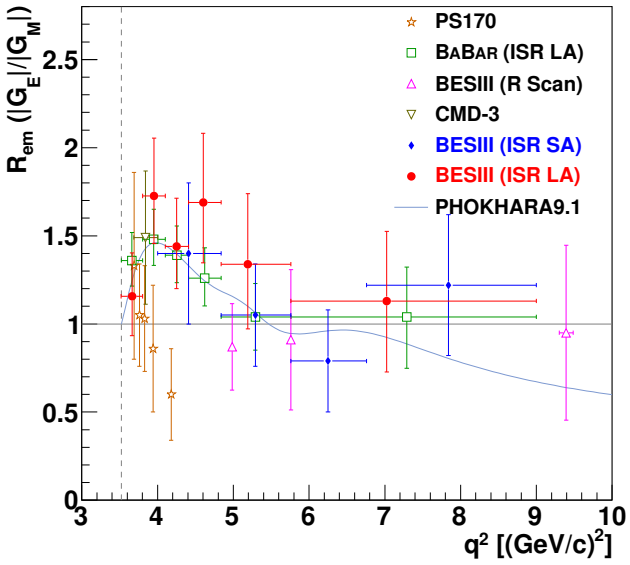

Fig. 11.1: The ratio of proton FFs extracted from the $e^+e^-\to p\bar{p}\gamma$ process with the ISR photon tagged (LA) and untagged (SA) at BESIII, together with the previous measurements.

High precision has been achieved in the measurement of the cross section of $e^+e^-\to p\bar{p}$ and the effective FF of the proton from the $e^+e^-\to p\bar{p}\gamma$ process. Due to a larger amount of events with the ISR photon emitted into a very small polar angle and the high detection efficiency of charged tracks, smaller statistical uncertainties have been obtained from the analysis with the ISR photon untagged. The total precision of the cross section is better than 10% for the bins below 2.600 GeV/c^2 (Tab. 10.6). The $e^+e^-\to p\bar{p}$ cross section measured in both analyses, with the ISR photon tagged and untagged, has full radiative corrections including ISR-NLO, FSR and VP (see Section 2.3.3 and Section 4.3). The results for the cross section of $e^+e^-\to p\bar{p}$ and the effective FF of the proton measured from the $e^+e^-\to p\bar{p}\gamma$ process are shown in Fig. 11.2 and 11.3, respectively, together with the previous measurements. The results from this thesis are consistent with the recent measurements from BABAR [47,48] and BESIII R-Scan [42] in the same q^2 range.

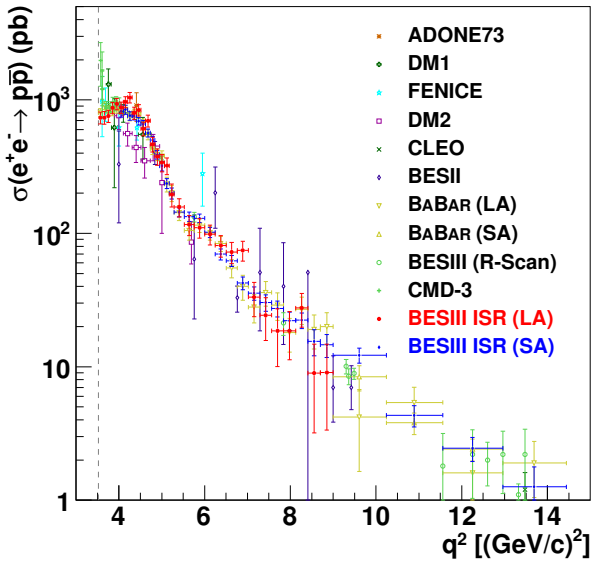

Fig. 11.2: The cross section of $e^+e^- \to p\bar{p}$ measured from the $e^+e^- \to p\bar{p}\gamma$ process with the ISR photon tagged (LA) and untagged (SA) at BESIII, together with the previous measurements.

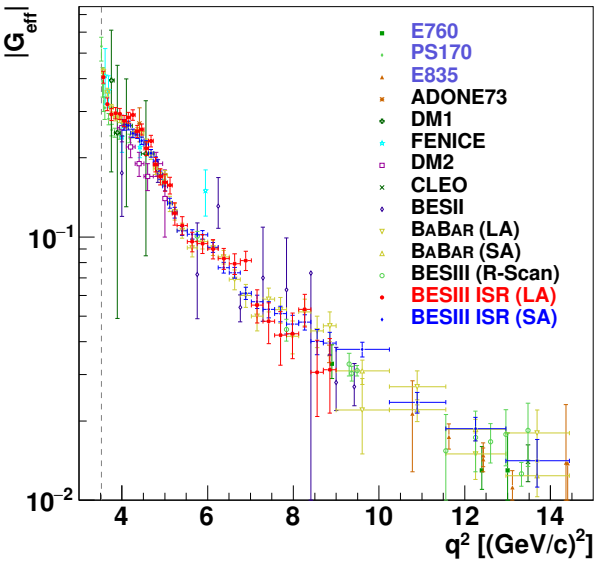

Fig. 11.3: The effective FF of the proton measured from the $e^+e^- \to p\bar{p}\gamma$ process with the ISR photon tagged (LA) and untagged (SA) at BESIII, together with the previous measurements.

APPENDIX A

Methods of Moments

In the $e^+e^- \to p\bar{p}\gamma$ analysis with ISR photon tagged (Chapter 8), the ratio of proton FFs is extracted with two methods, by fitting with H_M and H_E MC samples [83], and by using the method of moments. Both methods give consistent results (Tab. 9.3), however, the method of moments makes use of the$e^+e^- \to p\bar{p}$ differential cross section, which is an approximation in the case of the ISR process $e^+e^- \to p\bar{p}\gamma$.

The Uppsala-BESIII group has derived the expressions for the ratio of proton FFs with the method of moments, where the ratio is calculated from the expectation value of the proton angular distribution ($\cos\theta$) in the $e^+e^- \to p\bar{p}$ data after the background subtraction and the MC efficiency correction. This method was used in the recent analysis of $e^+e^- \to p\bar{p}$ from BESIII [42].

From the differential cross section of $e^+e^- \to p\bar{p}$ (Eq.2.17), the second moment of the proton angular distribution (the expectation value of $\cos^2\theta$) is given by:

$$
\begin{aligned}
< \cos^2\theta > &= \frac{\int_{-1}^{+1} \cos^2\theta \frac{d\sigma}{d\cos\theta} d\cos\theta}{\int_{-1}^{+1} \frac{d\sigma}{d\cos\theta} d\cos\theta} \\
&= \frac{\int_{-1}^{+1} N_1 |G_M|^2 \cos^2\theta [(1+\cos^2\theta) + \frac{R^2}{\tau}(1-\cos^2\theta)] d\cos\theta}{\int_{-1}^{+1} N_1 |G_M|^2 [(1+\cos^2\theta) + \frac{R^2}{\tau}(1-\cos^2\theta)] d\cos\theta} \\
&= \frac{\int_{-1}^{+1} [(1+\frac{R^2}{\tau})\cos^2\theta + (1-\frac{R^2}{\tau})\cos^4\theta] d\cos\theta}{\int_{-1}^{+1} [(1+\frac{R^2}{\tau}) + (1-\frac{R^2}{\tau})\cos^2\theta] d\cos\theta} \\
&= \frac{\frac{2}{3}(1+\frac{R^2}{\tau}) + \frac{2}{5}(1-\frac{R^2}{\tau})}{2(1+\frac{R^2}{\tau}) + \frac{2}{3}(1-\frac{R^2}{\tau})} \\
&= \frac{1}{5}\frac{4\tau+R^2}{2\tau+R^2},
\end{aligned}
\tag{A.1}
$$

where R is the ratio of proton FFs, $R = \frac{|G_E|}{|G_M|}$.

Solving this equation, the ratio of proton FFs depends on the second moment of $\cos\theta$:

$$
R = \sqrt{2\tau \frac{5 < \cos^2\theta > -2}{1 - 5 < \cos^2\theta >}}. \tag{A.2}
$$

In this thesis, a $\cos^2\theta$ distribution ($H(\cos^2\theta)$) is produced for each mass interval after the background subtraction and the MC efficiency correction. The expectation value of $\cos^2\theta$ in Eq. A.2 is substituted with the mean value $H(\cos^2\theta)$, while the uncertainty ($\Delta < \cos^2\theta >$) on the expectation value is the standard error of the mean value of the $H(\cos^2\theta)$ distribution. Applying error propagation, the uncertainty (ΔR) on the ratio is:

$$
\begin{aligned}
\Delta R &= \sqrt{\left(\frac{\partial R}{\partial <\cos^2\theta>} \Delta < \cos^2\theta > \right)^2} \\
&= \sqrt{\left(\frac{\tau}{R} \frac{5}{(1-5<\cos^2\theta>)^2} \Delta < \cos^2\theta > \right)^2}.
\end{aligned}
\tag{A.3}
$$

In the case that the signal $e^+e^- \to p\bar{p}$ events colleted for integrating over a q^2 range, the finite size of the q^2 bins has to be taken into account in the uncertainty of τ,

$$\begin{aligned} \Delta R &= \sqrt{\left(\frac{\partial R}{\partial <\cos^2\theta>}\Delta <\cos^2\theta>\right)^2 + \left(\frac{\partial R}{\partial \tau}\Delta\tau\right)^2} \\ &= \sqrt{\left(\frac{\tau}{R}\frac{5}{(1-5<\cos^2\theta>)^2}\Delta <\cos^2\theta>\right)^2 + \left(\frac{R}{2\tau}\Delta\tau\right)^2}. \end{aligned} \tag{A.4}$$

APPENDIX B

Statistics for Cross Section Measurement

The statistics of the $e^+e^- \to p\bar{p}$ cross section measurement using the $e^+e^- \to p\bar{p}\gamma$ process with the ISR photon tagged from different data set studied in this thesis ($\sqrt{s}$ = 3.773, 4.009, 4.230, 4.260, 4.360, 4.420 and 4.600 GeV) are listed in Tab. B.1-B.7.

Tab. B.1: Number of reconstructed signal events, estimated background contamination, selection efficiency and radiative factor at $\sqrt{s}$ = 3.773 GeV.

$M^{\rm inv}_{p\bar{p}}$ [GeV/c^2]	$\mathcal{N}^{\rm rec}$	$\mathcal{N}^{\rm bkg}$	$\epsilon_{\rm MC}$ (%)	(1+δ)
1.877-1.900	71	8.20±0.82	6.73±0.04	1.21
1.900-1.925	61	15.36±1.10	6.65±0.03	1.15
1.925-1.950	84	21.89±1.33	6.62±0.03	1.13
1.950-1.975	92	25.22±1.43	6.56±0.03	1.12
1.975-2.000	109	28.44±1.52	6.41±0.03	1.12
2.000-2.025	113	28.72±1.52	6.43±0.03	1.11
2.025-2.050	125	31.22±1.59	6.40±0.03	1.11
2.050-2.075	124	32.62±1.64	6.33±0.03	1.10
2.075-2.100	100	29.41±1.55	6.27±0.03	1.10

$M^{\mathrm{inv}}_{p\bar{p}}$ [GeV/c^2]	$\mathcal{N}^{\mathrm{rec}}$	$\mathcal{N}^{\mathrm{bkg}}$	ϵ_{MC} (%)	(1+δ)
2.100-2.125	89	30.00±1.58	6.34±0.03	1.10
2.125-2.150	83	25.89±1.45	6.39±0.03	1.10
2.150-2.175	94	24.26±1.41	6.32±0.04	1.10
2.175-2.200	66	23.36±1.40	6.40±0.04	1.09
2.200-2.225	66	24.24±1.44	6.47±0.04	1.09
2.225-2.250	62	20.06±1.29	6.61±0.05	1.09
2.250-2.275	59	19.16±1.25	6.75±0.06	1.09
2.275-2.300	46	18.76±1.26	6.79±0.06	1.09
2.300-2.350	77	31.54±1.65	6.99±0.05	1.09
2.350-2.400	64	28.81±1.56	7.30±0.05	1.08
2.400-2.450	55	25.98±1.51	7.37±0.06	1.08
2.450-2.500	57	22.21±1.40	7.48±0.06	1.08
2.500-2.550	53	20.35±1.34	7.61±0.07	1.08
2.550-2.600	38	18.45±1.30	7.66±0.07	1.07
2.600-2.650	51	19.84±1.35	7.74±0.08	1.08
2.650-2.700	31	18.11±1.31	7.85±0.08	1.07
2.700-2.750	28	20.97±1.42	7.99±0.09	1.06
2.750-2.800	29	21.68±1.45	8.08±0.10	1.06
2.800-2.850	31	22.57±1.48	8.00±0.10	1.07
2.850-2.900	45	24.72±1.58	8.00±0.11	1.05
2.900-2.950	28	24.38±1.59	8.13±0.11	1.06
2.950-3.000	32	26.11±1.68	8.10±0.12	1.04

Tab. B.2: Number of reconstructed signal events, estimated background contamination, selection efficiency and radiative factor at $\sqrt{s}$ = 4.009 GeV.

$M^{\mathrm{inv}}_{p\bar{p}}$ [GeV/c^2]	$\mathcal{N}^{\mathrm{rec}}$	$\mathcal{N}^{\mathrm{bkg}}$	ϵ_{MC} (%)	(1+δ)
1.877-1.900	13	2.03±0.49	6.71±0.04	1.21
1.900-1.925	14	1.92±0.45	6.48±0.03	1.15
1.925-1.950	7	3.43±0.59	6.58±0.03	1.14
1.950-1.975	9	4.20±0.65	6.51±0.03	1.12
1.975-2.000	12	4.35±0.65	6.52±0.03	1.12
2.000-2.025	13	3.65±0.59	6.42±0.03	1.11
2.025-2.050	13	3.58±0.60	6.44±0.03	1.11
2.050-2.075	15	4.90±0.69	6.40±0.03	1.10
2.075-2.100	14	4.88±0.69	6.40±0.03	1.11
2.100-2.125	19	4.12±0.63	6.32±0.03	1.10
2.125-2.150	10	2.93±0.53	6.43±0.03	1.10
2.150-2.175	11	3.89±0.60	6.36±0.04	1.10
2.175-2.200	12	2.51±0.49	6.30±0.04	1.10
2.200-2.225	9	2.86±0.52	6.36±0.04	1.10
2.225-2.250	7	2.70±0.51	6.41±0.05	1.10
2.250-2.275	4	1.89±0.42	6.59±0.05	1.10
2.275-2.300	3	1.61±0.39	6.79±0.06	1.10
2.300-2.350	6	5.31±0.71	6.79±0.05	1.10
2.350-2.400	7	4.77±0.68	7.01±0.05	1.09
2.400-2.450	6	3.19±0.56	7.24±0.06	1.09
2.450-2.500	6	3.08±0.55	7.23±0.06	1.09
2.500-2.550	8	2.90±0.54	7.29±0.07	1.08
2.550-2.600	5	1.81±0.43	7.54±0.07	1.08
2.600-2.650	7	2.07±0.46	7.69±0.08	1.09
2.650-2.700	3	1.96±0.45	7.62±0.08	1.08

$M^{\mathrm{inv}}_{p\bar{p}}$ [GeV/c^2]	$\mathcal{N}^{\mathrm{rec}}$	$\mathcal{N}^{\mathrm{bkg}}$	ϵ_{MC} (%)	(1+δ)
2.700-2.750	3	2.20±0.48	7.74±0.09	1.08
2.750-2.800	6	1.92±0.45	7.79±0.10	1.07
2.800-2.850	9	2.40±0.51	7.98±0.11	1.06
2.850-2.900	3	1.69±0.44	8.05±0.11	1.07
2.900-2.950	2	3.04±0.59	7.94±0.12	1.07
2.950-3.000	3	3.18±0.60	8.18±0.13	1.07

Tab. B.3: Number of reconstructed signal events, estimated background contamination, selection efficiency and radiative factor at $\sqrt{s}$ = 4.230 GeV.

$M^{\mathrm{inv}}_{p\bar{p}}$ [GeV/c^2]	$\mathcal{N}^{\mathrm{rec}}$	$\mathcal{N}^{\mathrm{bkg}}$	ϵ_{MC} (%)	(1+δ)
1.877-1.900	11	1.43±0.32	6.62±0.04	1.21
1.900-1.925	14	2.02±0.37	6.31±0.03	1.15
1.925-1.950	22	3.39±0.48	6.41±0.03	1.14
1.950-1.975	34	3.16±0.47	6.43±0.03	1.12
1.975-2.000	18	4.10±0.52	6.36±0.03	1.12
2.000-2.025	25	4.78±0.56	6.36±0.03	1.12
2.025-2.050	29	5.08±0.58	6.30±0.03	1.11
2.050-2.075	25	4.90±0.58	6.34±0.03	1.11
2.075-2.100	24	4.56±0.57	6.26±0.03	1.11
2.100-2.125	25	4.54±0.57	6.24±0.03	1.11
2.125-2.150	16	3.86±0.52	6.25±0.03	1.10
2.150-2.175	21	4.13±0.54	6.25±0.04	1.11
2.175-2.200	17	3.40±0.49	6.30±0.04	1.10
2.200-2.225	8	3.25±0.48	6.24±0.04	1.10
2.225-2.250	12	2.40±0.41	6.25±0.05	1.10
2.250-2.275	13	2.66±0.43	6.36±0.05	1.10
2.275-2.300	9	2.60±0.43	6.46±0.06	1.10
2.300-2.350	15	4.49±0.58	6.54±0.05	1.09

$M^{\mathrm{inv}}_{p\bar{p}}$ [GeV/c^2]	$\mathcal{N}^{\mathrm{rec}}$	$\mathcal{N}^{\mathrm{bkg}}$	ϵ_{MC} (%)	(1+δ)
2.350-2.400	11	4.07±0.55	6.68±0.05	1.09
2.400-2.450	17	4.30±0.57	6.93±0.05	1.09
2.450-2.500	13	3.63±0.53	7.03±0.06	1.09
2.500-2.550	9	2.18±0.41	7.06±0.06	1.09
2.550-2.600	12	2.67±0.46	7.26±0.07	1.08
2.600-2.650	11	2.10±0.41	7.32±0.08	1.09
2.650-2.700	4	1.97±0.40	7.35±0.09	1.09
2.700-2.750	2	1.56±0.36	7.33±0.09	1.08
2.750-2.800	5	1.56±0.36	7.51±0.10	1.08
2.800-2.850	5	2.14±0.43	7.33±0.10	1.08
2.850-2.900	8	2.30±0.44	7.62±0.11	1.07
2.900-2.950	6	1.72±0.39	7.65±0.12	1.09
2.950-3.000	5	1.86±0.41	7.68±0.13	1.08

Tab. B.4: Number of reconstructed signal events, estimated background contamination, selection efficiency and radiative factor at $\sqrt{s}$ = 4.260 GeV.

$M^{\mathrm{inv}}_{p\bar{p}}$ [GeV/c^2]	$\mathcal{N}^{\mathrm{rec}}$	$\mathcal{N}^{\mathrm{bkg}}$	ϵ_{MC} (%)	(1+δ)
1.877-1.900	16	1.07±0.28	6.61±0.04	1.21
1.900-1.925	12	1.77±0.34	6.24±0.03	1.15
1.925-1.950	17	1.94±0.36	6.34±0.03	1.14
1.950-1.975	18	2.72±0.44	6.39±0.03	1.13
1.975-2.000	19	3.32±0.48	6.35±0.03	1.12
2.000-2.025	16	2.82±0.43	6.31±0.03	1.12
2.025-2.050	17	2.76±0.43	6.23±0.03	1.12
2.050-2.075	29	3.32±0.47	6.26±0.03	1.11
2.075-2.100	25	3.82±0.52	6.25±0.03	1.11
2.100-2.125	28	2.93±0.46	6.23±0.03	1.11
2.125-2.150	19	3.69±0.51	6.19±0.03	1.11

$M^{\mathrm{inv}}_{p\bar{p}}$ [GeV/c^2]	$\mathcal{N}^{\mathrm{rec}}$	$\mathcal{N}^{\mathrm{bkg}}$	ϵ_{MC} (%)	(1+δ)
2.150-2.175	16	3.00±0.45	6.25±0.04	1.11
2.175-2.200	8	2.73±0.44	6.22±0.04	1.10
2.200-2.225	8	2.94±0.46	6.19±0.04	1.10
2.225-2.250	7	2.09±0.39	6.21±0.05	1.10
2.250-2.275	6	2.31±0.40	6.36±0.05	1.10
2.275-2.300	5	1.35±0.31	6.44±0.06	1.10
2.300-2.350	10	3.92±0.54	6.52±0.05	1.10
2.350-2.400	13	3.28±0.50	6.64±0.05	1.10
2.400-2.450	9	2.88±0.47	6.81±0.05	1.10
2.450-2.500	9	2.48±0.44	6.90±0.06	1.09
2.500-2.550	7	2.49±0.44	6.98±0.06	1.09
2.550-2.600	8	1.70±0.36	7.08±0.07	1.10
2.600-2.650	5	1.96±0.39	7.04±0.08	1.09
2.650-2.700	4	1.45±0.34	7.40±0.09	1.09
2.700-2.750	2	1.53±0.35	7.41±0.09	1.08
2.750-2.800	2	1.51±0.36	7.45±0.10	1.08
2.800-2.850	1	1.62±0.37	7.40±0.11	1.09
2.850-2.900	5	1.70±0.38	7.65±0.11	1.08
2.900-2.950	6	1.93±0.41	7.75±0.12	1.08
2.950-3.000	3	1.25±0.34	7.79±0.13	1.07

Tab. B.5: Number of reconstructed signal events, estimated background contamination, selection efficiency and radiative factor at $\sqrt{s}$ = 4.360 GeV.

$M^{\mathrm{inv}}_{p\bar{p}}$ [GeV/c^2]	$\mathcal{N}^{\mathrm{rec}}$	$\mathcal{N}^{\mathrm{bkg}}$	ϵ_{MC} (%)	(1+δ)
1.877-1.900	8	0.87±0.24	6.58±0.04	1.22
1.900-1.925	17	0.59±0.20	6.23±0.03	1.15
1.925-1.950	11	1.26±0.28	6.29±0.03	1.13
1.950-1.975	11	1.60±0.33	6.33±0.03	1.13

$M^{\mathrm{inv}}_{p\bar{p}}$ [GeV/c^2]	$\mathcal{N}^{\mathrm{rec}}$	$\mathcal{N}^{\mathrm{bkg}}$	ϵ_{MC} (%)	(1+δ)
1.975-2.000	10	1.63±0.33	6.29±0.03	1.12
2.000-2.025	10	2.07±0.37	6.26±0.03	1.12
2.025-2.050	14	2.05±0.37	6.22±0.03	1.11
2.050-2.075	11	2.49±0.40	6.17±0.03	1.11
2.075-2.100	12	2.13±0.38	6.15±0.03	1.11
2.100-2.125	16	1.66±0.33	6.17±0.03	1.11
2.125-2.150	14	1.62±0.33	6.20±0.03	1.10
2.150-2.175	4	0.94±0.25	6.14±0.04	1.11
2.175-2.200	8	1.24±0.28	6.17±0.04	1.11
2.200-2.225	6	0.89±0.25	6.31±0.04	1.10
2.225-2.250	4	1.11±0.28	6.21±0.05	1.11
2.250-2.275	5	1.16±0.28	6.27±0.05	1.10
2.275-2.300	3	0.80±0.24	6.31±0.06	1.10
2.300-2.350	8	2.37±0.41	6.34±0.05	1.10
2.350-2.400	3	1.45±0.32	6.54±0.05	1.10
2.400-2.450	6	1.53±0.33	6.68±0.05	1.10
2.450-2.500	1	1.26±0.31	6.77±0.06	1.09
2.500-2.550	2	1.35±0.32	6.89±0.06	1.09
2.550-2.600	5	1.31±0.32	7.03±0.07	1.11
2.600-2.650	5	1.08±0.29	7.20±0.08	1.09
2.650-2.700	1	1.09±0.29	7.36±0.09	1.09
2.700-2.750	5	0.71±0.24	7.25±0.09	1.08
2.750-2.800	1	0.16±0.11	7.26±0.10	1.08
2.800-2.850	1	0.74±0.25	7.39±0.11	1.09
2.850-2.900	0	0.75±0.25	7.32±0.11	1.08
2.900-2.950	0	0.43±0.19	7.31±0.12	1.08
2.950-3.000	0	1.12±0.31	7.41±0.13	1.07

Tab. B.6: Number of reconstructed signal events, estimated background contamination, selection efficiency and radiative factor at $\sqrt{s}$ = 4.420 GeV.

$M^{\mathrm{inv}}_{p\bar{p}}$ [GeV/c^2]	$\mathcal{N}^{\mathrm{rec}}$	$\mathcal{N}^{\mathrm{bkg}}$	ϵ_{MC} (%)	(1+δ)
1.877-1.900	12	0.87±0.24	6.49±0.04	1.22
1.900-1.925	15	1.55±0.32	6.16±0.03	1.15
1.925-1.950	16	1.87±0.35	6.21±0.03	1.13
1.950-1.975	18	2.10±0.38	6.25±0.03	1.13
1.975-2.000	24	2.81±0.44	6.22±0.03	1.12
2.000-2.025	16	2.73±0.42	6.21±0.03	1.12
2.025-2.050	16	3.54±0.48	6.14±0.03	1.11
2.050-2.075	26	4.31±0.53	6.14±0.03	1.11
2.075-2.100	12	3.59±0.49	6.07±0.03	1.11
2.100-2.125	19	2.93±0.44	6.10±0.03	1.11
2.125-2.150	10	2.45±0.41	6.11±0.03	1.10
2.150-2.175	24	2.08±0.38	6.15±0.04	1.11
2.175-2.200	12	2.47±0.41	6.11±0.04	1.11
2.200-2.225	16	2.56±0.42	6.18±0.04	1.10
2.225-2.250	10	1.67±0.34	6.20±0.05	1.11
2.250-2.275	11	1.79±0.35	6.10±0.05	1.11
2.275-2.300	5	1.91±0.37	6.20±0.06	1.11
2.300-2.350	11	3.82±0.52	6.27±0.05	1.10
2.350-2.400	7	2.75±0.44	6.37±0.05	1.10
2.400-2.450	11	2.17±0.40	6.59±0.05	1.10
2.450-2.500	7	2.47±0.42	6.76±0.06	1.09
2.500-2.550	7	2.30±0.41	6.79±0.06	1.09
2.550-2.600	7	1.60±0.35	6.94±0.07	1.10
2.600-2.650	4	1.52±0.34	7.14±0.08	1.10
2.650-2.700	3	1.23±0.31	7.10±0.09	1.08
2.700-2.750	5	1.08±0.29	7.15±0.09	1.09

$M^{\mathrm{inv}}_{p\bar{p}}$ [GeV/c^2]	$\mathcal{N}^{\mathrm{rec}}$	$\mathcal{N}^{\mathrm{bkg}}$	ϵ_{MC} (%)	(1+δ)
2.750-2.800	5	1.66±0.36	7.13±0.10	1.08
2.800-2.850	2	1.28±0.32	7.36±0.11	1.08
2.850-2.900	4	1.63±0.36	7.14±0.11	1.08
2.900-2.950	1	1.30±0.33	7.44±0.12	1.07
2.950-3.000	4	1.25±0.32	7.40±0.13	1.09

Tab. B.7: Number of reconstructed signal events, estimated background contamination, selection efficiency and radiative factor at $\sqrt{s}$ = 4.600 GeV.

$M^{\mathrm{inv}}_{p\bar{p}}$ [GeV/c^2]	$\mathcal{N}^{\mathrm{rec}}$	$\mathcal{N}^{\mathrm{bkg}}$	ϵ_{MC} (%)	(1+δ)
1.877-1.900	7	0.28±0.14	6.31±0.04	1.22
1.900-1.925	10	0.57±0.19	6.00±0.03	1.16
1.925-1.950	7	0.72±0.21	6.08±0.03	1.14
1.950-1.975	10	1.00±0.25	6.14±0.03	1.13
1.975-2.000	16	1.31±0.30	6.03±0.03	1.12
2.000-2.025	9	1.23±0.28	6.07±0.03	1.12
2.025-2.050	6	1.28±0.29	6.03±0.03	1.12
2.050-2.075	11	1.41±0.30	6.02±0.03	1.11
2.075-2.100	8	1.29±0.29	5.98±0.03	1.11
2.100-2.125	9	1.27±0.28	5.98±0.03	1.11
2.125-2.150	5	1.26±0.28	5.99±0.03	1.11
2.150-2.175	11	1.61±0.32	5.99±0.04	1.10
2.175-2.200	8	0.71±0.21	6.02±0.04	1.11
2.200-2.225	5	0.93±0.25	6.01±0.04	1.11
2.225-2.250	3	1.02±0.26	6.07±0.05	1.10
2.250-2.275	5	0.46±0.18	6.00±0.05	1.11
2.275-2.300	2	0.91±0.25	6.14±0.06	1.10
2.300-2.350	4	1.65±0.34	6.15±0.05	1.11
2.350-2.400	5	1.54±0.33	6.18±0.05	1.10

$M^{\mathrm{inv}}_{p\bar{p}}$ [GeV/c^2]	$\mathcal{N}^{\mathrm{rec}}$	$\mathcal{N}^{\mathrm{bkg}}$	ϵ_{MC} (%)	(1+δ)
2.400-2.450	3	1.12±0.28	6.27±0.05	1.10
2.450-2.500	5	0.77±0.23	6.50±0.06	1.10
2.500-2.550	4	1.43±0.32	6.52±0.06	1.09
2.550-2.600	4	0.36±0.16	6.61±0.07	1.08
2.600-2.650	3	0.60±0.21	6.79±0.08	1.11
2.650-2.700	6	0.67±0.22	6.80±0.08	1.09
2.700-2.750	3	0.53±0.20	7.03±0.09	1.09
2.750-2.800	1	0.76±0.24	7.18±0.10	1.10
2.800-2.850	0	0.46±0.19	6.84±0.11	1.08
2.850-2.900	1	0.08±0.08	7.12±0.12	1.09
2.900-2.950	0	0.16±0.11	7.14±0.12	1.08
2.950-3.000	0	0.16±0.11	7.04±0.13	1.08

APPENDIX C

The MC Efficiency of the Proton Angular Distribution

Figures C.1 - C.7 show the MC efficiency in the proton angular distribution from both analyses with the ISR photon tagged and untagged for all seven data sets. Flat distributions are obtained in the full angular distribution range from the analysis with the ISR photon tagged, which is a big advantange to extract the ratio of proton FFs with high precision. In the central bins, the MC efficiency in the analysis with the ISR photon untagged is much higher than in the analysis with the ISR photon tagged, but it drops dramatically in the edge bins.

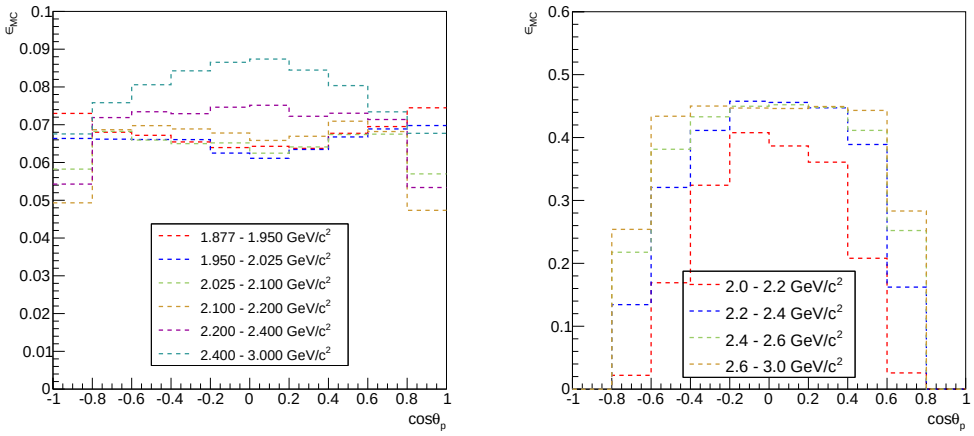

(a) tagged (b) untagged

Fig. C.1: The MC efficiency in the proton angular distribution at $\sqrt{s} = 3.773$ GeV for different invariant-mass bins: (a) with the ISR photon tagged, (b) with the ISR photon utagged.

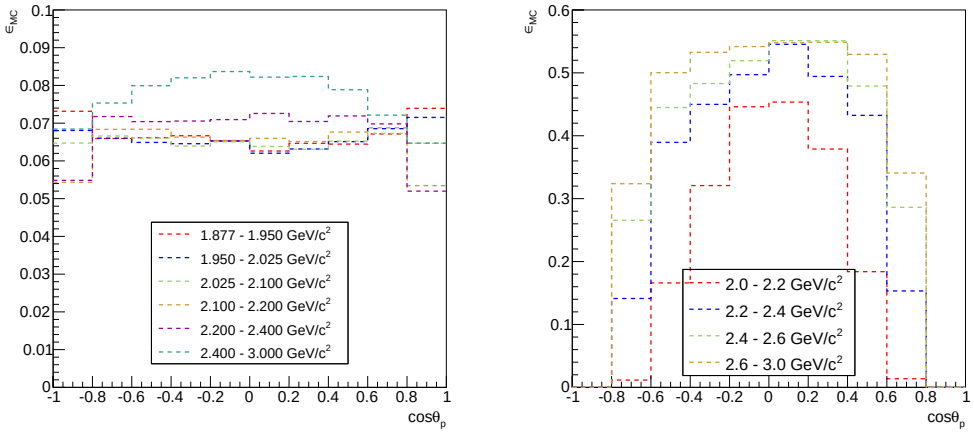

(a) tagged (b) untagged

Fig. C.2: The MC efficiency in the proton angular distribution at $\sqrt{s} = 4.009$ GeV for different invariant-mass bins: (a) with the ISR photon tagged, (b) with the ISR photon utagged.

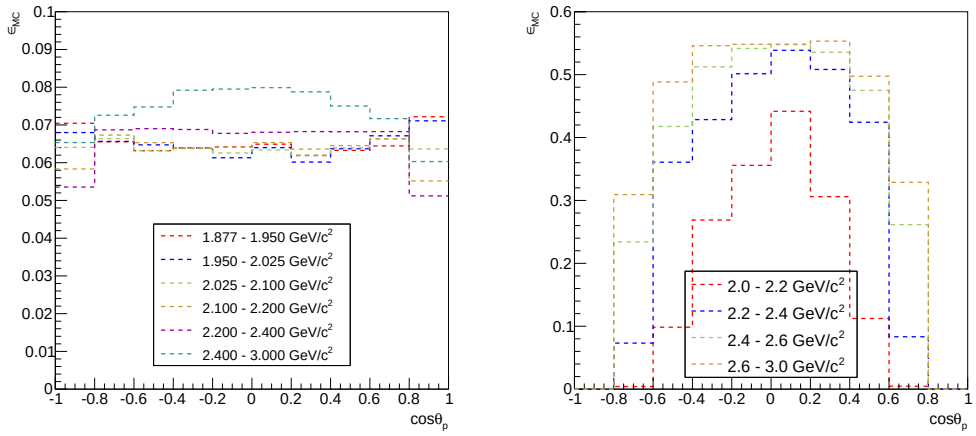

(a) tagged (b) untagged

Fig. C.3: The MC efficiency in the proton angular distribution at $\sqrt{s} = 4.230$ GeV for different invariant-mass bins: (a) with the ISR photon tagged, (b) with the ISR photon utagged.

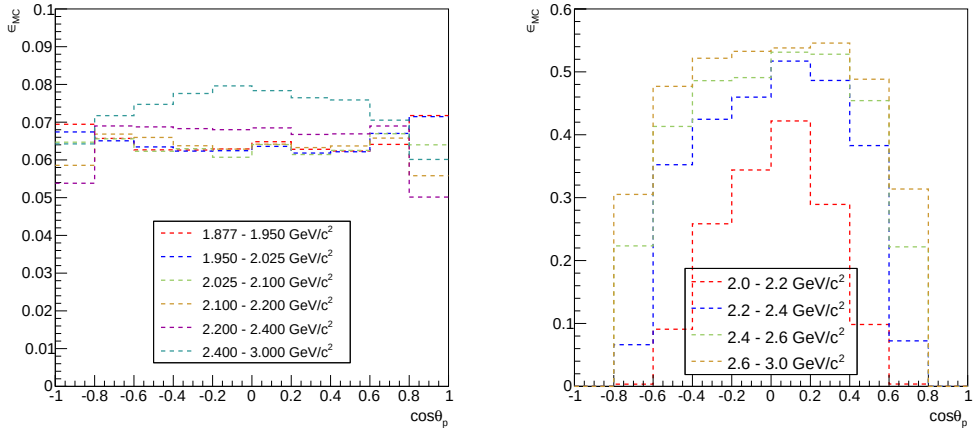

(a) tagged (b) untagged

Fig. C.4: The MC efficiency in the proton angular distribution at $\sqrt{s} = 4.260$ GeV for different invariant-mass bins: (a) with the ISR photon tagged, (b) with the ISR photon utagged.

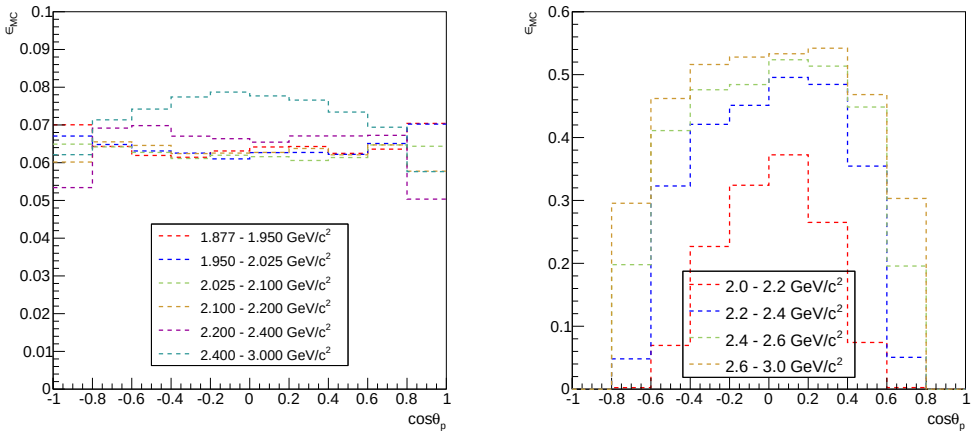

(a) tagged (b) untagged

Fig. C.5: The MC efficiency in the proton angular distribution at $\sqrt{s} = 4.360$ GeV for different invariant-mass bins: (a) with the ISR photon tagged, (b) with the ISR photon utagged.

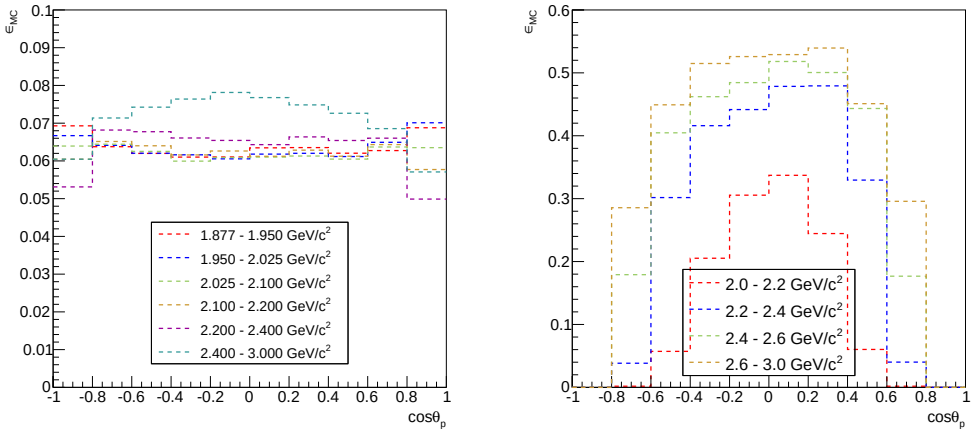

(a) tagged (b) untagged

Fig. C.6: The MC efficiency in the proton angular distribution at $\sqrt{s} = 4.420$ GeV for different invariant-mass bins: (a) with the ISR photon tagged, (b) with the ISR photon utagged.

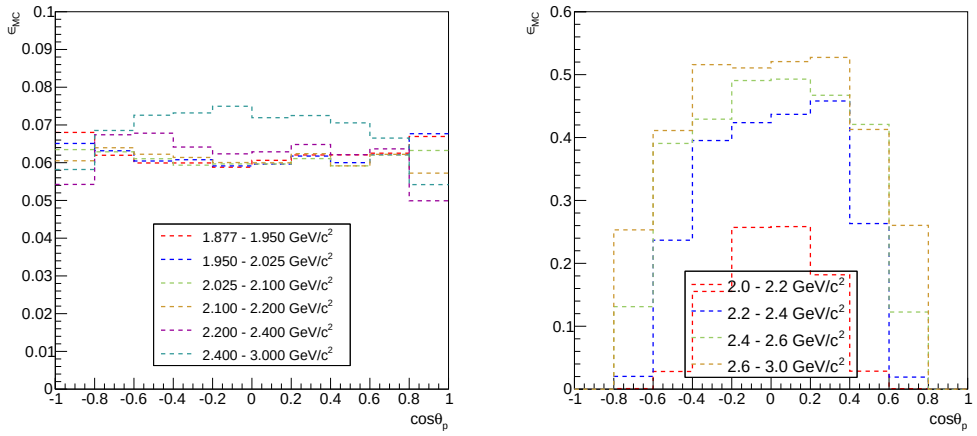

(a) tagged (b) untagged

Fig. C.7: The MC efficiency in the proton angular distribution at $\sqrt{s} = 4.600$ GeV for different invariant-mass bins: (a) with the ISR photon tagged, (b) with the ISR photon utagged.

APPENDIX D

Feasibility Study of $\bar{p}$-^{16}O Collision for $\overline{\text{P}}$ANDA Experiment

The $\overline{\text{P}}$ANDA (antiProton ANihilation at DArmstadt) experiment studies interactions between antiprotons and the fixed target protons and nuclei in the mometum range of 1.5-15.0 GeV/c using HESR (High Energy Storage Ring) at FAIR (Facility for Antiproton and Ion Research) [90]. One of the topics which can be addressed is to create antiproton-nucleus bound states.

D.1 Introduction

In the era of the low energy antiproton ring (LEAR) at CERN, the ^{A}X($\bar{p}$, p)$^{A-1}_{\bar{p}}$Y knock-out reaction was investigated to search for $\bar{p}$-nucleus bound states with the magnetic spectrometer SPES II [91]. In this experiment, the momentum of the antiproton beam was 600 MeV/c, and the beam collided with different targets such as ^{2}H, ^{6}Li, ^{12}C, ^{64}Cu, ^{208}Pb and ^{209}Bi. The knocked-out proton in the forward direction (0° with respect to the beam direction) was measured, and quasi-free elastic $\bar{p}p$ scattering was observed in the lighter targets. However, no evidence for $\bar{p}$-nucleus bound states was found during the experiment. The reason could be the very strong continuous background from protons knocked-out by high momentum pions from in-flight antiproton annihilations. These continuous inclusive

proton spectra can be described by a Maxwellian distribution [91],

$$\frac{d^2\sigma}{d\Omega dE} = C\sqrt{E}e^{-E/T}, \tag{D.1}$$

where T is an effective temperature (in MeV) related to the mass of the target, and E is the energy of the knocked-out proton. Another possible reason could be that the energy of the beam was too low to implant the antiproton into a nucleus. To better understand the continuous proton background and the creation of bound antiproton-nucleus systems in antiproton-nuclei collisions, simulations were performed with the GiBUU (Gießen-Boltzmann-Uehling-Uhlenbeck) event generator [92].

GiBUU was developed by the theoretical physics group of Gießen University and it is based on the BUU (Boltzmann-Uehling-Uhlenbeck) equation for elementary reactions on nuclei in the MeV and GeV ranges. The BUU equation describes the space-time evolution of a many-particles system under a mean-field potential and collision terms [93].

In GiBUU, the $\bar{p}p$ ($\bar{n}n$) annihilation cross section is given by the following parametrizations [93]:

$$\sigma_{\mathrm{ann}}^{\bar{p}p} = \begin{cases} 51.52p_{\mathrm{lab}}^{-0.85} + 0.034p_{\mathrm{lab}}^{-2.94} & p_{\mathrm{lab}} \leq 0.51; \\ 88.8p_{\mathrm{lab}}^{-0.4} - 24.2 & 0.51 < p_{\mathrm{lab}} \leq 6.34; \\ 38p_{\mathrm{lab}}^{-0.5} + 24p_{\mathrm{lab}}^{-1.1} & 6.34 < p_{\mathrm{lab}}, \end{cases} \tag{D.2}$$

where p_{lab} is the beam momentum in the laboratory expressed in GeV/c and the cross section, $\sigma_{\mathrm{ann}}^{\bar{p}p}$, is expressed in mb.

The $\bar{n}p$ ($\bar{p}n$) annihilation cross section coincides with $\sigma_{\mathrm{ann}}^{\bar{p}p}$ at large beam momenta and is lower than the cross section of the $\bar{p}p$ annihilation at low beam momenta:

$$\sigma_{\mathrm{ann}}^{\bar{n}p} = \begin{cases} 41.4 + 29p_{\mathrm{lab}}^{-1} & p_{\mathrm{lab}} \leq 0.382; \\ \sigma_{\mathrm{ann}}^{\bar{p}p} & 0.382 < p_{\mathrm{lab}}, \end{cases} \tag{D.3}$$

The elastic $\bar{p}p$ scattering cross section can be parameterized as:

$$\sigma_{\mathrm{el}}^{\bar{p}p} = 40p_{\mathrm{lab}}^{-0.56} + 5.8e^{-(p_{\mathrm{lab}}-1.85)^2}. \tag{D.4}$$

And the angular distribution of the elastic scattering is given by:

$$\frac{d\sigma}{dt} \propto e^{bt}, \tag{D.5}$$

where b is the slope parameter,

$$b = (A + \hbar B/p_{\bar{p}p})^2/\hbar^2, \tag{D.6}$$

expressed in GeV^{-2}, with A=0.67 fm, B=0.35 fm, and $p_{\bar{p}p}$ in the cms momentum.

Furthermore, the potential of the antiproton in the nucleus is tuned by a parameter ξ. When ξ=0.22, it correspods to $Re(V_{\rm opt}) \simeq$-150 MeV at the normal nuclear matter density.

D.2 Parameters for Simulations

In this work, two groups of the $\bar{p}$-nucleus simulations are performed. The first group is simulated to compare the continuous background with the LEAR experiment, in which the antiproton beam energy is 0.18 GeV and the target is ^{6}Li. The second group is simulated to search for $^{15}_{\bar{p}}$N bound states with the knocking-out reaction of ^{16}O($\bar{p}$, p)$^{15}_{\bar{p}}$N, and the antiproton beam energy is 1.5 GeV.

According to the introduction of GiBUU above, Tab. D.1 lists the parameters used in the simulations.

Tab. D.1: Parameters of Simulations.

$E_{\rm beam}$ (GeV)	$\sigma^{\bar{p}p}_{\rm ann}$ (mb)	$\sigma^{\bar{p}p}_{\rm el}$ (mb)	Target
0.18	84.7	80.9	^{6}Li
1.5	40.0	32.2	^{16}O

In the simulations, the impact parameter, which is the distance of closet approach of the antiproton and the nucleus following their initial strait-line trajectories, is set to zero artificially increasing the probability of the knocking-out events.

D.3 Analysis of $\bar{p}$-nucleus simulations

In the output data files of GiBUU simulations, the recorded particles, which are nucleons, mesons and other baryons, have the position and momentum information as well as the parental information describing their production. The knocked-out proton is produced by the antiproton-proton collision. According to the information of the particles in the final state, the interesting events are selected.

As mentioned in the previous section, the simulations of $\bar{p}$-nucleus collision are performed in two groups, therefore the analyses are also separated into two. In the first simulation, the events are selected to have a proton in a forward cone with the angle smaller than 5° with respect to the beam direction. In the second simulation, the interesting events are the ones with one knocked-out proton in the forward cone and the mesons produced from the antiproton-nucleon annihilation.

D.3.1 Simulation of the $\bar{p}$-^{6}Li collision

In the LEAR expriment, the continuous background of the knocked-out proton is mainly due to the final state interaction (FSI) between nucleons and mesons, or protons from other baryon decays. The kinetic energy spectrum of the knocked-out proton is described by Eq. D.1, where the beam energy is $E = 177.9$ MeV, the constant $C = 17.3$ μb/sr·MeV$^{-3/2}$, and the effective temperature $T = 101 \pm 4$ MeV [91]. Two small peaks, which represent knocked-out protons from the quasi-free scattering, are located below the beam energy for $\bar{p}$-^{6}Li collision in the LEAR expriment as shown in Fig. D.1. The lower and higher peaks come from the 1s-shell and 1p-shell knocked-out protons, respectively.

In this simulation, the continuous background is very similar to the experiment as shown in Fig. D.2. However, no quasi-free structure is observed because the nuclear structure is not included in the simulation in GiBUU. The difference between the simulation and Eq. D.1 is due to the unphysical parameter setting, the artificial head-on impact parameter.

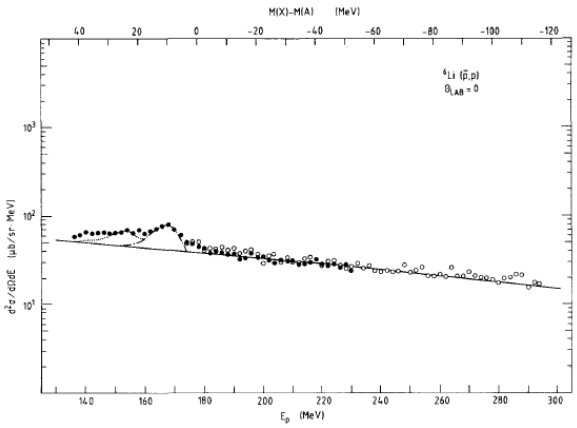

Fig. D.1: The results of $\bar{p}$-^{6}Li in LEAR experiment [91].

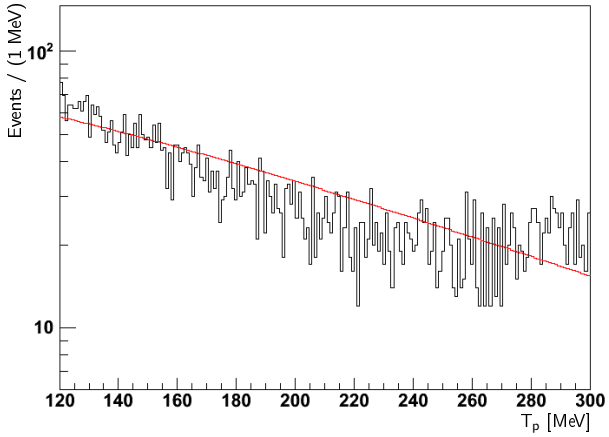

Fig. D.2: The results of the continuous background simulation for ^{6}Li($\bar{p}$, p)$^5_{\bar{p}}$He. The red line is Eq. D.1 with $T = 101 \pm 4$ MeV and C=17.3 μb/sr·MeV$^{-3/2}$.

D.3.2 Simulation of the $\bar{p}$-^{16}O collision

The knocking-out reaction of $\bar{p}$-^{16}O and the cascaded annihilation of the $\bar{p}$-nucleon is expressed,

$$\bar{p} + p \rightarrow \bar{p}_{\text{stopped}} + p_{\text{fast}}, \tag{D.7}$$

$$\bar{p}_{\text{stopped}} + p(n) \rightarrow \text{mesons}. \tag{D.8}$$

A typical signal event is described in two steps. The first step is the knocking-out reaction

(Eq. D.7), where a proton is knocked-out by the elastic scattering of antiproton-proton. In the second step, the stopped antiproton annihilates with a nucleon followed by mesons production (Eq. D.8).

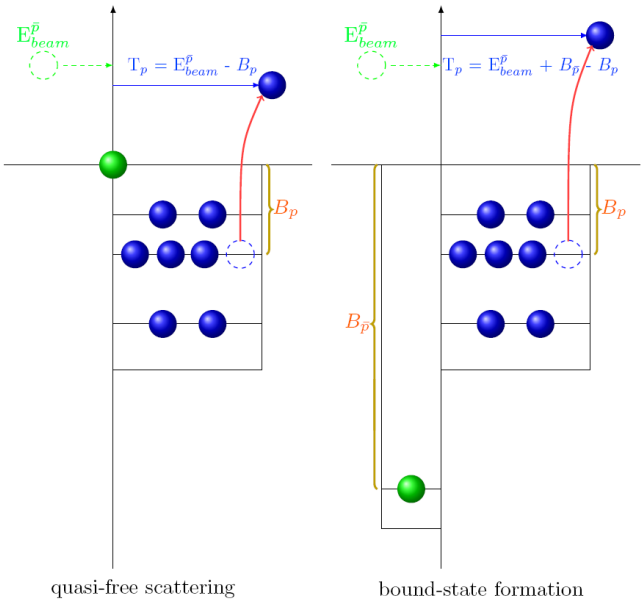

Fig. D.3: The comparison of quasi-free scattering and bound-state formation of antiproton.

For the knocking-out reaction, there are two possibilities, a quasi-free scattering or a bound-state formation. In the first case, the kinetic energy of the knocked-out proton is smaller than the beam energy, while it is larger than the beam energy in the second case because of the different binding energies expected between the proton and the antiproton in the nucleus. Figure D.3 shows a schematic illustration of the two different reaction mechanisms. The kinetic energies of knocked-out protons from the two cases can be calculated as:

$$\begin{cases} T_p = E_{\mathrm{beam}} - B_p, \\ T_p = E_{\mathrm{beam}} + B_{\bar{p}} - B_p. \end{cases} \tag{D.9}$$

Following the knocking-out reaction, the stopped antiproton annihilates with a nucleon at rest into mesons. And the invariant mass of the mesons is expressed as:

$$M^{\mathrm{inv}}_{\mathrm{mesons}} = \sqrt{E^2_{\mathrm{tot}} - P^2_{\mathrm{tot}}}. \tag{D.10}$$

For the quasi-free scattering process, the total annihilation energy is given by the total mass of the antiproton and the nucleon. The total momentum of the system is zero if the binding energy and the Fermi energy of the nucleon are ignored. Thus, the invariant mass of the mesons is:

$$M^{\text{inv}}_{\text{mesons}} = M_{\bar{p}} + M_N. \tag{D.11}$$

For the bound-state formation process, the antiproton has a potential energy ($V_{\bar{p}}$) with the nucleus at rest, which shifts the mass of the bounded antiproton to $M_{\bar{p}}$+$V_{\bar{p}}$. This decreases the invariant mass of the mesons compared to the previous case:

$$M^{\text{inv}}_{\text{mesons}} = M_{\bar{p}} + M_N + V_{\bar{p}}, \tag{D.12}$$

where the potential energy of the antiproton in the nucleus, $V_{\bar{p}}$, has a negative value, and the binding energy of the $\bar{p}$-^{15}N bound state, $B_{\bar{p}}$ = -$V_{\bar{p}}$, has a positive value.

To get larger statistics of the interesting events, two settings are modified artificially in GiBUU. First, for the two-body interaction, the differential cross section (see Eq. D.5) of the scattering $\bar{p}_1 p_2 \rightarrow \bar{p}_3 p_4$,

$$\frac{d\sigma}{dt} = \frac{\sigma_0 b e^{bt}}{1 - e^{-bt_{\text{max}}}}, \tag{D.13}$$

is replaced by an isotropic one,

$$\frac{d\sigma_{\text{iso}}}{dt} = \frac{\sigma_0}{t_{\text{max}}}, \tag{D.14}$$

where $t = (p_1 - p_3)^2 = -2q^2(1 - \cos_\theta)$, $q = \sqrt{\frac{s}{4} - m^2}$ is the cms momentum, $t_{\text{max}} = 4q^2$, and σ_0 is the total elastic scattering cross section integrated over all scattering angles. Secondly, the impacting parameter is set to be zero artificially instead of a random value, which is the optimal condition to implant an antiproton into the nucleus through the knocking-out reaction.

Event selection in the $\bar{p}$-^{16}O simulation

From Tab. D.1, the cross section of antiproton-proton annihilation in flight is larger than the elastic scattering cross section at the beam energy 1.5 GeV. The pions, which are produced from the antiproton annihilation in flight, can knock out a proton in forward direction. Furthermore, a baryon produced from an antiproton-nucleon annihilation can also decay and emitt a proton. These inclusive protons are the continuous background due to the continuous distribution of the pions.

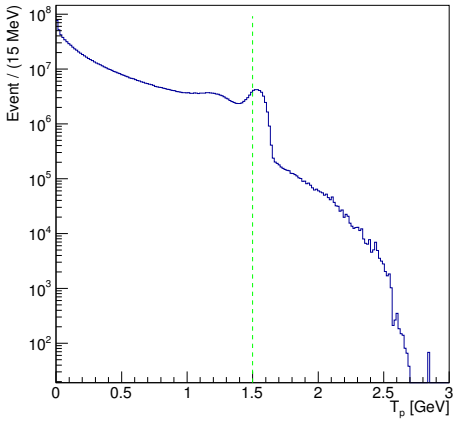

Fig. D.4: The kinetic energy distribution of the proton in the forward direction from the $\bar{p}$-^{16}O interaction. The green dashed line marks the beam energy.

Figure D.4 shows the kinetic energy distribution of the inclusive protons in the forward direction with respect to the beam direction from 10^9 events generated for the simulation of $\bar{p}$-^{16}O with E_{beam}=1.5 GeV.

To reject the continuous background, two conditions are required by the event selection:

- the event must have one and only one knocked-out proton by the antiproton in the forward cone with an angle smaller than 5° with respect to the beam direction,
- except for nucleons from the target, only pions are present in the final state, which come from the annihilation of antiproton and nucleon directly or from the other mesons decays, such as η, ρ, ω, η' and ϕ.

Figure D.5 (a) shows the exclusive protons in the forward cone knocked out by the antiporton. Additionally, only the pions are required in the final state, the invaraint mass of the pions is shown in Fig. D.5 (b). From 10^9 generated events, only $\sim 10^4$ events are left by applying these two conditions. Figure D.6 (a) and (b) show the total momentum of the pions and a scatter plot for the invariant mass of the pions and the kinetic energy of the knocked-out proton. According to Eq. D.9 and Eq. D.12, the signal ($\bar{p}$-^{15}N bound state) events must be in the upper-left area of the scatter plot. In these plots, the green and red dashed lines mark the beam energy (1.5 GeV, or momentum 2.25 GeV/c) and the rest mass of two nucleons (1.877 GeV/c^2).

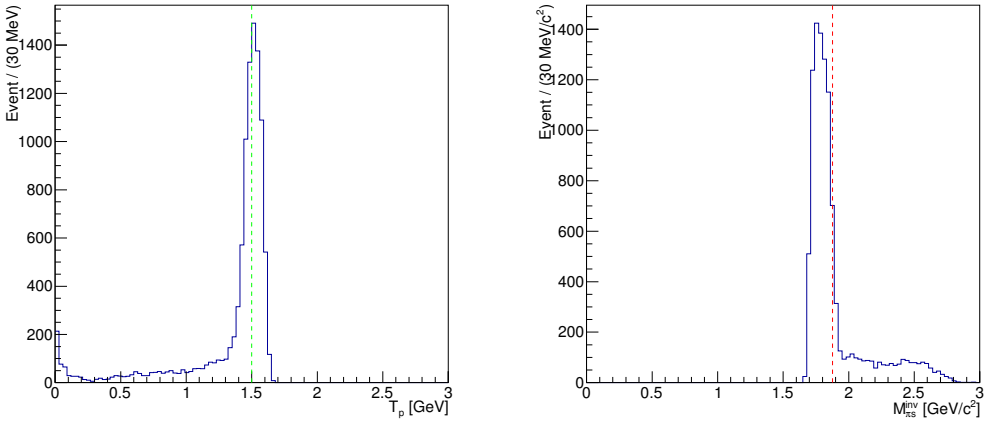

(a) Kinetic energy of the knocked-out proton (b) Invariant mass of the pions

Fig. D.5: The knocking-out reaction with only the pions in the final state: (a) kinetic energy distribution of the knocked-out proton, (b) invariant-mass distribution of the pions. The green and red dashed lines mark the beam energy and the rest mass of two nucleons.

Searching for the $\bar{p}$-^{15}N bound state

In the energy spectrum of the exclusive proton (Fig. D.5 (a)), the tail shown in the lower energy contains knocked-out protons carrying part of the beam energy. The antiproton has the rest beam energy and annihilates in flight to produce pions This corresponds to the tail in the higher invariant mass of the pions in Fig. D.5 (b). Furthermore, these events are also seen in the higer region of the pions total momentum (Fig. D.6 (a)).

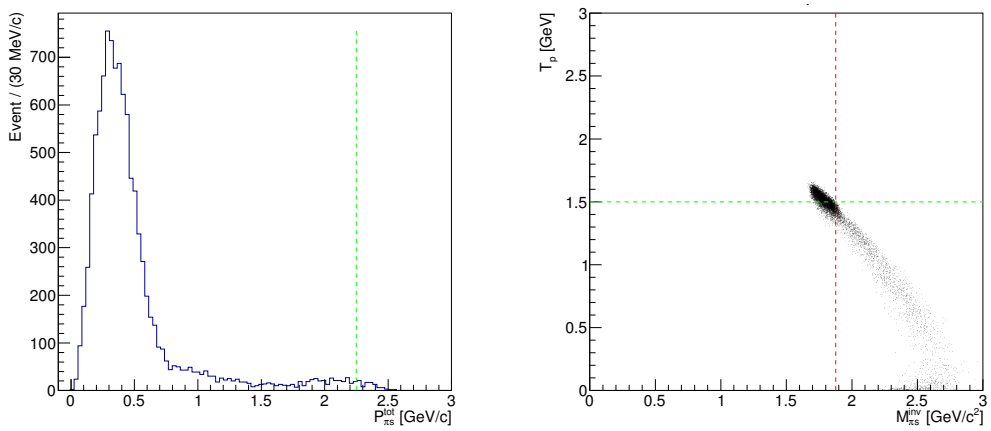

(a) Total momentum of the pions (b) Proton energy vs pions invariant mass

Fig. D.6: The knocking-out reaction with only the pions in the final state: (a) momentum distribution of the pions, (b) scatter plot of the pions invariant mass and the knocked-out proton kinetic energy. The green and red dashed lines mark the beam momentum (energy) and the rest mass of two nucleons.

In principle, the pions produced from the antiproton annihilation at rest should be isotropic and have zero total momentum. Considering the Fermi motion and the FSI of the pions, the total mometum of the pions from the $\bar{p}$-^{15}N bound state events is very small comparing to the beam momentum of the antiproton. Therefore, different cut values are applied on the total momentum of the pions to reject the low energy knocked-out proton.

Figure D.7-D.8 show the results with the cut $P_{\pi s}^{tot} \leq 750$ MeV/c, Fig. D.9-D.10 show the results with the cut $P_{\pi s}^{tot} \leq 500$ MeV/c and Fig. D.11-D.12 show the results with the cut $P_{\pi s}^{tot} \leq 250$ MeV/c.

After the cuts on the total momentum of the pions, the lower kinetic energy tail of the knocked-out proton is efficiently rejected. At the same time, the change of the pions invariant mass histogram is consistent. As seen in the 2D plots, events in the fourth quadrant are strongly suppressed.

The expected signature has the properties of a faster proton (with kinetic energy larger than the beam energy) and the pions with lower invariant mass. For these optimal simulation conditions and the proper selection criteria, there are still events which have low proton kinetic energy and high pions invariant mass, which corresponds to not fully removed background.

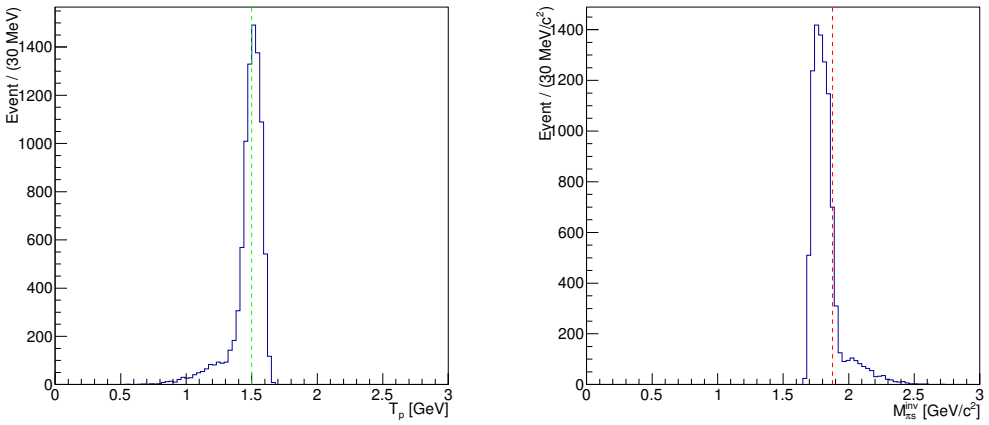

(a) Kinetic energy of the knocked-out proton (b) Invariant mass of the pions

Fig. D.7: The knocking-out reaction with the cut $P_{\pi s}^{\mathrm{tot}} \leq 750$ MeV/c: (a) kinetic energy distribution of the knocked-out proton, (b) invariant-mass distribution of the pions. The green and red dashed lines mark the beam energy and the rest mass of two nucleons.

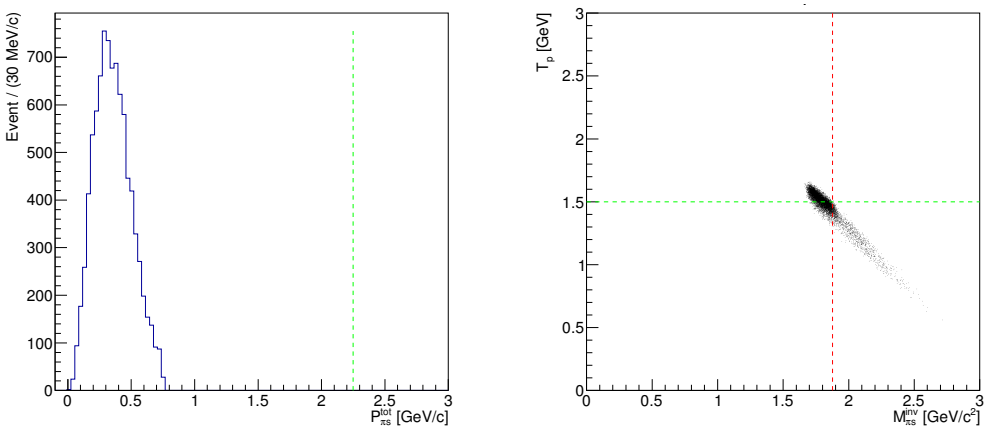

(a) Total momentum of the pions (b) Proton energy vs pions invariant mass

Fig. D.8: The knocking-out reaction with the cut $P_{\pi s}^{\mathrm{tot}} \leq 750$ MeV/c: (a) the momentum distribution of the pions, (b) scatter plot of the pions invariant mass and the knocked-out proton kinetic energy. The green and red dashed lines mark the beam momentum (energy) and the rest mass of two nucleons.

The most possible reason is because of the quasi-free scattering, in which the events have the antiproton on the surface of the nuclei and isotropic pions are produced after the annihilation

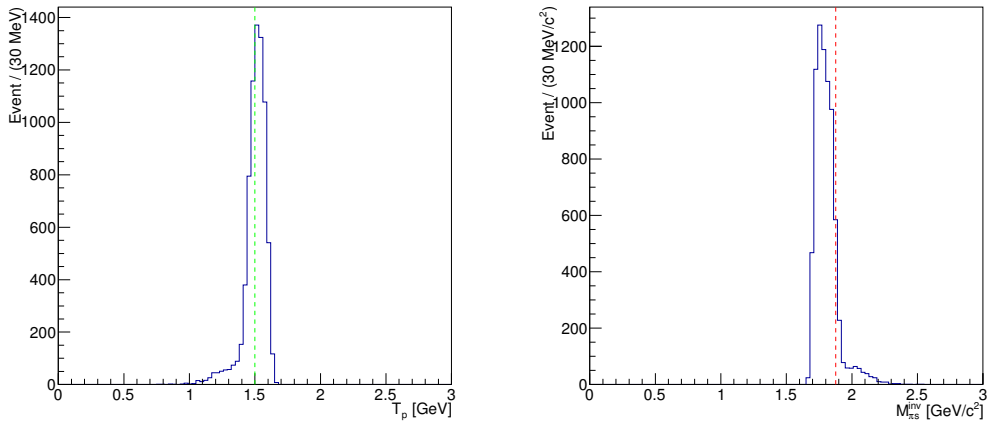

(a) Kinetic energy of the knocked-out proton (b) Invariant mass of the pions

Fig. D.9: The knocking-out reaction with the cut $P_{\pi s}^{\mathrm{tot}} \leq 500$ MeV/c: (a) kinetic energy distribution of the knocked-out proton, (b) invariant-mass distribution of the pions. The green and red dashed lines mark the beam energy and the rest mass of two nucleons.

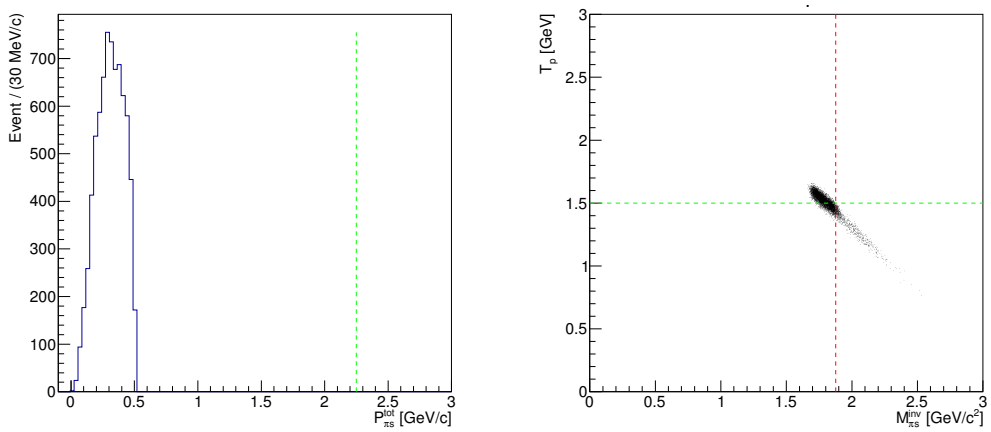

(a) Total momentum of the pions (b) Proton energy vs pions invariant mass

Fig. D.10: The knocking-out reaction with the cut $P_{\pi s}^{\mathrm{tot}} \leq 500$ MeV/c: (a) momentum distribution of the pions, (b) scatter plot of the pions invariant mass and the knocked-out proton kinetic energy. The green and red dashed lines mark the beam momentum (energy) and the rest mass of two nucleons.

at rest. These events cannot be excluded by the cut on the total momentum of the pions.

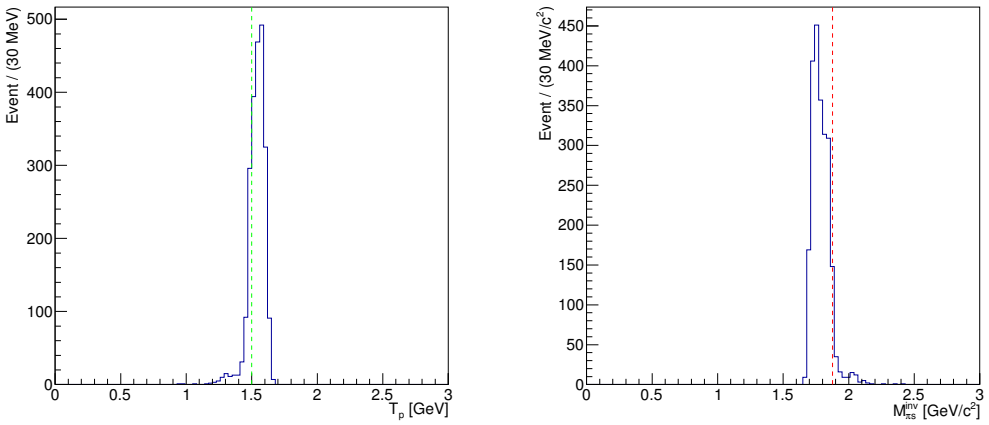

(a) Kinetic energy of the knocked-out proton (b) Invariant mass of the pions

Fig. D.11: The knocking-out reaction with the cut $P_{\pi s}^{\mathrm{tot}} \leq 250$ MeV/c: (a) kinetic energy distribution of the knocked-out proton, (b) invariant-mass distribution of the pions. The green and red dashed lines mark the beam energy and the rest mass of two nucleons.

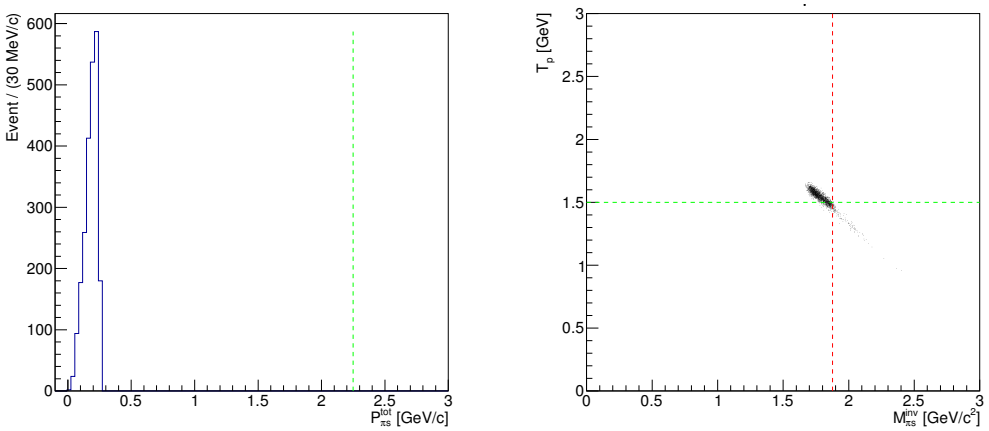

(a) Total momentum of the pions (b) Proton energy vs pions invariant mass

Fig. D.12: The knocking-out reaction with the cut $P_{\pi s}^{\mathrm{tot}} \leq 250$ MeV/c: (a) momentum distribution of the pions, (b) scatter plot of the pions invariant mass and the knocked-out proton kinetic energy. The green and red dashed lines mark the beam momentum (energy) and the rest mass of two nucleons.

D.4 Conclusions

Through the simulation of 10^9 events, the yield of expected signal events was too small even under the optimized conditions by setting parameters artifitially. Furthermore, there

was no efficient method to reject the quasi-free scattering background and to select clean $\bar{p}$-^{15}N signal events. Further study will be helpful with new methods which can supress the background.

Acronyms

$\overline{\text{P}}$ANDA	antiProton ANnihilation at DArmstadt.
BABAR	$B\ \bar{B}$ experiment.
BEPC	Beijing Electron Positron Collider.
BES	Beijing Spectrometer.
BOSS	BESIII Offiline Software System.
BUU	Boltzmann-Uehling-Uhlenbeck.
CERN	Conseil Européen pour la Recherche Nucléaire (European Organization for Nuclear Research).
CMD	Cryogenic Magnetic Detector.
DAQ	Data Acquistion.
DST	Data-Summary-Type.
EMC	Electromagnetic Calorimeter.
FF	(electromagnetic) Form Factor.
FSR	Final State Ratiation.

GDML	Geometry Description Markup Language.
ISR	Initial State Ratiation.
LEAR	Low Energy Antiproton Ring.
MC	Monte Carlo.
MDC	Multilayer Drift Chamber.
MUC	Muon Counter.
NLO	Next-to-Leading Order.
PDG	Particle Data Group.
PHSP	Phase Space.
PMT	Photomultiplier.
PQCD	perturbative Quantum Chromodynamics.
PS170	Proton Synchrotron (experiment number).
PWA	Parial Wave Analysis.
QCD	Quantum Chromodynamics.
QED	Quantum Electrodynamics.
RPC	Resistive Plate Counter.
SCQ	Superconducting Quadrupole.
SL	Space-Like.
SSM	Superconducting Solenoid Magnet.
TL	Time-Like.
VMD	Vector Meson Dominance.
VP	Vacuum Polarization.

Bibliography

[1] K. Huang, "Quarks Leptons & Gauge Fields", World Scientific Publishing, ISBN 9971-950-03-0.

[2] S. Braibant, G. Giacomelli and M. Spurio, "Particles and Fundamental Interactions: An Introduction to Particle Physics" (2nd ed.), Springer, ISBN 978-94-007-2463-1.

[3] P. Skands, [hep-ph], arXiv:1207.2389.

[4] C. Patrignani *et al.,* (Particle Data Group), Chin. Phys. C **40** (2016) 100001.

[5] G. Ecker, Prog. Part. Nucl. Phys. **35** (1995) 1.

[6] M. Gell-Mann, Phys. Lett. **8** (1964) 214.

[7] N. Brambilla *et al.,* Eur. Phys. J. C **74**:2981 (2014) 1

[8] R. Hofstadter *et al.,* Phys. Rev. **91** (1953) 422.

[9] R. Hofstadter *et al.,* Phys. Rev. **92** (1953) 978.

[10] R. Hofstadter *et al.,* Phys. Rev. **98** (1955) 217.

[11] M. N. Rosenbluth, Phys. Rev. **79** (1950) 615.

[12] L. I. Schiff Stanford Microwave Laboratory Report No. 102 (1949) 8, unpublished.

[13] C. F. Perdrisat *et al.,* Prog. Part. Nucl. Phys. **59** (2007) 694.

[14] R. Hofstadter Rev. Mod. Phys. **28** (1956) 214.

[15] E. Clementel and C. Villi, Nuov. Cim **4** (1956) 1207.

[16] R. Hofstadter *et al.,* Rev. Mod. Phys. **30** (1958) 482.

[17] V. Punjabi *et al.,* Eur. Phys. J. A **51** (2015) 79.

[18] L. L. Foldy, Phys. Rev. **87** (1952) 688.

[19] G. Salzman, Phys. Rev. **99** (1955) 973.

[20] F. Halzen and A. D. Martin, "Quaks & Leptons: An Introductory Course in Modern Particle Physics", John Wiley & Sons, (1984).

[21] S. Pacetti, R. Baldini and E. Tomasi-Gustafsson, Phys. Rep. **550-551** (2015) 1.

[22] R. Baldini, S. Pacetti and E. Tomasi-Gustafsson, JUSTC, **46** 4 (2016) 308.

[23] R. K. Bhaduri, "Models of the Nucleon", Addison-Wesley, (1988).

[24] E. A. Kuraev, C. Adamuscin, E. Tomasi-Gustafsson and F. E. Maas, Phys. Lett. B **649** (2007) 400.

[25] C. Adamuscin, E. A. Kuraev, E. Tomasi-Gustafsson and F. E. Maas, Phys. Rev. C **75** (2007) 045205.

[26] F. J. Ernst, R. G. Sachs and K. C. Wali, Phys. Rev. **119** (1960) 1105.

[27] A. Zichichi, S. M. Berman, N. Cabibbo and R. Gatto, Nuovo Cim. **24** (1962) 170.

[28] S. J. Brodsky and G. R. Farrar, Phys. Rev. Lett. **31** (1973) 1153.

[29] C. Tzara, Nucl. Phys. B **18** (1970) 246.

[30] R. Baldini, S. Pacetti and A. Zallo, Eur. Phys. A **48** (2012) 33.

[31] A. Denig and G. Salmè, Prog. Part. Nucl. Phys. **68** (2013) 113.

[32] A. D. Sakharov, Zh. Eksp. Teor. Fiz. 18 (1948) 631, Sov. Phys. Usp. 34 (1991) 375.

[33] M. Castellano *et al.*, Nuovo Cimento A **14** (1973) 1.

[34] A. Antonelli *et al.*, (FENICE Collaboration) Phys. Lett. B **313** (1993) 283.

[35] A. Antonelli *et al.*, (FENICE Collaboration) Phys. Lett. B **334** (1993) 431.

[36] A. Antonelli *et al.*, (FENICE Collaboration) Nucl. Phys. B **517** (1998) 3.

[37] B. Delcourt *et al.*, (DM1 Collaboration), Phys. Lett. B **86** (1982) 395.

[38] D. Bisello *et al.*, (DM2 Collaboration), Nucl. Phys. B **224** (1983) 379.

[39] A. Antonelli *et al.*, (DM2 Collaboration), Z. Phys. C **48** (1990) 23.

[40] T. K. Pedlar *et al.*, (CLEO Collaboration), Phy. Rev. Lett. **95** (2005) 261803.

[41] M. Ablikim *et al.*, (BES Collaboration), Phys. Lett. B **630** (2005) 14.

[42] M. Ablikim *et al.*, (BESIII Collaboration), Phys. Rev. D **91** (2015) 112004.

[43] R. R. Akhmetshin, *et al.*, Phys. Lett. B **759** (2016) 634.

[44] G. Bonneau and F. Martin, Nucl. Phys. B **27** (1971) 381.

[45] V. P. Druzhinin *et al.*, Rev. Mod. Phys. 83 (2011) 1545.

[46] J. P. Lees *et al.*, (BABAR Collaboration), Phys. Rev. D **73** (2006) 012005.

[47] J. P. Lees *et al.*, (BABAR Collaboration), Phys. Rev. D **87** 9 (2013) 092005.

[48] J. P. Lees *et al.*, (BABAR Collaboration), Phys. Rev. D **88** 7 (2013) 072009.

[49] H. Czyz, M. Gunia and J .H. Kühn, JHEP. **1308** (2013) 110.

[50] J. V. de Wiele and S. Ong, Eur. Phys. J. A **49** (2013) 18.

[51] T. A. Armstrong *et al.*, (E760 Collaboration), Phys. Rev. Lett. **70** (1993) 1212.

[52] T. A. Armstrong *et al.*, (E835 Collaboration), Phys. Rev. D **47** (1993) 772.

[53] M. Ambrogiani *et al.*, (E835 Collaboration), Phys. Rev. D **60** (1999) 032002.

[54] G. Bardin *et al.*, Nucl. Phys. B **411** (1994) 3.

[55] R. Baldini *et al.* Eur. Phys. J. C **46** (2006) 421.

[56] F. Iachello, A. D. Jackson and A. Landé, Phys. Lett. B **43** (1973) 191.

[57] F. Iachello and Q. Wan, Phys. Rev. C **69** (2004) 055204.

[58] R. Bijker and F. Iachello, Phys. Rev. C **69** (2004) 068201.

[59] Q. Wan and F. Iachello, Internat. J. Modern. Phys. A **20** (2005) 1846.

[60] V. A. Matveev, R. M. Muradyan and A. N. Tavkhelidze, Lett. Al Nuovo Ciim. **7** (1973) 719.

[61] S. J. Brodsky and G. R. Farrar, Phys. Rev. Lett. **31** (1973) 1153.

[62] G. P. Lepage and S. J. Brodsky, Phys. Rev. Lett. **43** (1979) 545.

[63] S. Pacetti and E. Tomasi-Gustafsson, private communication.

[64] A. Bianconi and E. Tomasi-Gustafsson, Phys. Rev. C **93** (2015) 035201.

[65] E. Tomasi-Gustafsson and A. Bianconi, private communication.

[66] M. H. Ye and Z. P. Zheng, Int. J. Mod. Phy. A (1987) 1707.

[67] J. Z. Bai *et al.,* Nucl. Inst. and Meth. A **344** (1994) 319.

[68] J. Z. Bai *et al.,* Nucl. Inst. and Meth. A **458** (1994) 627.

[69] K. T. Chao and Y. F. Wang, Physics at BESIII, Int. J. of Mod. Phy. V24, (2009) Supplement 1.

[70] R. Brun and F. Rademakers, "ROOT - An Object Oriented Data Analysis Framework", Nucl. Inst. & Meth. in Phys. Res. A **389** (1997) 81.

[71] M. Abilikim *et al.,* (BESIII Collaboration), Nucl. Instr. Meth. A **614** (2010) 345.

[72] BEPCII team, **BEPCII: Status and Progress**

[73] M. Ablikim *et al.,* (BESIII Collaboration), Phys. Rev. D **93** (2016) 052010.

[74] M. Ablikim *et al.,* (BESIII Collaboration), Chin. Phys. C **37** (2013) 063001.

[75] M. Ablikim *et al.,* (BESIII Collaboration), Phys. Rev. D **95** (2017) 052003.

[76] M. Ablikim *et al.,* (BESIII Collaboration), Chin. Phys. C **37** (2013) 123001.

[77] M. Ablikim *et al.,* (BESIII Collaboration), Chin. Phys. C **39** (2015) 093001.

[78] G. S. Huang, for BESIII Collaboration, arXiv:1209.4813.

[79] B. X. Zhang, BESIII *internal document* (2016).

[80] S. Agostinelli *et al.,* (GEANT4 Collaboration), Nucl. Instrum. Methods A **506** (2003) 250.

[81] J. Allison *et al.,* (GEANT4 Collaboration), IEEE Trans. Nucl. Sci. **53** (2006) 270.

[82] Z. Y. Deng *et al.,* HEP & NP, **30** (2006) 371.

[83] H. Czyz *et al.,* Phys. Rev. D **90** (2014) 114021.

[84] R. G. Ping, Chin. Phys. C **38** (2014) 083001.

[85] R. G. Ping, 2013, BESIII-doc-162-v18.

[86] J. Liu, 2013, BESIII Summer Collaboration Meeting.

[87] J. K. Wang *et al.,* Chin. Phys. C **33** (3) (2009) 210

[88] A. G. Frodesen, O. Skjeggestad and H. Tofte, Bargen, Norway: Universitetesforlaget (1979) 501p.

[89] N. Berger *et al.,* Chin. Phys. C **34** (2010) 1779.

[90] W. Erni *et al*., ($\overline{\text{P}}$ANDA Collaboration) arXiv:0903.3905.

[91] E. Aslanides *et al*., Nucl. Phys. A **470** (1987) 445

[92] GiBUU Project, Institut für Theoretische Physik, JLU Gießen.

[93] O. Buss *et al*., Phys. Rep. **512** (2012) 1.